

Sustainable Civil Infrastructures

Hany Shehata
Braja Das
A. P. S. Selvadurai
Ayman Fayed *Editors*

Advanced Numerical Methods in Foundation Engineering

Proceedings of the 3rd GeoMEast International Congress and Exhibition, Egypt 2019 on Sustainable Civil Infrastructures – The Official International Congress of the Soil-Structure Interaction Group in Egypt (SSIGE)



@Seismicisolation Springer

Sustainable Civil Infrastructures

Editor-in-Chief

Hany Farouk Shehata, SSIGE, Soil-Interaction Group in Egypt SSIGE, Cairo, Egypt

Advisory Editors

Khalid M. ElZahaby, Housing and Building National Research Center, Giza, Egypt
Dar Hao Chen, Austin, TX, USA

Sustainable Infrastructure impacts our well-being and day-to-day lives. The infrastructures we are building today will shape our lives tomorrow. The complex and diverse nature of the impacts due to weather extremes on transportation and civil infrastructures can be seen in our roadways, bridges, and buildings. Extreme summer temperatures, droughts, flash floods, and rising numbers of freeze-thaw cycles pose challenges for civil infrastructure and can endanger public safety. We constantly hear how civil infrastructures need constant attention, preservation, and upgrading. Such improvements and developments would obviously benefit from our desired book series that provide sustainable engineering materials and designs. The economic impact is huge and much research has been conducted worldwide. The future holds many opportunities, not only for researchers in a given country, but also for the worldwide field engineers who apply and implement these technologies. We believe that no approach can succeed if it does not unite the efforts of various engineering disciplines from all over the world under one umbrella to offer a beacon of modern solutions to the global infrastructure. Experts from the various engineering disciplines around the globe will participate in this series, including: Geotechnical, Geological, Geoscience, Petroleum, Structural, Transportation, Bridge, Infrastructure, Energy, Architectural, Chemical and Materials, and other related Engineering disciplines.

More information about this series at <http://www.springer.com/series/15140>

Hany Shehata · Braja Das ·
A. P. S. Selvadurai · Ayman Fayed
Editors

Advanced Numerical Methods in Foundation Engineering

Proceedings of the 3rd GeoMEast
International Congress and Exhibition, Egypt
2019 on Sustainable Civil Infrastructures –
The Official International Congress
of the Soil-Structure Interaction Group
in Egypt (SSIGE)



Springer

@Seismicisolation

Editors

Hany Shehata
Soil-Structure Interaction
Group in Egypt (SSIGE)
Cairo, Egypt

A. P. S. Selvadurai
McGill University
Montreal, QC, Canada

Braja Das
California State University
California, CA, USA

Ayman Fayed
Ain Shams University
Cairo, Egypt

ISSN 2366-3405
Sustainable Civil Infrastructures
ISBN 978-3-030-34192-3
<https://doi.org/10.1007/978-3-030-34193-0>

ISSN 2366-3413 (electronic)
ISBN 978-3-030-34193-0 (eBook)

© Springer Nature Switzerland AG 2020

This work is subject to copyright. All rights are reserved by the Publisher, whether the whole or part of the material is concerned, specifically the rights of translation, reprinting, reuse of illustrations, recitation, broadcasting, reproduction on microfilms or in any other physical way, and transmission or information storage and retrieval, electronic adaptation, computer software, or by similar or dissimilar methodology now known or hereafter developed.

The use of general descriptive names, registered names, trademarks, service marks, etc. in this publication does not imply, even in the absence of a specific statement, that such names are exempt from the relevant protective laws and regulations and therefore free for general use.

The publisher, the authors and the editors are safe to assume that the advice and information in this book are believed to be true and accurate at the date of publication. Neither the publisher nor the authors or the editors give a warranty, expressed or implied, with respect to the material contained herein or for any errors or omissions that may have been made. The publisher remains neutral with regard to jurisdictional claims in published maps and institutional affiliations.

This Springer imprint is published by the registered company Springer Nature Switzerland AG
The registered company address is: Gewerbestrasse 11, 6330 Cham, Switzerland

@Seismicisolation

Contents

Groundwater Numerical Modelling of Amman-Zarqa Basin-Jordan	1
Fayez Abdulla, Bashar Abu Dawleh, Majed Abu-Zreig, and Abbas Al-Omari	
A Density-Dependent Constitutive Model of Rockfill as Well as a Dynamic Contact Technique for Simulation of Dynamic Compaction with MPM	19
Ruiyu Zhang, Erxiang Song, Abbas Haider, and Yujin Sun	
Bearing Capacity of Square Footing: A Comparative Study Employing Non-associative MC and MCC Model	34
Mousumi Mukherjee and Arindam Dey	
A Micro-mechanical Study for Constant Shear Drained Behaviour of Granular Material	48
Hoang Bao Khoi Nguyen, Mizanur Rahman, and Hung-Chun Wang	
Stiff Degradation of Granular Material – A DEM Approach	56
Md. Mizanur Rahman, Hoang Bao Khoi Nguyen, and Hung-Chun Wang	
Conventional Method to Estimate Settlement of Plate Subjected to Bi-Axial Loading – Part II	63
Khaled R. Khater and Mohamed Abouzied	
Numerical Prediction of Thermo-Mechanical Behavior of Energy Pile in Pyroclastic Soil	89
Gianpiero Russo, Gabriella Marone, Luca Di Girolamo, and Marianna Pirone	
The Role of Constitutive Material Laws on the Jacking of Single Pile Into Sandy Soil Using Coupled Eulerian-Lagrangian Method	108
Mohamed Abdelfattah, Khalid Abdel-Rahman, Sayed M. Ahmed, and Yasser M. El-Mossallamy	

Numerical Analysis of Instabilities Affecting an Excavation on the High Speed Line in Northern Morocco	125
Ghizlane Ardouz and Khadija Baba	
Effects of Reynolds Number and Aspect Ratio on the Turbulence Characteristics in Developing and Fully Developed Flow Over a Rough Bed	133
Minakshee Mahananda, Prashanth Reddy Hanmaiahgari, and Ram Balachandar	
Author Index	145

About the Editors



Hany Shehata is the founder and CEO of the Soil-Structure Interaction Group in Egypt “SSIGE.” He is a partner and vice-president of EHE-Consulting Group in the Middle East, and managing editor of the “Innovative Infrastructure Solutions” journal, published by Springer. He worked in the field of civil engineering early, while studying, with Bechtel Egypt Contracting & PM Company, LLC. His professional experience includes working in culverts, small tunnels, pipe installation, earth reinforcement, soil stabilization, and small bridges. He also has been involved in teaching, research, and consulting. His areas of specialization include static and dynamic soil-structure interactions involving buildings, roads, water structures, retaining walls, earth reinforcement, and bridges, as well as, different disciplines of project management and contract administration. He is the author of an Arabic practical book titled “Practical Solutions for Different Geotechnical Works: The Practical Engineers’ Guidelines.” He is currently working on a new book titled “Soil-Foundation-Superstructure Interaction: Structural Integration.” He is the contributor of more than 50 publications in national and international conferences and journals. He served as a co-chair of the GeoChina 2016 International Conference in Shandong, China. He serves also as a co-chair and secretary general of the GeoMEast 2017 International Conference in Sharm El-Sheikh, Egypt. He received the Outstanding Reviewer Award for 2016 of the ASCE as selected by the Editorial Board of International Journal of Geomechanics.



Professor Braja Das is the Dean Emeritus of the College of Engineering and Computer Science, California State University, USA. He is a geotechnical engineering by profession and received his Ph.D. degree in 1972 from the University of Wisconsin, Madison, USA. For more than three decades, Professor Das has worked as a faculty member and in academic administration in several universities. He is a Fellow and Life Member of the American Society of Civil Engineers; Life Member of the American Society for Engineering Education; and Emeritus Member of TRB's AFS-80 Committee on Stabilization of Geomaterials and Stabilized Materials.

As a teacher, he has received many teaching awards including the Distinguished Achievement Award for Teaching Excellence, University of Texas at El Paso (1983); AMOCO Foundation Award for Outstanding Teaching, University of Texas at El Paso (1983); Western Electric Fund Award, ASEE (1984); and Ralph R. Teetor Educational Award, Society of Automotive Engineers Inc. (1985).

Professor Das has published more than 300 papers in various journals and peer-reviewed conference proceedings. They are mostly in the areas of shallow foundations, earth anchors, and geosynthetics. He published some of the early founding studies on the bearing capacity of shallow foundations on geogrid-reinforced sand. His past editorial activities in geotechnical engineering journals include Editorial Board Member of Journal of Geotechnical Engineering, ASCE (1988–1992); Lowland Technology International, Japan (1999–2007); Geotextiles and Geomembranes, Elsevier, UK (2008–present). He was the Associate Editor of the International Journal of Offshore and Polar Engineering (1995–1998); and Co-Editor of Geotechnical and Geological Engineering, Springer (2001–2006). He is Founder and Editor-in-Chief of the International Journal of Geotechnical Engineering (Taylor and Francis, UK) from 2007 up to the present.

Dr. Das has been a very popular keynote/or invited speaker in many conferences and special meetings in various countries. These countries include Mexico,

Dominican Republic, Costa Rica, El Salvador, Peru, Colombia, Ecuador, India, University of Birmingham, UK, Korea, Bolivia, Venezuela, Turkey, Turkish Republic of North Cyprus, and Tunisia. He has been named as the first Eulalio Juárez Badillo Lecturer by the Mexican Society of Geotechnical Engineers (November 2016).

Professor Das is the author/co-author of several texts and reference books in the area of geotechnical engineering, probably having written more than any other individual in geotechnical engineering. His textbooks have been translated into several languages and are used throughout the world. His clear, concise, and singularly unique style of presentation is very much admired, thereby attracting many students over the last 25 years who might not have considered geotechnical engineering as a profession.

This is truly his most outstanding achievement which has endeared him to many young geotechnical engineers around the world. This is his legacy—now and for years to come.



A. P. S. Selvadurai is currently William Scott Professor and Distinguished James McGill Professor in the Department of Civil Engineering and Applied Mechanics, McGill University, Montréal, Canada. He obtained his PhD degree in Theoretical Mechanics from the University of Nottingham, under the tutelage of the world-renowned continuum mechanist, the late A. J. M. Spencer. In 1986, the University of Nottingham awarded him its first-ever research DSc in Theoretical Mechanics. He was Professor and Chair of the Department of Civil Engineering at Carleton University, Ottawa, 1982 to 1991, and from 1993 to 1997, the Chair of the Department of Civil Engineering and Applied Mechanics at McGill University.

Dr. Selvadurai was awarded the Humboldt Senior Scientist Award and in 2000 (re-invitation Award, 2019) and the first civil engineer to be awarded the Killam Research Fellowship (Canada Council for the Arts). In 2003, he received the prestigious Max Planck Research Prize in the Engineering Sciences. In 2007, he

received the Killam Prize for Engineering, awarded by the Canada Council for the Arts and the CANCAM Gold Medal, awarded by the Central Committee for Canadian Congresses of Applied Mechanics. In 2008, he received the IACMAG Medal for Outstanding Accomplishments in Theoretical, Computational, and Experimental Geomechanics, and in 2010, he received the ALERT Medal awarded by Alliance of Laboratories in Europe for Research and Technology. In 2012, he was awarded the degree of Docteur Honoris Causa by the Institut Polytechnique de Grenoble, France. In 2013, he was awarded the Eric Reissner Medal of the ICCES and The Maurice A. Biot Medal of the ASCE. In 2017, he received the Chandrakant S. Desai Medal from the International Association for Computer Methods and Advances in Geomechanics.

His research includes the mechanics of elastic media undergoing large deformations, fracture mechanics, micromechanics of inclusions and defects, poroelasticity, coupled thermo-hydro-mechanical processes in deformable media, mechanics of inhomogeneous media, interfaces in geomechanics, fragmentation of brittle geomaterials, transport in porous media, and mechanics of geosynthetics subjected to chemical exposure. He is the author or co-author of texts devoted to Elastic Analysis of Soil-Foundation Interaction (Elsevier, 1979), Elasticity and Geomechanics (with R. O. Davis) (Cambridge University Press, 1996), Partial Differential Equations in Mechanics Vols. 1 & 2 (Springer-Verlag, 2000); Plasticity and Geomechanics (with R. O. Davis) (Cambridge University Press, 2002), Transport in Porous Media (with Y. Ichikawa) (Springer-Verlag, 2012), and Thermo-Poroelasticity and Geomechanics (with A. P. Suvorov) (Cambridge University Press, 2016). He serves on the Editorial Boards of nine leading International Journals devoted to Geomechanics, Applied Mechanics, Computational Mechanics, and Engineering Mathematics. He is a Fellow of several Academies and Learned Societies.

**Ayman Fayed, Ph.D., C.Eng., M.ASCE**

- Main research areas of interest: soil-structure interaction, deep foundations, excavation support systems, ground improvement and subsurface characterization.
- Expert in data analysis and modeling using numerical approaches and artificial intelligence techniques.
- Extensive experience in teaching and training both undergraduates and graduated engineers.
- Geotechnical consultant of more than 20 years of professional practice.
- Broad experience in design and analysis of geotechnical systems including deep and shallow foundations, retaining structures and ground improvement.
- Considerable experience in Dredging and Reclamation Projects.

Education:

2002/Ain Shams University/Cairo, Egypt

Ph. D. in Civil (Geotechnical) Engineering

Thesis topic “Interaction between Deep Braced Excavation and Ground for Metro Subway Stations”

1997/Ain Shams University/Cairo, Egypt

M.Sc. in Civil (Geotechnical) Engineering

Thesis topic “Uplift Resistance of Shallow Foundations”

1992/Ain Shams University/Cairo, Egypt

B.Sc. in Civil Engineering (Honor)



Groundwater Numerical Modelling of Amman-Zarqa Basin-Jordan

Fayez Abdulla¹(✉), Bashar Abu Dawleh¹, Majed Abu-Zreig^{1,2},
and Abbas Al-Omari³

¹ Civil Engineering Department, Jordan University of Science and Technology,
P.O Box 3030, Irbid, Jordan
fabdulla@just.edu.jo

² International Platform for Drylands Research and Education,
Tottori University, Tottori, Japan

³ Water and Environmental Research Center,
The University of Jordan, Amman, Jordan

Abstract. Amman Zarqa Basin (AZB) is the most developed groundwater basin in the arid region of Jordan and faces water shortage and declining water table due to overexploitation to meet irrigation and domestic water demands. Therefore, groundwater flow modeling for this watershed is a necessary tool for proper management of groundwater resources to protect AZB from depletion. MODFLOW was calibrated and used to simulate the behavior of the flow system under different pumping rates scenarios. The conceptual model for Amman-Wadi Sir (B2/A7) aquifer system was formulated by one layer unconfined type overlaid by impervious layer (A1/6 aquitard) and calibrated for steady state condition by matching observed and simulated initial head contour lines. Drawdown data for the period 1985–1995 was also used for calibration of the transient model by matching simulated drawdowns with observed ones, and then validated by using drawdown data for the period 1996–2002. The results of the calibrated model showed that the horizontal hydraulic conductivity of the B2/A7 aquifer ranges between 0.007 to 45 m/d. Calibrated specific yield ranges from 0.001 to 0.15.

Three scenarios were conducted to predict the B2/A7 aquifer system response under different conditions during the period 2020–2030. The first scenario assumed that the pumping rates of year 2005 (110.4 MCM/year) are constant for 15, and 25 years. The maximum drawdowns where found reached about 99.9 and 104.9 m in the years 2020, and 2030, respectively. The second scenario assumed that the present abstraction rates (110.4 MCM/year) is reduced to 80 MCM/year. The maximum drawdowns were reduced to about 90, and 94.8 m in the years 2020 and 2030, respectively. The third scenario assumed an abstraction rate of only 65 MCM/year. The maximum drawdowns in this case will be decreased to only 76.8, and 72.5 m for the years 2020 and 2030, respectively; this scenario (abstraction rate of 65 MCM/year) has been found to provide a safe recovery and stability in the drawdown and therefore, could be considered as the safe yield of AZB.

Keywords: MODFLOW · Amman-Zarqa Basin · Groundwater modeling · Calibration · Validation

1 Introduction

Jordan is an arid country with very limited water resources. Groundwater contributes a significant portion of the water supply in Jordan. Increased dependence on groundwater needs improved aquifer management with respect to understanding recharge and discharge issues (Tompson et al. 1999). Amman-Zarqa aquifer is located in the northern part of Jordan and is a major source of drinking water for Amman, Zarqa and Jerash cities. Furthermore, due to the increasing demand, the withdrawal from most of the Jordan's aquifers is almost double that of the safe yield. This will eventually lead to the depletion of water resources and deterioration in the water quality according to the National Water Master Plan of Jordan (NWMP 2001). Groundwater modeling is an effective tool to understand the nature of groundwater flow and for aquifer management. Groundwater modeling begins with the development of conceptual model after enough knowledge of the hydrogeology of the system, followed by the mathematical model, which consists of differential equations for hydraulic head with specification of system geometry, and boundary conditions. Many numerical methods are used to solve these differential equations; however the most common methods are finite difference and finite element method.

The present study is oriented toward finding simple methodology tool for predicting, with reasonable accuracy, the hydrological behaviour of Amman-Zarqa Basin (AZB) using appropriate and adjusted models such as MODFLOW. The study may, in future, help decision makers and planners in selecting optimum groundwater management scenarios suitable for arid and semiarid regions. This report presents the results of the groundwater modelling for AZB-Jordan the numerical groundwater modelling of the AZB aims at

1. Simulating the hydrological behaviour of AZB using the MODFLOW
2. Carrying out different management scenarios for AZB (local climate effects such as successive droughts hydrological years, groundwater pumping...)

2 Materials and Methods

2.1 Study Area

The study area lies in the north of Jordan as shown in Fig. 1. The Amman-Zarqa Basin (AZB) covers 3739 km² of area, 415 km² of which are in Syria. The basin is bordered by the Yarmouk Basin in the North, the Azraq Basin in the East and South, the Dead Sea Basin in the southwest, and by the Rift Sides Basin in the West. The drainage pattern is primarily towards west into the Jordan Valley area. The Zarqa River is the main drainage course and originates from the Amman area conveying As-Samra Treatment Plant effluent via Wadi Dhuleil where meets Zarqa River near Sukhnah Town and flowing into the King Talal Reservoir (KTR) (Fig. 2).

The Amman-Zarqa basin is the most developed watershed in Jordan. It is the fastest growing region both industrially and in terms of population. Amman-Zarqa basin comprises the Greater Amman, Dhuleil, upper Zarqa, Baq'a and Jerash areas.

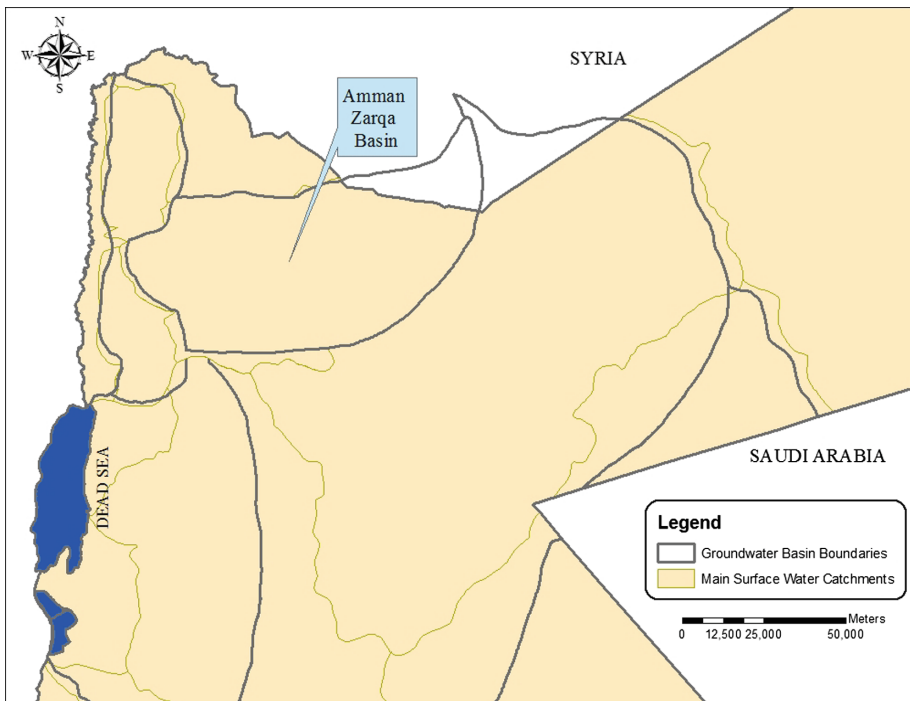


Fig. 1. Study area location (MWI 2006)

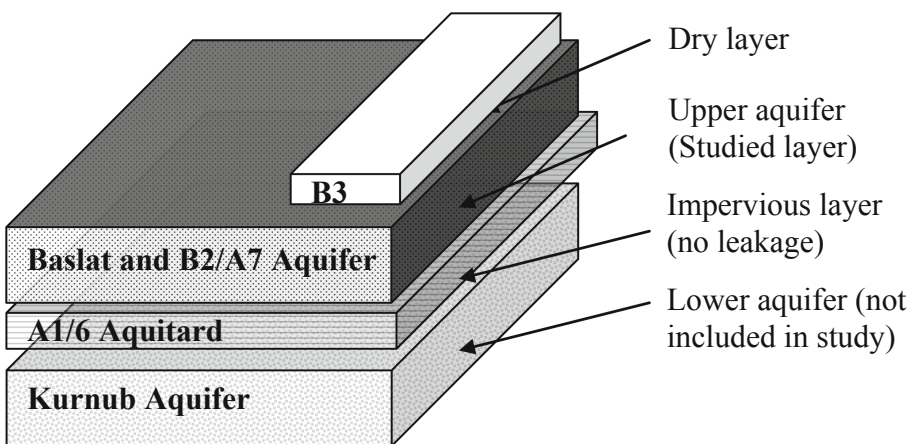


Fig. 2. Conceptual model of the study area

Groundwater resources in most of these areas are highly developed and over exploited. Groundwater potential in the basin is mostly utilized for irrigation in the areas of upper Zarqa, Baqa'a, Dhuleil and Jerash.

Average annual surface runoff in the Zarqa River as measured at New Jarash Bridge is around 68 MCM (43 and 25 MCM for base flow and flood flow respectively) for the period (1969–1999) records. In addition to the natural flows, the total flow of the Zarqa River into the KTR includes large volume of wastewater effluent from As-Samra treatment plant as well as some flows from Jerash, Abu Nseir and Baqa'a treatment plants.

Groundwater flows from the north from Arab Mountain to the northwest towards the Yarmouk basin, to the southwest towards Zarqa River, and to the East towards the Azraq aquifer. Recharge occurs directly (rainfall) and indirectly (lateral flow). Groundwater flows from the north at Jabal-el Arab area in Syria towards Yarmouk basin on the northwest, to Zarqa River basin on the southwest and to Azraq basin on the east. Total estimated annual groundwater recharge is about 70 MCM/y (direct from rainfall is about 32 MCM and about 38 MCM as subsurface flow from the north across the Syrian borders.

2.2 Groundwater Flow Modeling of AZB

The proposed methodology for the modeling of the groundwater flow of AZB is summarized below. In this study, the groundwater modeling protocol suggested by Chiang and Kinzelbach (1993) was followed. The first step in this protocol is establishing the purpose of the modeling application; it has been mentioned in Sect. 1. The processing Modflow Pro (PM5) (Chiang and Kinzelbach 1993) was selected to simulate the behavior of groundwater flow for the Amman Zarqa Basin aquifer. This model simulates three dimensional groundwater flows by using finite difference techniques.

2.2.1 Conceptual Model

The conceptual model is the second step in the modeling protocol. It is a pictorial representation of the groundwater flow system. Its prime usage is to simplify the field problem and allow organizing the associated field data, so that the system can be analyzed more readily. Such simplification of the field problem is necessary, because a complete reconstruction of the field system is not feasible.

2.2.2 Model Domain and Grid

Formulating the conceptual model helps in defining the area of interest, and for flow model and transport model the boundary, initial conditions, and the initial values for the aquifer parameters which will be discussed in the next subsections.

The model domain was selected to cover 2361 km² of the total area (2408 km²) of the Amman Zarqa watershed. The area of the modeling domain was chosen based on data availability and model boundaries not to be affected by stresses within the modeling domain. The domain is located between 390000 E, 530000 N (left lower corner) and 485000 E, 585000 N (upper right corner) according to the JTM coordinate system.

The model domain was discretized using 116 rows × 183 columns rectangular cells. This discretization produces 8734 cells in the model layer. The width of the cells varies between 335 to 1000 m depending on the location and concentration of wells as shown in the Fig. 3, and the regions that have high gradient in the water level, and taking into consideration that the ratio of the lengths of the cell sides (cell aspect ratio)

is up to 10:1 which may be used without introducing significant error (Spitz and Moreno, 1996). Also a gradual variation in cell sizes between adjacent cells was taken into consideration to be not greater than a factor of 1.5, which will facilitate model convergence, increase stability, and reduce inaccuracy (Spitz and Moreno, 1996).

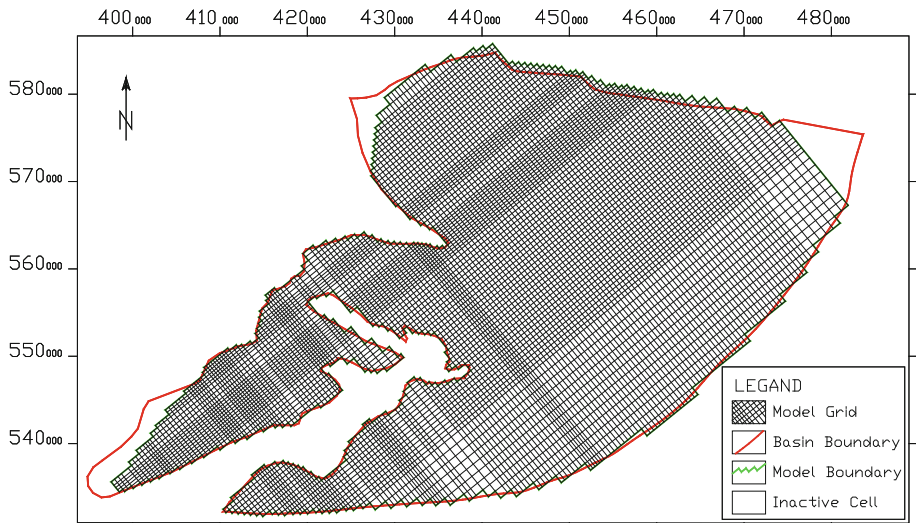


Fig. 3. Amman Zarqa Basin model boundary showing the active vs. inactive cell

The orientation of the model grid is dependent highly on the hydrogeological features of the study area and the predominant groundwater flow direction (Spitz and Moreno 1996), as a result of that the grid of the model domain can be oriented in the same direction of the predominant groundwater flow direction or inclined nearly by 39° counter clockwise on average from W-E direction as most groundwater flow moves perpendicular on that direction.

2.2.3 Boundary Conditions

Mathematical models consist of governing equations, boundary conditions, and initial conditions. Boundary conditions are mathematical statement specifying the dependent variable (head) or the derivative of the dependent variable (flux) at the boundaries of the model domain.

The specification of appropriate boundary conditions is an essential part of the conceptualizing and modeling groundwater system and is also the part most subject to serious error by hydrologists. However, there are three major types of boundary conditions, all of which may vary with time (Anderson and Woessner 1992):

- Type 1: specified head boundaries (Dirichlet conditions) for which the hydraulic head is given.
- Type 2: Specified flow boundaries (Neumann conditions) for which the derivative of head (flux) across the boundary is given. A no flow boundary condition is set by specifying flux to be zero.

- Type 3: Head-dependent flow boundaries (Cauchy or mixed boundary conditions) used to represent leakage from surface water bodies where the exchange of water between aquifer and surface water depends on the head differences between surface water and groundwater. Leakage to or from a river, lake or reservoir is good examples for this type.

MODFLOW uses the flag “IBOUND” to assign the three types of the boundary conditions in each of the flow domain cells, where Type 1 specified head boundaries are identified by assigning cells negative values (suggested to use -1) to represent constant head boundaries, which is classified as fixed-head cell in Processing Modflow Pro (PM5), and positive values (suggested to use 1) for variable head cell, which is classified as active cell in PM5. Type 2 used only for no flow boundaries in MODFLW and takes value of (0) and classified as inactive cell in PM5. While type 3 boundaries identified by General-Head boundary, river, reservoir, and drainage from packages menu in PM5.

MODFLOW selects specified head conditions over specified flow because it is easier to measure head than to measure flow. Also specified head conditions are helpful in achieving the calibration.

Depending on the map of the groundwater flow pattern of the B2/A7 aquifer the boundary conditions for the Amman Zarqa Basin is shown in Fig. 4 where the numbers in it refer to the following points:

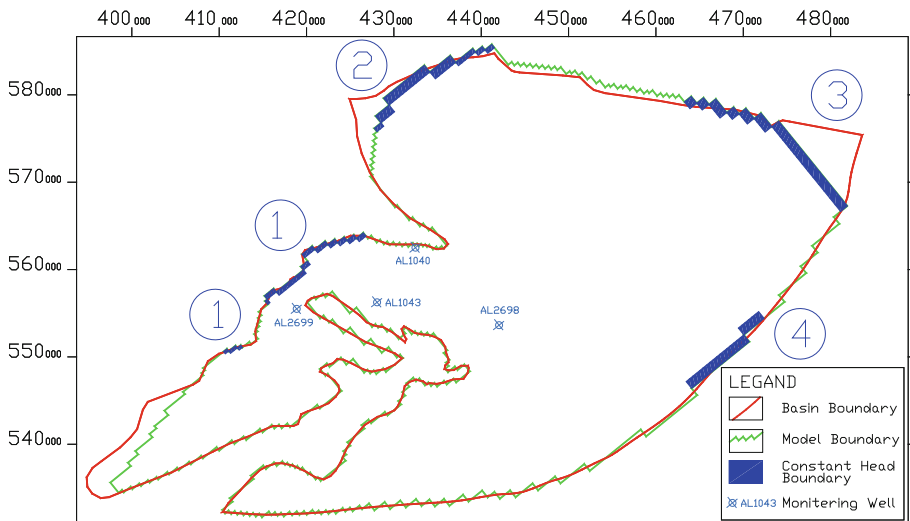


Fig. 4. Flow model boundaries and grid for Amman Zarqa Basin (B2/A7 and Basalt Aquifer)

1. The western side is defined as a specified head boundary where groundwater flows out to Zarqa River.
2. Another discharge side from the Amman Zarqa Basin is in the northern side, where groundwater feeding Yarmouk Basin, it is also defined as a specified head boundary.

3. The Arab Mountain in the east north is an important recharge source for Amman Zarqa Basin, it is considered as a specified head boundary.
4. Southern side of the Amman Zarqa Basin is also major outflow boundaries toward Azraq basin, where they are defined as a specified head boundary.

2.2.4 Initial Conditions

The initial conditions describe the distribution of heads (or pressures) and concentrations throughout the model domain at the start of the simulation. The initial condition in steady state condition is the head distribution within the model area at initial time. The initial conditions supplied to a transient run should be the result of a steady state flow or transient flow and transport simulation of background flow and transport conditions, which will give a mass balance starting point.

However, there are two types of steady state solutions that can be used as initial conditions: static steady state and dynamic average steady state simulation. The first type indicates conditions without any external stresses (well extractions) on the model, while the second type indicates conditions with some external stresses, which is most frequently used as initial conditions in groundwater simulation as this type is more available than the first one. Figure 5 shows the water level map for Amman Zarqa Basin created from the initial water level in the wells during the sixties where the extraction quantities still minor, which can be considered as a static steady state condition with acceptable error to represent the initial head distribution at the late sixties for Amman Zarqa Basin.

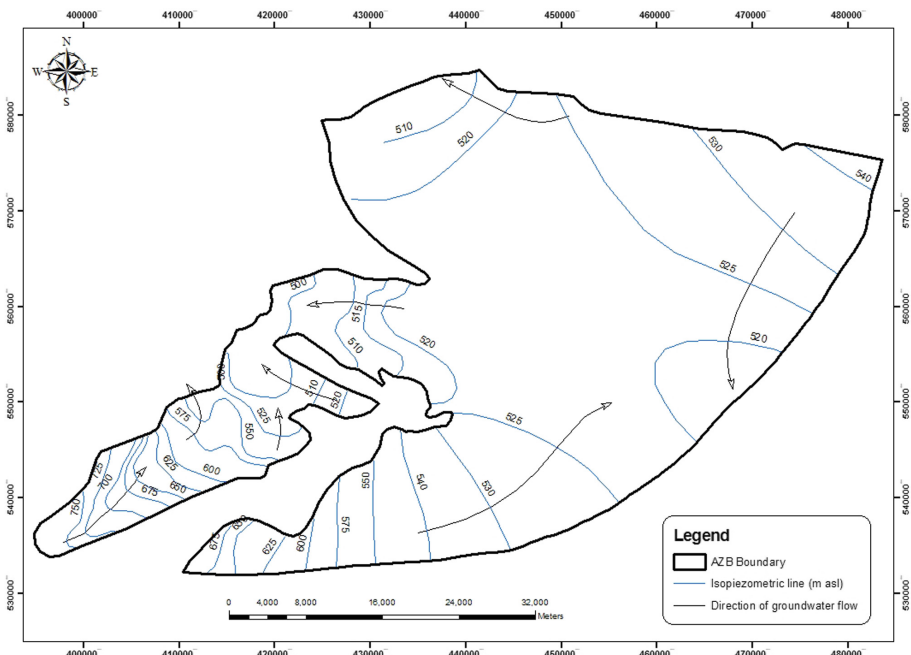


Fig. 5. Ground water flow pattern and water level map for Amman Zarqa Basin used as initial condition in the model application.

3 Results and Discussion

Model calibration and validation are necessary and critical steps in any model application. For most groundwater models, calibration is an iterative procedure of parameter evaluation and refinement, as a result of comparing simulated and observed values of interest. Model validation is in reality an extension of the calibration process. Its purpose is to assure that the calibrated model properly assesses all the variables and conditions which can affect model results, and demonstrate the ability to predict field observations for periods separate from the calibration effort (Donigian 2003). The calibration and validation phases are especially critical since the outcome establishes how well the model represents the basin.

3.1 Steady State Calibration

The steady state condition is a condition that existed in the aquifer before any development had occurred. Match the initial heads observed for the aquifer with the hydraulic heads simulated by MODFLOW is called steady state calibration that is done by sequential adjustment of the model parameters.

In the early stage of the model building, modifications were made to the thickness of the B2/A7 aquifer for some parts of the Amman Zarqa Basin, where after entering the first contour maps of the base and top of the aquifer to the model, there are some areas in the model especially in the western part with low thickness or even with negative one, while the wells information show that the thickness of the aquifer is much more. These errors in thicknesses are mostly due to the interpolating errors during maps building, and presence of some wrong information that are used to build the maps (errors in field measurements, information handling, etc.). This was done as an essential step in the early stage of the calibration process so as to ensure the reliability of the input data, especially in the hydrological maps where high source of errors are existed, and also to make the MODFLOW run properly.

Hydraulic conductivities, those estimated from previous studies and from pumping tests were used as initial values for the steady state simulation. By using the trial and error calibration, the horizontal hydraulic conductivity was adjusted during many sequential model runs until the match between the observed and simulated heads were obtained. Also minor adjustments were done on the boundary conditions that are firstly used in the initial runs. A comparison of measured and simulated water level contours of the B2/A7-Basalt aquifer is presented in Fig. 6. It is clearly shown that there is a good match between the simulated and measured heads. The values of the calibrated horizontal hydraulic conductivity are ranged between 1 m/d and 10 m/d, the maximum value of the calibrated hydraulic conductivity was occurred in the middle of the basin where it reached 45 m/d, while the minimum value reached 0.007 m/d to the west of Amman Zarqa Basin. As the simulation was done on one layer with an impermeable bottom, no vertical hydraulic conductivity is required to be calibrated.

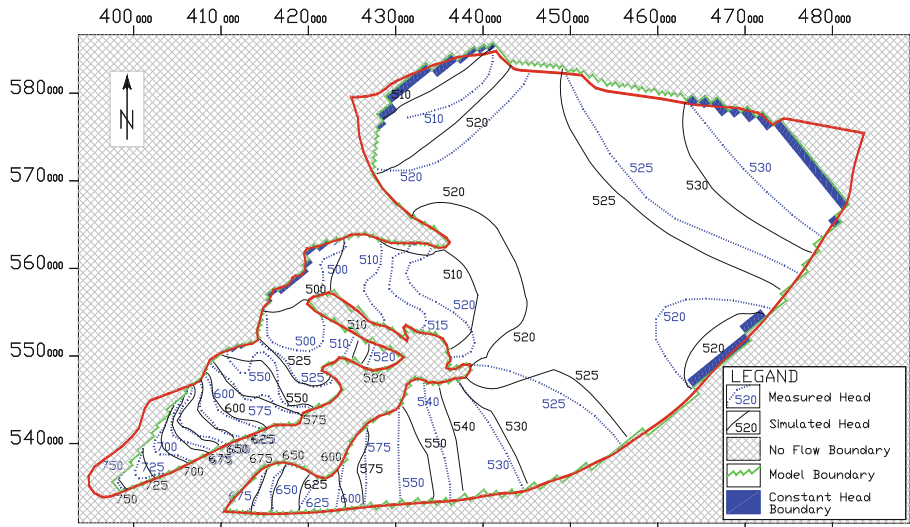


Fig. 6. Map of the measured and simulated water levels for the B2/A7-Basalt aquifer (Steady state calibration)

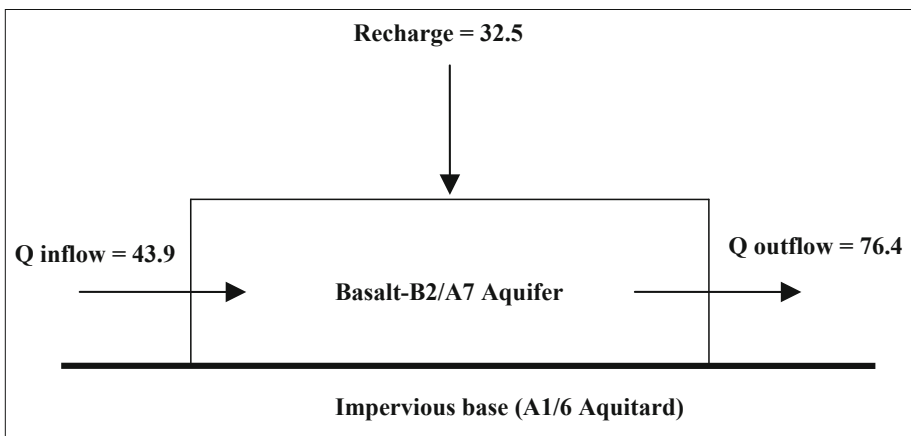


Fig. 7. Water Balance of the model domain at the steady state conditions (units in MCM/year)

Figure 7 shows the water balance for the Basalt-B2/A7 aquifer system in AZB at steady state condition where the calibrated outflow is exceeded the inflow by 32.5 MCM. The inflow comes from Arab Mountain in the east north of AZB which indicated by number (3) in Fig. 7 with about 43.9 MCM. The major outflows from the B2/A7 aquifer system are toward Azraq Basin (indicated by number 4) with about 37.2 MCM, and toward Zarqa River (indicated by number 1) with about 29.9 MCM, in addition to 9.3 MCM discharge toward Yarmouk Basin (indicated by number 2).

Accordingly, the water balance for steady state condition of B2/A7 aquifer in the AZB can be summarized as follows: the total annual direct recharge is 32.5 MCM, the total annual inflow (from Arab Mountain in the east north of AZB) is 43.9 MCM, and total annual outflow is 76.4 MCM. Major outflows from the B2/A7 aquifer system are toward Azraq Basin (37.2 MCM), and toward Zarqa River (29.9 MCM), in addition to (9.3 MCM) discharge toward Yarmouk Basin.

3.2 Model Evaluation

Contour maps of measured and simulated heads provides a visual, qualitative measure of the similarity between patterns, but they also include errors introduced by contouring and therefore should not be used as the only proof of calibration. A histogram of residual heads of model cells is another way of showing the calibration fit as shown in Fig. 8, where there is a balanced distribution of residuals around zero and most of the residual heads are located between 5 m and -5 m. It is clear that the distribution of the histogram is almost normal around zero with an average residual of 0.56 m, where ideally it should be zero.

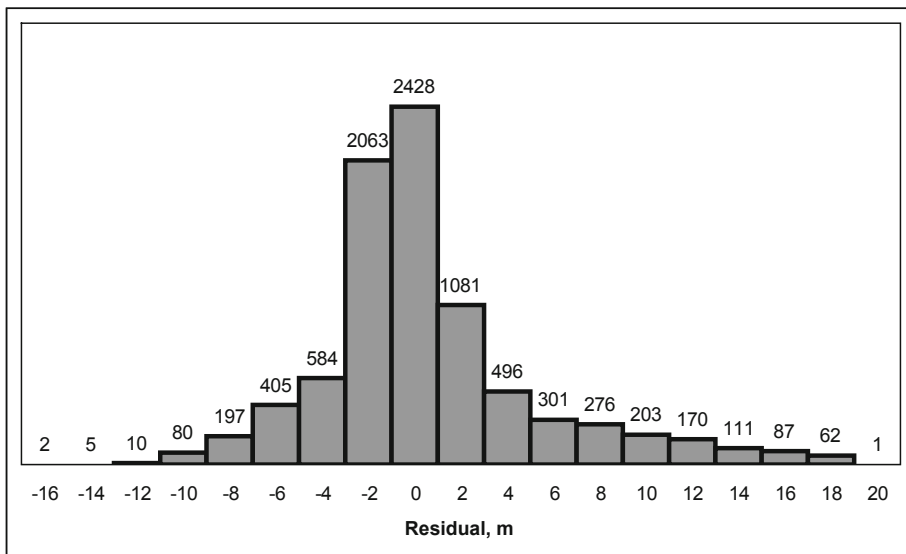


Fig. 8. Histogram of residual heads (observed minus calibrated) (m)

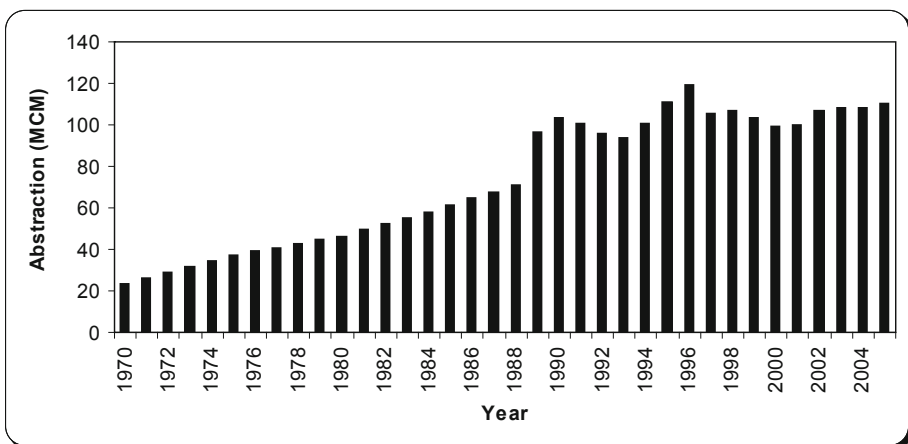
As shown graphically, the calibrated heads of steady state prove good fit with the observed heads, in addition Table 1 summarized some measures of the goodness of fit between observed and predicted heads and compared model values with the ideal ones. These also provide quantitative measures of the calibrated heads in addition to the visual and qualitative measures that are presented previously.

Table 1. Measures of fit between observed and predicted heads for steady state calibration

Measure/item	Max. residual	Min. residual	Mean error	Mean absolute error	R2
Model value	19.18	-16.31	0.56	3.30	0.994
Ideal value	0.0	0.0	0.0	0.0	1.0

3.3 Abstraction

Annual abstraction for the Amman Zarqa Basin was obtained from the Water Authority of Jordan (WAJ). These data represent the abstraction records for AZB wells for the time period that extends from 1989 to 2004 for all the basin aquifers. Abstraction data provide by WAJ for the period before 1989 is not complete. Accordingly, the total well abstractions for the years 1965, 1970, 1975, 1980, 1985, 1990, 1995 were obtained from a study conducted by MWI (2001) on AZB entitled of “hydrological impacts of over-pumping and assessment of groundwater management options in the Amman Zarqa highlands”. Then, linear interpolation using these data was used to find the abstraction records for the missing years of abstractions. Figure 9 shows the modified abstraction data.

**Fig. 9.** Modified abstraction data for Amman Zarqa basin for the years from 1989 to 2004.

3.4 Recharge

Estimation of the natural recharge is probably the most difficult parameter to estimate due to the many factors that affect on this process. Although there are many methods to estimate the recharge quantity but most of them required detailed and accurate data to get an acceptable estimation. Different methods to predict the recharge quantities were used. The method that gave a recharge values close to the surface water model and the previous studies for AZB was the Soil Conservation Service (SCS) method.

The evaporation through the rainfall storm assumed equal to zero. Amman Zarqa basin was divided into zones according to the Thiessen polygon method. Rainfall gauging stations that have a good time series records were chosen. Also, the basin coverage was taken into consideration in choosing the useful rainfall stations. The curve number values were taken for each sub-catchment according to the soil type, land use and many other factors. By application of the SCS method and rainfall data, a monthly recharge was calculated and used as input to the model.

3.5 Transient Calibration

Transient calibration step comes after finishing steady state calibration step, where successful transient calibration step depends on the good results obtained from the steady state calibration step mainly hydraulic conductivities and boundary conditions. Typically specific yield for unconfined aquifers and storage coefficient for confined aquifers are the main parameters that are changed during the transient calibration in order to get calibrated model.

The year of 1970 was considered as the year in which significant water production started. From 1970 to 1979, one stress period was selected to cover each successive two years with 2 time steps each. The period from year 1980 until year 2005 was divided into 52 stress periods, where each year was split into two stress periods, so that the natural recharge is only occurred in the first one and its length is 152 days (5 months) with 5 time steps, while no recharge is occurred in the second stress period which length is 213 days (7 months) with 7 time steps. It is assumed that wells discharges have the same rates over the year.

The transient-state model was calibrated using available water-level data from 4 wells that differ in the monitoring start year, which vary from 1970 to 1988. The water level data for the wells was divided into two parts: the first part of the data used for calibration while the second part used for validation. The calibration period extends from the monitoring start year till 1995 for monitoring wells no. AL1040 and AL1043 and to 1998 for monitoring wells no. AL2698 and AL 2699. The remaining part of the data is left for the validation process. The transient-state simulation was assumed to be calibrated when the simulated water levels are in good agreement with the observed water levels.

The transient calibration was firstly done by assigning initial values of the specific yield to the model layer, these values are taken from previous studies, then by performing several computer runs in which the initial values of the specific yield were changed several times until acceptable matches/fit were obtained between the observed and simulated water levels drawdowns. The range of the resulted specific yield after the final calibration of the transient state is from 0.001 to 0.15.

Figures 10a, 10b, 10c and 10d show the comparison between observed and calculated hydraulic head in the observation wells where their drawdowns are highly affected mainly by the groundwater withdrawals and slightly by the natural recharge variation resulted from rainfall fluctuation. It can be seen that there is a good agreement between the observed and simulated drawdowns.

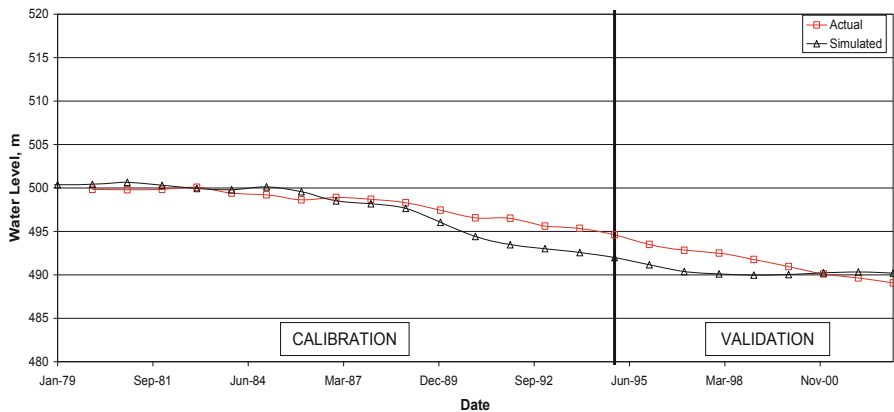


Fig. 10a. Comparison between observed and simulated hydraulic head (AL1040)

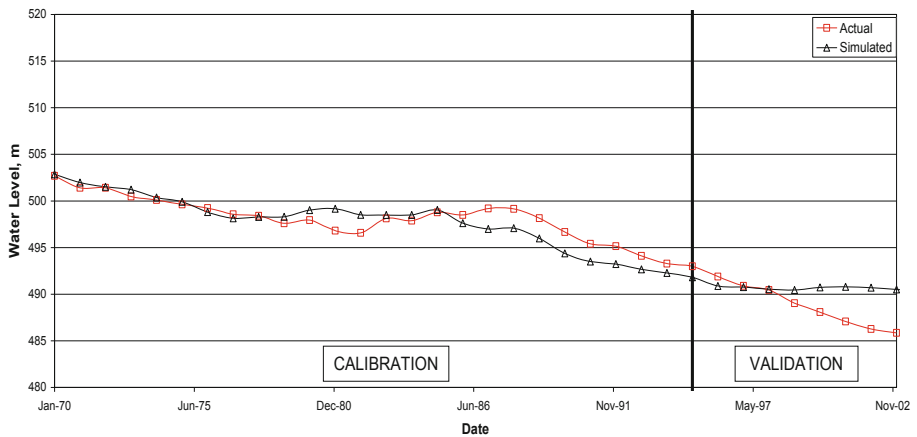


Fig. 10b. Comparison between observed and simulated hydraulic head (AL1043)

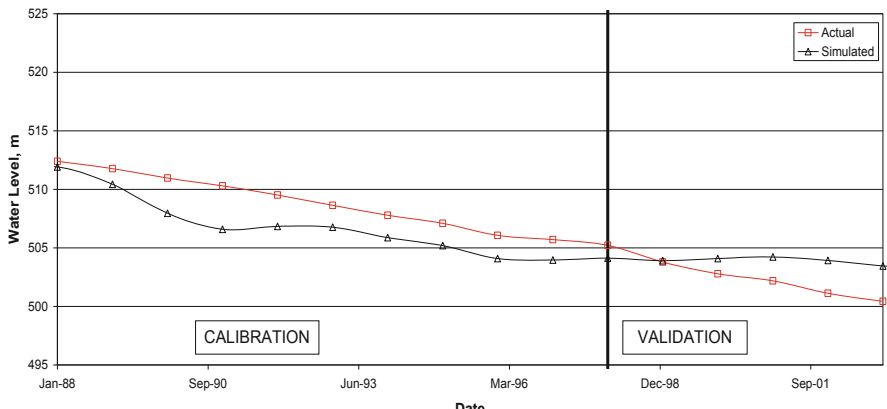


Fig. 10c. Comparison between observed and simulated hydraulic head (AL2698)

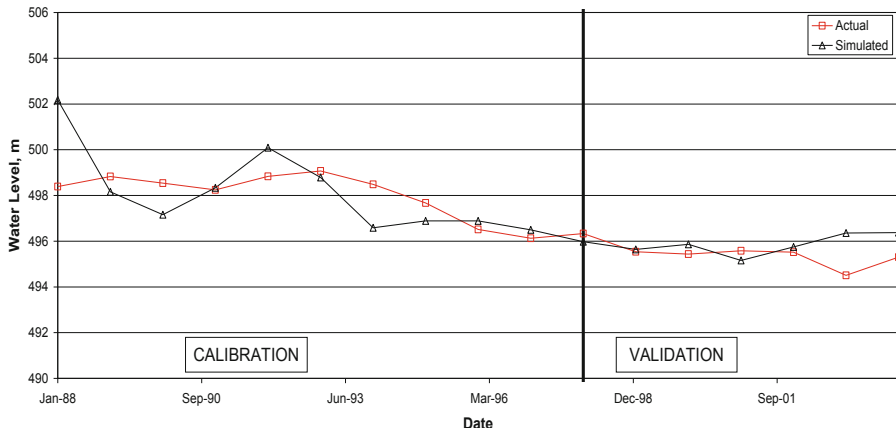


Fig. 10d. Comparison between observed and simulated hydraulic head (AL2699)

Model validation is in reality an extension of the calibration process. Its purpose is to assure that the calibrated model properly assesses all the variables and conditions which can affect model results. While there are several approaches to validating a model, perhaps the most effective procedure is to use only a portion of the available record of observed values for calibration; once the final parameter values are developed through calibration, simulation is performed for the remaining period of observed values and goodness-of-fit between recorded and simulated values is reassessed. This type of split-sample calibration/validation procedure is commonly used, and recommended, for many groundwater flow modeling studies. Model credibility is based on the ability of a single set of parameters to represent the entire range of observed data. If a single parameter set can reasonably represent a wide range of events, then this is a form of validation (Donigian 2003).

The observation wells that have water levels data beyond year 1995 were used to validate the transient calibration results. From the previous figures it can be noticed that good match between observed and calculated hydraulic head for the monitoring wells used in the validation process.

Transient calibration is also evaluated quantitatively where some measures of goodness of fit between observed and predicted drawdown for calibration stage are presented in Table 2 and for validation stage are presented in Table 3. These quantitative measures give another way to evaluate transient calibration results over the visualized one presented in the previous figures. Generally, these measures show that the fit between measured and simulated heads for the calibration stage is better than validation stage which is expected.

Table 2. Measures of fit between observed and predicted heads for transient state (Calibration stage)

ID	Residual Max.	Residual Min.	ME	MAE	R2
AL1040	3.05	-0.94	0.76	1.28	0.98
AL1043	2.29	-2.36	0.33	1.06	0.92
AL2698	3.71	0.47	1.97	1.97	0.94
AL2699	1.90	-3.79	-0.05	1.02	0.57
Ideal value	0.0	0.0	0.0	0.0	1.0

Table 3. Measures of fit between observed and predicted heads for transient state (Validation stage)

ID	Residual Max.	Residual Min.	ME	MAE	R2
AL1040	2.44	-1.13	0.99	1.48	0.47
AL1043	1.00	-4.64	-1.98	2.26	0.29
AL2698	-0.11	-3.01	-1.85	1.85	0.57
AL2699	0.42	-1.85	-0.44	0.68	-0.71
Ideal value	0.0	0.0	0.0	0.0	1.0

3.6 Management Scenarios

Three different scenarios were conducted to predict the drawdown for the B2/A7 aquifer of the AZB during the period (2020–2030). These scenarios are explained below.

- **Scenario No.1** (No reduction of current withdrawal rate or 110.4 MCM/year).

In this scenario, it is assumed that the pumping rates of year 2005 are constant for 15, and 25 years. The maximum drawdowns were concentrated in the well field areas, where they reached about 99.9 and 104.9 m in the years 2020, and 2030 respectively. The drawdown levels are shown in Figs. 11a and 11b.

- **Scenario No.2** (30 MCM reduction of the withdrawal rate or 80 MCM/year)

The present abstraction rates of about 110.4 MCM/year will be reduced by 30 MCM to 80 MCM/year. The maximum drawdowns were decreased to reach about 90, and 94.8 m in the years 2020 and 2030 respectively.

- **Scenario No.3** (45 MCM reduction of current withdrawal rate or 65 MCM/year)

The present abstraction rates of about 110.4 MCM/year will be reduced by 45 MCM to 65 MCM/year. The maximum drawdowns were decreased to reach about 76.8, and 72.5 m in the years 2020 and 2030 respectively.

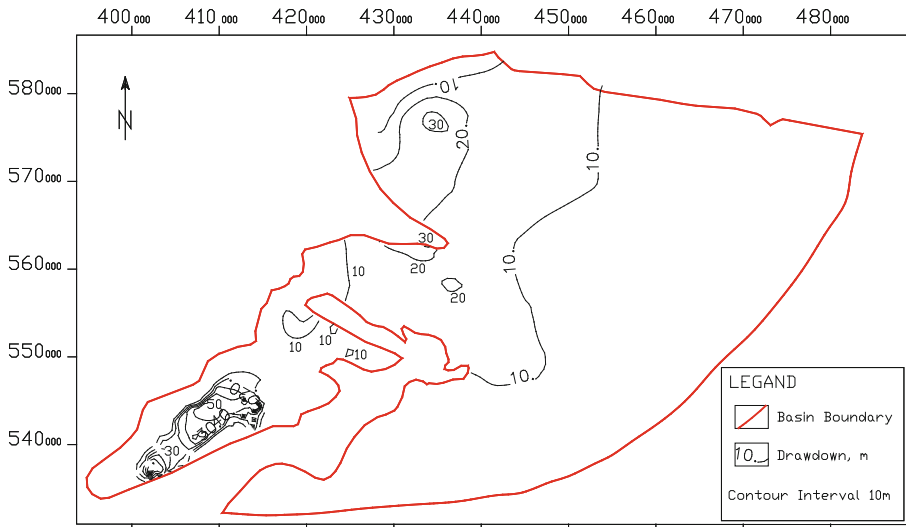


Fig. 11a. Drawdown of year 2020 for Scenario 1.

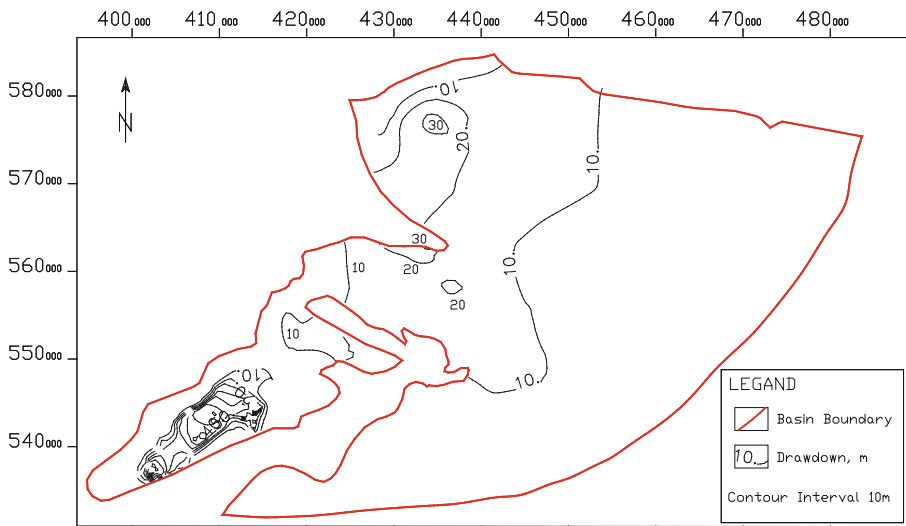


Fig. 11b. Drawdown of year 2030 for Scenario 1.

In this scenario it can be noticed that there are some kind of recovery in water drawdown in the early period and then some kind of stability in drawdown, so that abstraction rate of 65 MCM could be considered as the safe yield with this current pumping distribution. This can also be ensured when referring to the abstraction rates before 1986 which was around 65 MCM as drawdown in the observation wells were almost very small.

4 Conclusions

The MODFLOW model was calibrated for steady state condition for Amman-Zarqa Basin by matching observed and simulated initial head counter lines, using drawdown data for the period 1985–1995. The transient model was then validated using the drawdown data for the period 1996–2002. Results of the calibrated flow model (steady and transient states) indicate that the horizontal hydraulic conductivity of the B2/A7 aquifer system in AZB ranges between 0.007 to 45 m/d. The calibrated specific yield values range between 0.0001 and 0.15. The water balance for steady state condition of B2/A7 aquifer in the AZB can be summarized as follows:

- Total annual direct recharge is 32.5 MCM, Total annual inflow (from Arab Mountain in the east north of AZB) is 43.9 MCM,
- Total annual outflow is 76.4 MCM. Major outflows from the B2/A7 aquifer system
 - toward Azraq Basin (37.2 MCM),
 - toward Zarqa River (29.9 MCM),
 - 9.3 MCM discharge toward Yarmouk Basin.

Three scenarios were conducted to predict the B2/A7 aquifer system response under different conditions during the period 2005–2030:

- The first scenario assumed that the pumping rates of year 2005 are constant for 15, and 25 years. The maximum drawdowns were concentrated in the well field areas, where they reached about 99.9 and 104.9 m in the years, 2020, and 2030 respectively.
- The second scenario assumed that the present abstraction rates (110.4 MCM/year) will be reduced to 80 MCM/year. The maximum drawdowns were decreased to reach about 90, and 94.8 m in the years 2020 and 2030 respectively.
- The third scenario assumed that the present abstraction rates of about 110.4 MCM/year will be reduced to 65 MCM/year. The maximum drawdowns were decreased to reach about 76.8, and 72.5 m in the years 2020 and 2030 respectively.

The third scenario provides recovery and stability in the drawdown, therefore, the abstraction rate of 65 MCM could be considered as the safe yield of AZB

References

- Anderson, M.P., Woessner, W.W.: Applied Groundwater Modeling - Simulation of Flow and Advection Transport (1992)
- BGR/MWI: Groundwater Resources for Northern Jordan, vol. 4: Contribution to the Hydrogeology of Northern Jordan, Amman-Jordan (2001)
- BGR/WAJ: Groundwater Resources for Northern Jordan, vol. 5: Groundwater Modeling, Part 2: A Numerical Model of the Siwaqa-Qatrana-Hasa Well Field", Amman-Jordan (1998)
- BGR/WAJ: Groundwater Resources for Northern Jordan, vol. 1: Rainfall, Spring Discharge and Baseflow, Amman-Jordan (1996)
- BGR/WAJ: Groundwater Resources for Northern Jordan, vol. 3: Structural Features of the main Hydrogeological Units in the Northern Jordan, Amman-Jordan (1994a)

- BGR/WAJ: Groundwater Resources for Northern Jordan, vol. 2: Groundwater Abstraction
Groundwater Monitoring, Part 2: Monitoring of Groundwater Levels in Jordan, Amman-Jordan (1994b)
- BGR/WAJ: Groundwater Resources of South Jordan, Amman-Jordan (1989)
- Chiang, W.H., Kinzelbach, W.: Pre- and Postprocessors for Simulation of Flow and
Contaminants Transport in Groundwater Systems with MODFLOW, MODPATH and
MT3D, version 5, Hamburg, Heidelberg (1993)
- Donigian, A.S.: Watershed Model Calibration and Validation: the HSPF Experience,
AQUA TERRA Consultants (2003)
- Mercer, J.W., Faust, C.R.: Ground-Water Modeling: An Overview. *Ground Water* **18**(2), 108–
115 (1980)
- Spitz, K., Moreno, J.: A Practical Guide to Groundwater and Solute Transport Modeling. Wiley,
New York (1996)



A Density-Dependent Constitutive Model of Rockfill as Well as a Dynamic Contact Technique for Simulation of Dynamic Compaction with MPM

Ruiyu Zhang^(✉), Erxiang Song, Abbas Haider, and Yujin Sun

Department of Civil Engineering, Tsinghua University, Beijing, China
zrylltsinghua@163.com

Abstract. The mechanical behavior of rockfill under strong impact is highly nonlinear which results in grain breakage. In this paper, a simple but valid constitutive model for rockfill considering grain breakage is proposed and used to simulate the dynamic compaction process using material point method (MPM) which has proven to be suitable for large deformation problems. A useful dynamic contact algorithm is developed to achieve an automatic adjustment of the rigid body velocity so that the rigid model assumption of the hammer is still valid. The simulation results are verified using the test data from the construction site of Chengde Airport China. Later, the influence of soft substratum on the distribution of volumetric strain, volumetric compression plastic strain energy density and the historical maximum mean compressive stress in deep improvement zone is investigated. The usual ellipsoidal distributions of these three parameters are cut-off by the soft substratum and are observed to be semi-ellipsoidal in the soft substratum after dynamic compaction. There is a decrease of the volume compression plastic strain energy density and the historical maximum mean compressive stress under the interface, which is explained by a simple 1-D case where the stress wave is reflected and refracted on the interface of two different linear elastic materials.

Keywords: Rockfill · Dynamic contact · Grain breakage · Material point method · Dynamic compaction · Soft substratum

1 Introduction

Dynamic compaction is an economical and efficient ground improvement method. The basic thought of dynamic compaction is originated from ancient tamping method. As a modern ground treatment method, its formation and application dates from Menard and Broise (1976). Since then, this method has been widely applied in engineering practice.

Up to now, studies on dynamic compaction are mainly based on experiments and numerical simulations, where the finite element method is used for most of the numerical works (Ghassemi et al. 2010). When the traditional finite element method is applied to large deformation problems such as dynamic compaction, special computational techniques such as re-meshing and reassignment of material properties are

generally required (Poran and Rodriguez 1992). Recently, a new numerical method called the material point method (MPM) was proposed (Sulsky et al. 1994), which proves to be particularly suitable for simulating large deformation problems, hence it can be used to simulate the dynamic compaction process.

In previous theoretical analyses and numerical simulations of dynamic compaction, the mechanical behavior of soil was often regarded as elastic (Wang and Deng 1984) or viscoelastic (Chow et al. 1992). Some of the works also adopted relatively simple elastoplastic models like the MC model (Pan and Selby 2002). An elasto-plastic cap model was also adopted (Gu and Lee 2002) where, it is assumed that the plastic behavior of soil played a more important role than the elastic behavior, and the elastic modulus of soil was not updated during repeated strikes. However, soil under dynamic compaction will behave highly nonlinear, and its strength and stiffness will change significantly as its density is improved with the compaction process.

In this paper, a newly proposed soil constitutive model for rockfill is combined with an improved rigid-flexible contact algorithm and used to simulate the dynamic compaction process using MPM. A numerical model is first validated by the experimental results from the construction site of Chengde Airport China. Moreover, the influence of soft substratum on the dynamic compaction process is further investigated.

2 Methodology

2.1 Material Point Method

MPM was proposed by Sulsky et al. (1994) based on studies by Harlow and Evans (1955), Dawson (1983), Brackbill and Ruppel (1986). The advantages of the Lagrangian and Eulerian modelling techniques are combined in this method. The specific control equations, numerical processes and program implementations, are referred to related studies (Sun and Song 2015; Zhang et al. 2011).

For standard MPM method, there is numerical noise caused by material particles crossing the background grid boundary. Zhang et al. (2011) proposed a new method for calculating the shape function gradient. To reduce the stress oscillation caused by the material particles crossing the background grid boundary, the shape function gradient based on material particles in the standard material point method and the shape function gradient based on the background grid nodes in the fluid implicit particle method (FLIP) were weighted (Brackbill and Ruppel 1986). This method is called the dual domain material point method (DDMP).

In DDMP, the modified shape function gradient is as follows:

$$\hat{N}_{Ip,j} = \alpha(\mathbf{x}_p)N_{Ip,j} + [1 - \alpha(\mathbf{x}_p)]\hat{N}_{Ip,j} \quad (1)$$

$$\hat{N}_{Ip,j} = \sum_{J=1}^{n_g} \frac{N_{Jp}}{V_J} \int_V N_J N_{I,j} dV \quad (2)$$

where the subscript I denotes the background grid node, p denotes the material particle, and j denotes the direction; $N_{Ip,j}$ is the shape function gradient of standard MPM, and $\hat{N}_{Ip,j}$ is the shape function gradient based on the background grid nodes; $\alpha(\mathbf{x}_p)$ is a

weight function that is zero on background grid boundaries, to ensure the continuity of the modified gradient, whose specific expression is referred to studies of Zhang et al. (2011).

For DDMP, the influence domain of a material particle and of a node are enlarged, as a result, a node near the material boundary will get node force from material particles but no mass. To overcome this problem, a simple but effective method is used to distribute the node force of a node with no mass to surrounding nodes with mass (Ma et al. 2010). To overcome the numerical oscillations and accelerate the computational convergence, the energy minimization technique (Cundall 1976) and artificial damping (Kafafi 2013) are used.

2.2 Improved Rigid-Flexible Contact Algorithm

During dynamic compaction, soil is compacted by a high-speed falling hammer, and a complicated dynamic contact procedure between the hammer and soil is involved. Due to the much higher stiffness of the hammer than that of soil, the hammer can be considered as rigid, then the calculation efficiency can be greatly improved. Nevertheless, if a structure is regarded as rigid in basic format of MPM, its velocity cannot be adjusted automatically by the interaction between the two contact bodies. Nairn (2013) proposed a rigid-flexible contact algorithm, in which the rigid body velocity must be prescribed as constant in the entire calculation process.

Here, the rigid body velocity is adjusted automatically as follows. At the beginning of each time step, if contact is detected, the total mass and the total momentum of the background grid nodes belonging to the flexible body f contacting the rigid body r only are counted. Subsequently, this part of the flexible body f is considered as an equivalent particle to collide and then move together with the whole rigid body r . In this way, the rigid body velocity at the beginning of each time step can be determined.

$$v_{ri}^{k+1} = \frac{m_r v_{ri}^k + m_f^{k,\text{cont}} v_{fi}^{k,\text{cont}}}{m_r + m_f^{k,\text{cont}}} \quad (3)$$

in which m_r is the rigid body mass; v_{ri}^k and v_{ri}^{k+1} are, respectively, the rigid body speeds at time t^k and t^{k+1} ; $m_f^{k,\text{cont}}$ and $v_{fi}^{k,\text{cont}}$ are, respectively, the total mass and equivalent velocity of the part belonging to the flexible body f contacting the rigid body only.

In this algorithm, the two contact bodies are allowed to be separated, while the relative slip between them is not allowed, on account that if the relative slip is allowed, the rigid body r and the part belonging to the flexible body f contacting the rigid body only cannot move together after the collision. Though there is the problem mentioned above, this algorithm is still suitable for simulating the procedure of dynamic compaction. In accordance with the field observations of Wang and Deng (1984), the relative slip between the hammer and soil is very small, so neglecting its influence is reasonable.

2.3 Density-Dependent Soil Constitutive Model

Rockfill behaves highly nonlinear under strong impact, and the grain breakage will occur obviously. A simple but valid model for rockfill considering grain breakage is

proposed based on the relationship between the void ratio and the mean compressive stress given by Baur (1996) and Gudehus (1996):

$$e = e_0 \exp\left[-\left(\frac{3p}{h_s}\right)^n\right] \quad (4)$$

In this model, the hardening of soil and the change of elastic modulus with variation of density can be considered. For details about the specific model, the reader is referred to our previous study (Zhang et al. 2019). In this model, 8 parameters need to be calibrated as shown in Table 1, and two parameters will influence the grain breakage degree, as shown in Figs. 1 and 2.

Table 1. Parameters of density-dependent soil constitutive model

Parameter symbol	Parameter name
e_0	Initial void ratio
h_s	Particle hardness
m	Stiffness pressure correlation index ($1 - n$)
k_{ul}	Ratio of unloading modulus to loading modulus
ν	Poisson's ratio
c	Cohesion
φ	Friction angle
ψ	Dilatancy angle

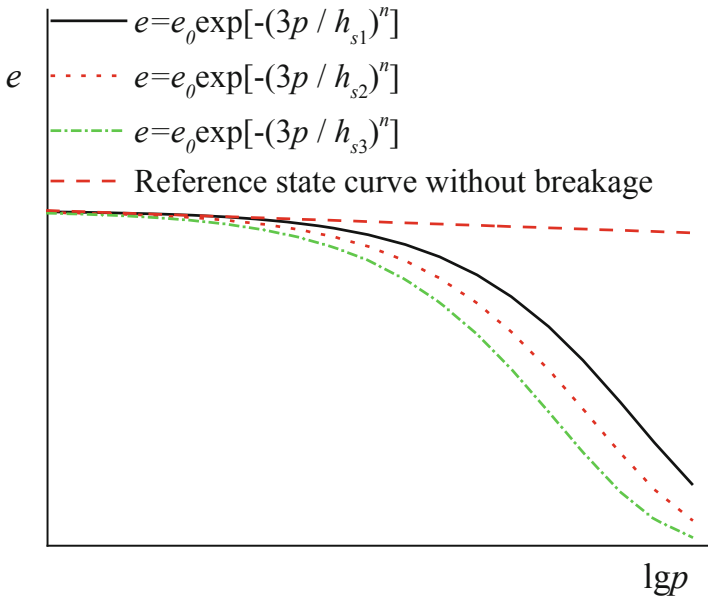


Fig. 1. $h_{s1} > h_{s2} > h_{s3}$

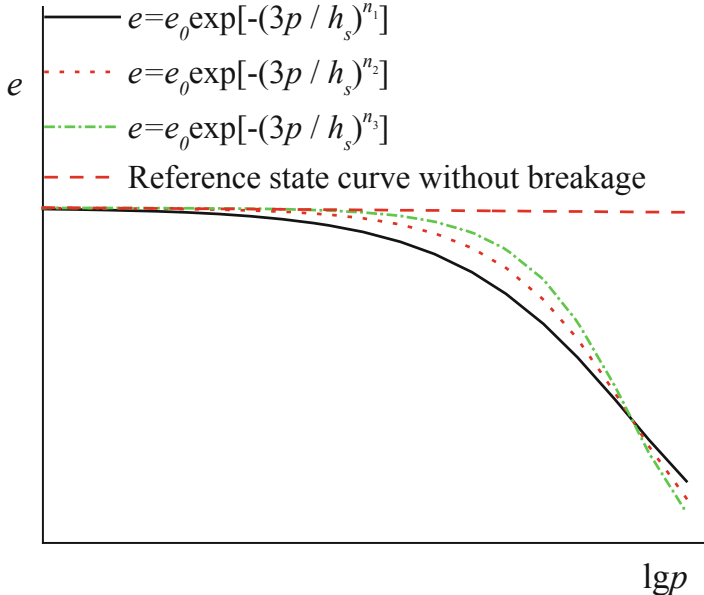


Fig. 2. $n_3 > n_2 > n_1$

3 Numerical Examples

3.1 Validation

To validate the proposed numerical model, the field test data from the construction site of Chengde Airport China was adopted where the filler was rockfill. The hammer bottom diameter was 2.25 m and its mass was 20 ton. The drop height of the hammer was 6.0 m, and the tamping energy was 1200 kN·m. Here, the results of the first 9 strikes are collected and analyzed. The crater depth of each strike is decreased on the whole, while a slightly sudden increase in the fifth strike may be due to the abrupt breakage of large particles. It is necessary to revise the abnormal data which is difficult to be explained by continuum mechanics, so the average value of the 4th and 6th strike is taken as that of the 5th strike. The corrected cumulative crater depth is shown in Fig. 3.

The middle rectangular area is selected for the simulation. As the boundary is relatively far from the hammer, the boundary influence can be negligible. Hence, the boundary is taken as symmetric. To reduce the computational cost of the simulation, only one quarter of the test area is modeled. The dimensions of the numerical model are shown in Fig. 4. The calculation cell of the background grid adopted is 0.2 m × 0.2 m × 0.2 m. For soil, the initial distance between the material particles within 2 m from the axis of the hammer is set to be 0.05 m, while the initial distance between the material particles outside this area is set to be 0.1 m. For the hammer, the initial distance between the material particles is set to be 0.025 m.

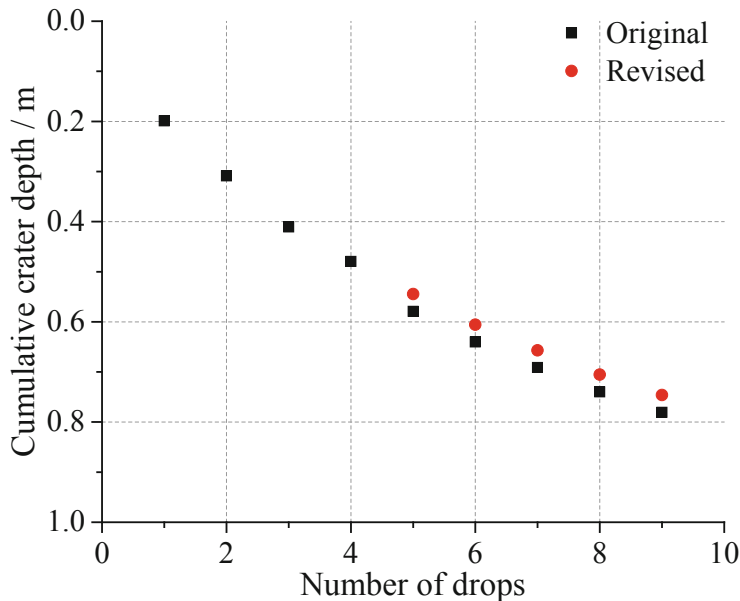


Fig. 3. Cumulative crater depth

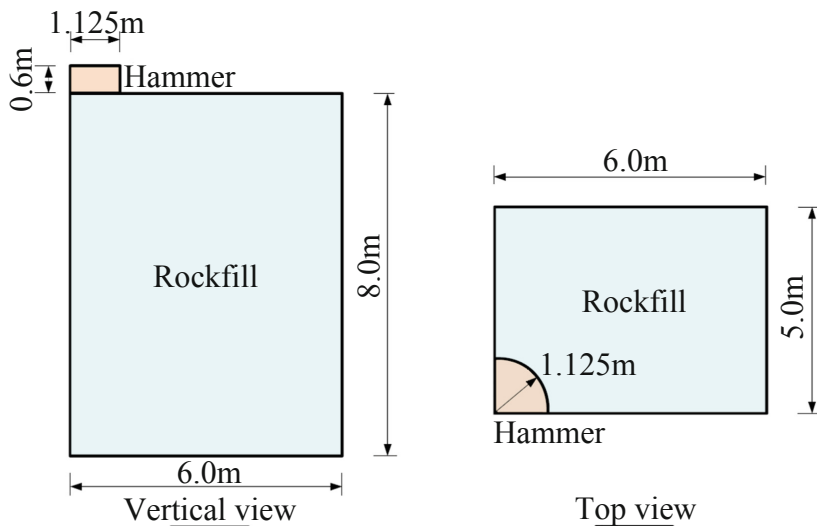


Fig. 4. Profiles of the numerical model

The material parameters are shown in Table 2. h_s and m are determined by back analysis of the crater depths of the first 2 strikes in the field test. Comparison between numerical simulation results and the measured results in the field test is shown in Fig. 5. The results at each strike predicted are consistent with the results of the field

test. It shows that the constitutive model of soil and the numerical simulation technique proposed can well reflect the main characteristics of the rockfill during the dynamic compaction process.

Table 2. Material parameters of soil

Parameter	e_0	h_s/MPa	m	k_{ul}	v	c/kPa	$\varphi/^\circ$	$\psi/^\circ$
Value	0.5	2600	0.7	8.0	0.3	5	35	0

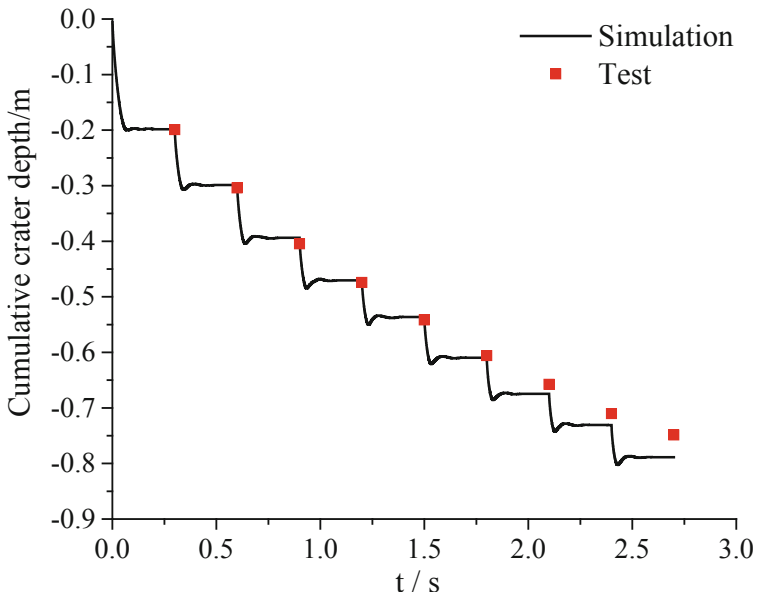


Fig. 5. Comparison between the numerical simulation and the field test

3.2 General Mechanism

The soil improvement zone can be divided into a deep improvement zone DIZ and a surface improvement zone SIZ, as shown in Fig. 6. DIZ is also the main improvement zone, which is mainly compacted due to the longitudinal compression effect of body waves. SIZ is slightly compacted due to the action of the surface wave and lateral compression. The volumetric strain distribution in DIZ is approximately ellipsoidal. This is consistent with the studies of Yao and Zhang (2016) and Poran and Rodriguez (1992). As shown in Figs. 7 and 8, the distribution of the volume compression plastic strain energy density as well as the historical maximum mean compressive stress is also ellipsoidal, the same as that of the volumetric strain in DIZ, and the downward trend is more pronounced than the trend toward the lateral direction.

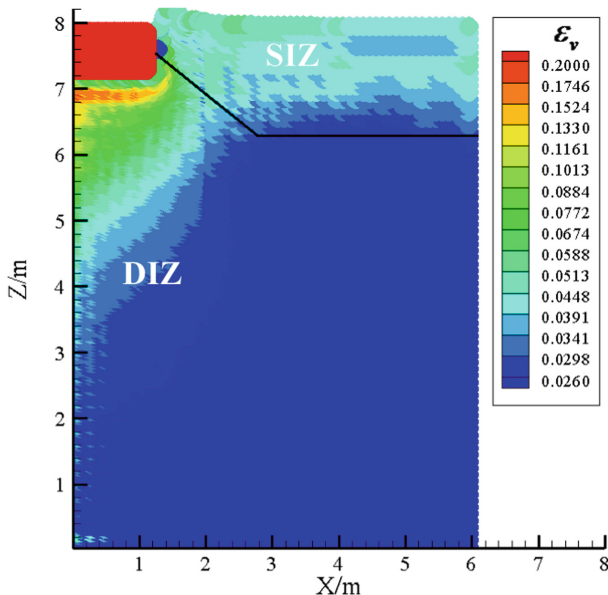


Fig. 6. Distribution of volumetric strain

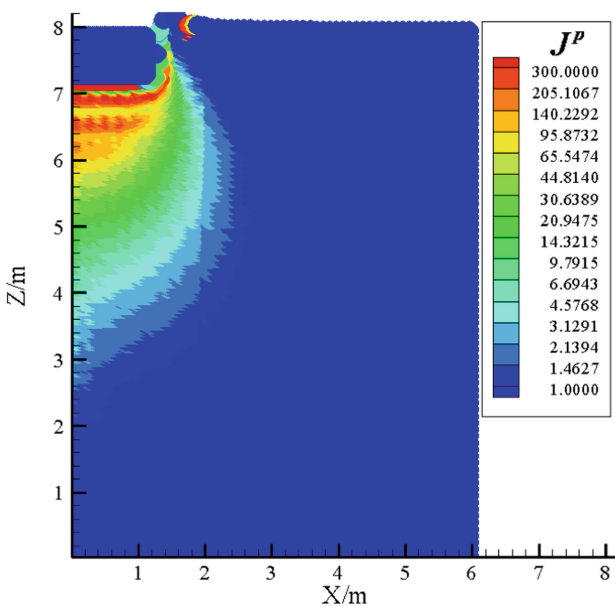


Fig. 7. Distribution of volume compression plastic strain energy density

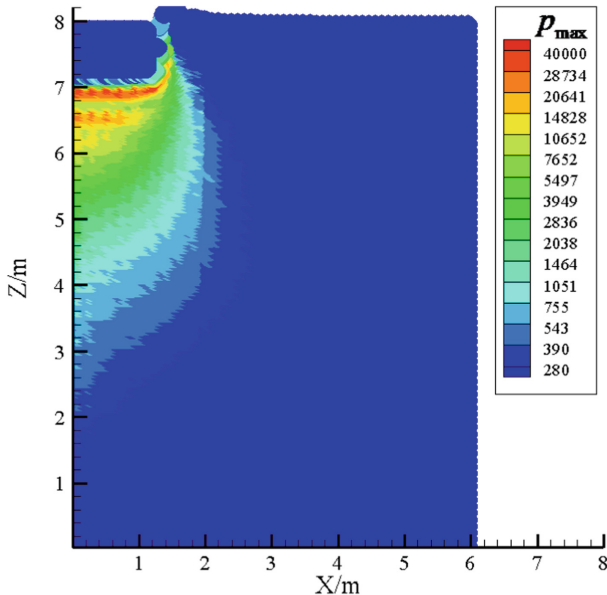


Fig. 8. Distribution of historical maximum mean compressive stress

3.3 The Influence of the Soft Substratum

In this section, the influence of the soft substratum (SS) in dynamic compaction is roughly investigated. The overlying soil layer is 3 m deep, and its material parameters are the same as that in Table 2, while h_s of SS is changed to 200 MPa.

The presence of SS increases the crater depth, and as the number of drops is increased, the crater depth increment is also increased, as shown in Fig. 9. The difference value between the settlement of the overlying soil layer relative to that of the SS is referred to herein as the relative crater depth. The presence of SS has little effect on the relative crater depth, which indicates that when there is a SS, the increase in the crater depth is mainly due to the settlement of SS.

SS is easily deformed, so obvious volumetric strain has already been generated under the gravity of the overlying soil layer, as shown in Fig. 10. The volumetric strain ellipsoid of the deep improvement zone I in Fig. 6 is cut off by SS as shown in Fig. 10. In the main area affected by dynamic compaction in SS, the volumetric strain distribution is also approximately semi-ellipsoidal. The influence of SS on the distributions of the volume compression plastic strain energy density and the historical maximum mean compressive stress in the soil is more or less the same as that on the volumetric strain, as shown in Figs. 11 and 12. It is worth noting that, when the dynamic compaction influence radius is changing along the depth, there is a sudden increase in SS.

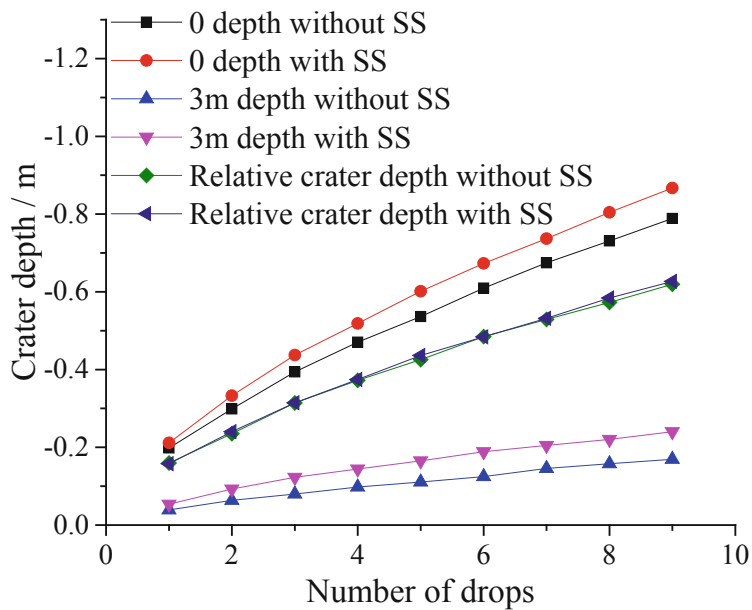


Fig. 9. Influence of SS on crater depth

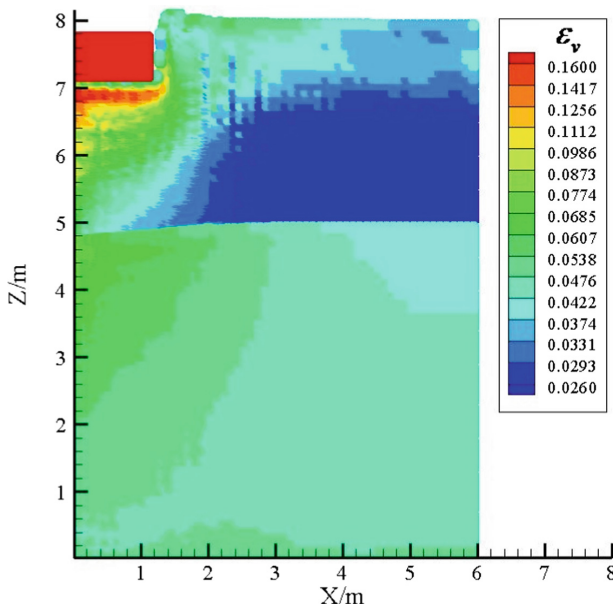


Fig. 10. Distribution of volumetric strain with SS

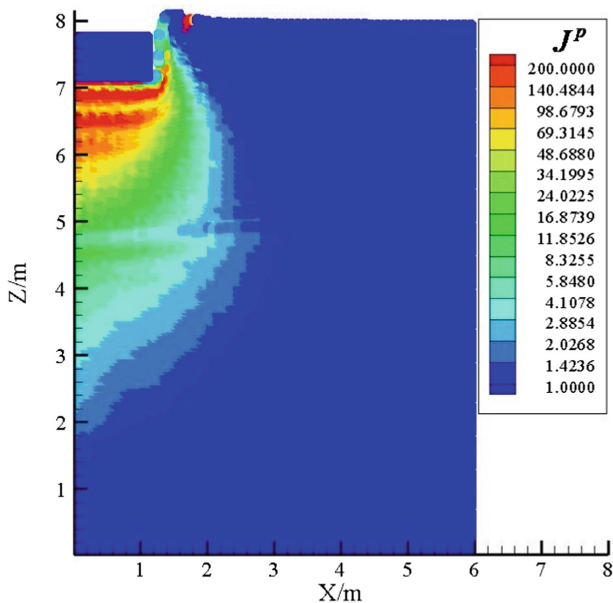


Fig. 11. Distribution of volume compression plastic energy density with SS

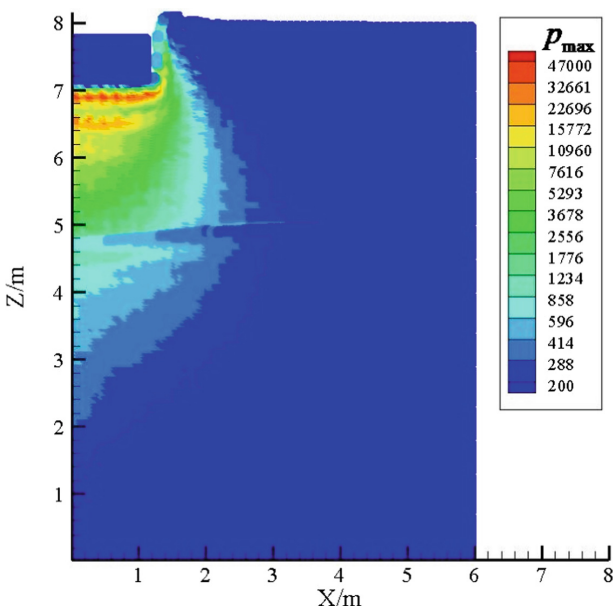


Fig. 12. Distribution of historical maximum mean compressive stress with SS

3.4 A Simple Theoretical Explanation

A simple 1-D case where the stress wave propagates in two different linear elastic materials separated by an interface, is investigated. Due to the reflection and refraction of the stress wave on the interface, the accurate stress expression in small deformation condition here should be as follows:

$$\sigma_{reflec} = R_\sigma(\sigma_1 - \sigma_0) \quad (5)$$

$$R_\sigma = \frac{k - 1}{k + 1} \quad (6)$$

$$\sigma_{refrac} = T_\sigma(\sigma_1 - \sigma_0) \quad (7)$$

$$T_\sigma = \frac{2k}{1 + k} \quad (8)$$

$$k = \frac{\rho_2 c_2}{\rho_1 c_1} \quad (9)$$

where, the subscript 1 denotes the material through which the stress wave passes first; 2 denotes another material through which the stress wave passes last; σ_1 is the incident stress; σ_0 is the initial stress of one point; σ_{reflec} is the reflection stress on the interface induced by the incident stress; σ_{refrac} is the refraction stress on the interface induced by the incident stress; ρc is called wave impedance.

As shown in Eqs. (7–11), if the wave impedance of material 2 is smaller than material 1, then the refraction stress will be smaller than the incident stress. If the wave impedance of material 2 is half of that of material 1, and the incident stress is 90 kPa, then the result is just as shown in Fig. 13, in which the reference stress is the stress at the same point in single elastic material 1. This is just a simple representation of the case of soft substratum. As shown in Figs. 11, 12, there is a decrease of the volume compression plastic strain energy density and the historical maximum mean compressive stress under the interface. After an obvious decrease, there is a small increase, and then the value gradually decreases continuously. The increase is due to the subsequent refraction stress wave which becomes faster and superposes with the front refraction stress wave. The effect of the reflection stress wave on the overlying layer is very small, which maybe is due to that the reflection stress in the overlying layer is absorbed quickly in a very short distance.

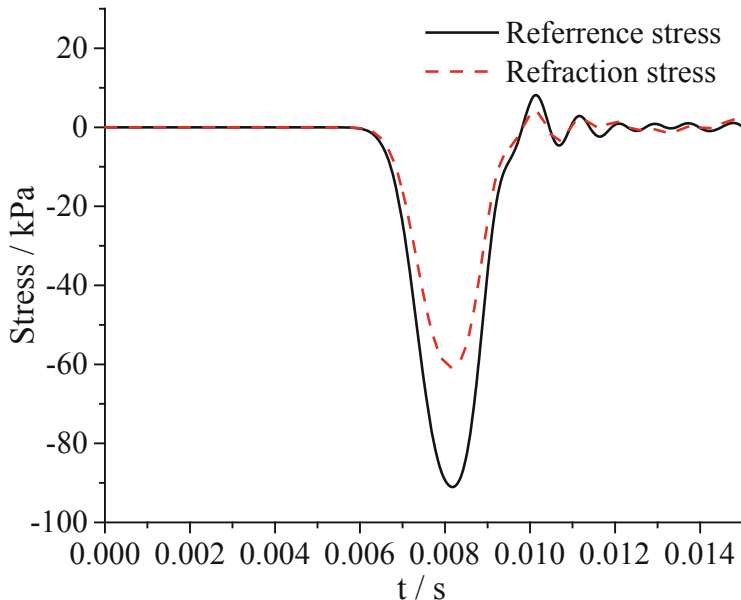


Fig. 13. Refraction stress in a simple soft substratum case

4 Conclusions

This work proposes a simple but valid constitutive model for rockfill considering grain breakage. It has been adopted combined with an improved contact algorithm to simulate the dynamic compaction process using MPM. The simulation results agree well with the test data on the construction site of Chengde Airport China. The soil improvement zone of rockfill during dynamic compaction can be divided into a deep improvement zone and a surface improvement zone, where the deep improvement zone is the main improvement zone. The distribution of volumetric strain as well as that of the volume compression plastic strain energy density and the historical maximum mean compressive stress in the deep improvement zone is approximately ellipsoidal, and the trend downward is more pronounced than the trend toward the side.

The influence of soft substratum on the dynamic compaction is also investigated. The presence of SS increases the crater depth, which is mainly due to the settlement of SS rather than the overlying layer. The ellipsoids of volumetric strain, volume compression plastic strain energy density and historical maximum mean compressive stress of the deep improvement zone are cut-off by SS. In the main area affected by dynamic compaction in SS, the distributions of the three variables observed are approximately semi-ellipsoidal. When the dynamic compaction influence radius of the three variables is changing along the depth, there is a sudden increase of the radius in SS. There is a decrease of the volume compression plastic strain energy density and the historical maximum mean compressive stress under the interface of the two zones, which is explained by a simple 1-D case where the stress wave is reflected and refracted on the interface of two linear elastic materials.

Acknowledgments. This study was supported by the National Key Fundamental Research Program of China (No. 2014CB047003).

References

- Bauer, E.: Calibration of a comprehensive hypoplastic model for granular materials. *Soils Found.* **36**(1), 13–26 (1996). <https://doi.org/10.3208/sandf.36.13>
- Brackbill, J.U., Ruppel, H.M.: FLIP: a method for adaptively zoned, particle-in-cell calculations of fluid flows in two dimensions. *J. Comput. Phys.* **65**(2), 314–343 (1986). [https://doi.org/10.1016/0021-9991\(86\)90211-1](https://doi.org/10.1016/0021-9991(86)90211-1)
- Chow, Y., Yong, D., Yong, K., Lee, S.: Dynamic compaction analysis. *J. Geotech. Eng.* **118**(8), 1141–1157 (1992). [https://doi.org/10.1061/\(asce\)0733-9410\(1992\)118:8\(1141\)](https://doi.org/10.1061/(asce)0733-9410(1992)118:8(1141))
- Cundall, P.: Explicit finite difference method in geomechanics. Paper presented at the Second International Conference on Numerical Methods in Geomechanics, Blacksburg (1976)
- Dawson, J.M.: Particle simulation of plasmas. *Rev. Mod. Phys.* **55**(2), 403 (1983). <https://doi.org/10.1103/revmodphys.55.403>
- Ghassemi, A., Pak, A., Shahir, H.: Numerical study of the coupled hydro-mechanical effects in dynamic compaction of saturated granular soils. *Comput. Geotech.* **37**(1–2), 10–24 (2010). <https://doi.org/10.1016/j.compgeo.2009.06.009>
- Gu, Q., Lee, F.-H.: Ground response to dynamic compaction of dry sand. *Géotechnique* **52**(7), 481–493 (2002). <https://doi.org/10.1680/geot.2002.52.7.481>
- Gudehus, G.: A comprehensive constitutive equation for granular materials. *Soils Found.* **36**(1), 1–12 (1996). <https://doi.org/10.3208/sandf.36.1>
- Harlow, F.H., Evans, M.: A machine calculation method for hydrodynamic problems (1955)
- Kafafi, I.K.a.: Formulation of a dynamic material point method (MPM) for geomechanical problems (2013)
- Ma, X., Giguere, P.T., Jayaraman, B., Zhang, D.Z.: Distribution coefficient algorithm for small mass nodes in material point method. *J. Comput. Phys.* **229**(20), 7819–7833 (2010). <https://doi.org/10.1016/j.jcp.2010.06.041>
- Menard, L., Broise, Y.: Theoretical and practical aspects of dynamic consolidation. In: *Ground Treatment by Deep Compaction*, pp. 3–18. Thomas Telford Publishing (1976)
- Nairn, J.: Modeling imperfect interfaces in the material point method using multimaterial methods. *Comput. Model. Eng. Sci.* **1**(1), 1–15 (2013)
- Pan, J., Selby, A.: Simulation of dynamic compaction of loose granular soils. *Adv. Eng. Softw.* **33**(7–10), 631–640 (2002). [https://doi.org/10.1016/S0965-9978\(02\)00067-4](https://doi.org/10.1016/S0965-9978(02)00067-4)
- Poran, C.J., Rodriguez, J.A.: Finite element analysis of impact behavior of sand. *Soils Found.* **32**(4), 68–80 (1992). https://doi.org/10.3208/sandf1972.32.4_68
- Sulsky, D., Chen, Z., Schreyer, H.L.: A particle method for history-dependent materials. *Comput. Methods Appl. Mech. Eng.* **118**(1–2), 179–196 (1994). [https://doi.org/10.1016/0045-7825\(94\)90112-0](https://doi.org/10.1016/0045-7825(94)90112-0)
- Sun, Y., Song, E.: Simulation of large-displacement landslide by material point method. *Chin. J. Geotech. Eng.* **37**(7), 1218–1225 (2015)
- Wang, Z.-Q., Deng, X.-I.: Mechanism of dynamic consolidation and its environmental effect. Paper presented at the First International Conference on Case Histories in Geotechnical Engineering, St. Louis, 6 May 1984
- Yao, Y., Zhang, B.: Reinforcement range of dynamic compaction based on volumetric strain. *Rock Soil Mech.* **37**(9), 2663–2671 (2016)

Zhang, D.Z., Ma, X., Giguere, P.T.: Material point method enhanced by modified gradient of shape function. *J. Comput. Phys.* **230**(16), 6379–6398 (2011). <https://doi.org/10.1016/j.jcp.2011.04.032>

Zhang, R., Sun, Y., Song, E.: Simulation of dynamic compaction using material point method and analysis of its energy conversion law. *Chin. J. Geotech. Eng.* **41**(7) (2019)



Bearing Capacity of Square Footing: A Comparative Study Employing Non-associative MC and MCC Model

Mousumi Mukherjee¹ and Arindam Dey²(✉)

¹ Department of Civil Engineering, IIT Mandi, Mandi, India
mousumi@iitmansi.ac.in

² Department of Civil Engineering, IIT Guwahati, Guwahati, India
arindam.dey@iitg.ac.in

Abstract. The classical bearing capacity theories adopt a plane-strain framework along with an elastic-perfectly plastic Mohr-Coulomb (MC) constitutive response of soil. It is well known that associative MC model fails to capture the evolution of principal stress and suffers from excessive dilation prediction. A non-associative extension of MC model is often employed to control such excessive dilation response; however, their applicability in prediction of 3D bearing capacity of footings should be explored. Further, the critical state based Modified Cam-Clay (MCC) models are expected to delineate a better stress-strain prediction of soil and it will be interesting to examine the 3D bearing capacity estimates of regular shaped foundations employing these two different models. In this regard, this article addresses the finite-element based bearing capacity estimation of a square footing resting on the surface of a semi-infinite homogeneous soil medium. The footing is represented by linear-elastic element, while the foundation soil has been represented by both non-associative MC and MCC models. Comparison of the load-displacement response of the uniformly loaded footing, obtained from considering the MC and MCC models, clearly delineates the shortcoming of the MC and necessity of adopting MCC behaviour in a 3-dimensional geotechnical problem.

Keywords: 3D bearing capacity · Square footing · Mohr-Coulomb model · Modified Cam-Clay model · Dilatancy · Load-deformation

1 Introduction

Bearing capacity estimation is one of the most attempted problem in geotechnical engineering. Followed by the classical studies related to bearing capacity of strip footings resting on semi-infinite elastic medium (Terzaghi 1943; Meyerhof 1951; Vesic 1973), several attempts have been made to address different realistic complexities with the aid of different analyses techniques (Hanna 1982; Meyerhof and Koumoto 1987; Hanna and Rahaman 1990; Reddy et al. 1991; Cerato and Lutenegger 2006; Loukidis and Salgado 2009; Zhao et al. 2014; Yang et al. 2016). It is worth noting that, in practice, the preference of adopting strip footing is largely restricted by the arrangement of foundations for a building structure, and the application of isolated square,

rectangular, or combined footings are more common. Such footings, when loaded, represent 3-dimensional stress distribution, which is expected to generate a characteristic response and failure mechanism that is different from the plane-strain mechanism observed for loaded strip footings. In order to cater the shape effect of footings on the bearing capacity, it is a common practice to utilize suitable shape factors governed by the aspect ratio of the footing. Many researchers have accommodated the shape effect, and its response on the bearing capacity and failure mechanism, through experimental and numerical studies on square footings on cohesionless or cohesive soils (Cerato and Lutenegger 2006; Acharyya and Dey 2018a, b, c; Acharyya et al. 2018a).

Almost all of the earlier studies have made use of the elastic-perfectly plastic Mohr-Coulomb (MC) model for representing the soil behavior. However, being a plane-strain adaptation, MC model cannot properly represent the stress-strain response of an arbitrarily shaped footing resting on semi-infinite medium. Moreover, the MC model fails to address any post-peak strain-softening feature in the load-displacement characteristics of a loaded footing. Therefore, M-C model fails to exhibit the development of intermediate principal stresses that forms the crux of 3-dimensional response of such foundations. This necessitates the application of an advanced generalized 3D-constitutive model that can accommodate both strain hardening and strain softening behaviour of the foundation soil. Application of Modified Cam-Clay (MCC) model, within a numerical framework, can be an effective means of simulating the 3D bearing capacity problems. Application of MCC model for geotechnical problems has already been into practice (Abd and Vermeer 2004; Lim et al. 2010; Wang and Bienen 2016; Oh and Vanapalli 2018; Dey et al. 2018).

Apart from the shear strength parameters (cohesion, c , and angle of internal friction, φ) and stiffness parameters (Modulus of elasticity, E , and Poisson's ratio, ν), the inferences from M-C models are also influenced by the angle of dilation (ψ). The dilatancy parameter primarily governs the volume change characteristics of the soil during shearing. The dilatancy angle varies from zero to the soil friction angle. Correspondingly, the magnitude of dilative coefficient, defined as $\eta = \psi/\varphi$, varies in the range of $0 \leq \eta \leq 1$. Based on the plasticity theory, it is stated that a material follows non-associative flow rule if the dilatancy angle is not similar to the friction angle of the material; whereas, the case $\eta = 1$ indicates that the material follows an associative flow rule (Vermeer and de-Borst 1984; Nova and Montrasio 1991; Drescher and Detournay 1993; Bolton and Lau 1993; Manoharan and Dasgupta 1995; Shiao et al. 2003; Benmabarek et al. 2012). It has been a common practice in most of the geotechnical problems to consider soils to be following associative flow rule, with the exception of few recent researches elucidating the influence of non-associative flow rule on the bearing response of shallow foundations (Acharyya and Dey 2018a, b, c). It was highlighted that dilatancy plays a significant role in altering the bearing response and the failure mechanism beneath a strip footing. Studies pertaining to the influence of dilatancy on the more common footing shapes, such as the square footing, are literally few. Based on a fully associative flow rule, Dey et al. (2018) highlighted that excessive dilation prediction of the associative MC model may have significant impact on the manifestation of the failure mechanism in the bearing capacity of a square footing. Further, it was illustrated by Dey et al. (2018) that excessive dilative MC models fail to

address the volumetric compression of the NC clayey soils. Hence, it becomes important to study further the influence of dilatancy on the bearing capacity of square footing resting on homogeneous ground, and the same is reported in the present article. Therefore, an attempt has been made to study further the influence of dilatancy on the prediction of MC models, and conduct a comparative study of the response of an MCC model to that of a non-dilative or partially-dilative MC model, thereby assessing their comparative efficacies in representing the bearing capacity and failure mechanism.

2 Description of Constitutive Models

The generalized 3D nonlinear elasto-plastic constitutive relation can be represented by the following incremental form

$$d\sigma'_{ij} = C_{ijkl} d\varepsilon_{kl} \quad (1)$$

where σ'_{ij} and ε_{kl} define the effective stress and strain tensor, respectively and the elasto-plastic tangent stiffness tensor C_{ijkl} is given by

$$C_{ijkl} = E_{ijkl} - \frac{E_{ijmn} P_{mn} Q_{rs} E_{rskl}}{H + Q_{ab} E_{abcd} P_{cd}} \quad (2)$$

Where E_{ijkl} is the isotropic elastic stiffness tensor, H is the hardening modulus, P and Q are the directions of outer normal to the plastic potential (g) and yield surface (f), respectively, $P_{ij} = \partial g / \partial \sigma'_{ij}$ and $Q_{ij} = \partial f / \partial \sigma'_{ij}$. Simulations have been carried out employing two different constitutive models, Modified Cam-Clay (MCC) and Mohr-Coulomb (MC). For the present work, non-associative formulation has been considered for MC model with different mathematical expression for the plastic potential and the yield surface ($g \neq f$); whereas, focus has been restricted only to the associative MCC model enforcing same expression for the two surfaces ($g = f$). The MCC model is a critical state concept-based hardening (softening) model with following expression for the yield surface

$$f = \frac{q^2}{M^2} + p'(p' - p'_p) \quad (3)$$

In the above expression, q , p' , M , p'_p are the shear stress, effective mean pressure, shear stress ratio (q/p') at critical state and pre-consolidation pressure. In MCC model, a logarithmic relation is assumed between specific volume (v) and p' in virgin isotropic compression

$$v - v_0 = -\lambda \ln \left(\frac{p'}{p'_0} \right) \quad (4)$$

where, λ is the isotropic compression index. During unloading or reloading, a different logarithmic relation is followed

$$v - v_0 = -\kappa \ln \left(\frac{p'}{p'_0} \right) \quad (5)$$

Where, κ is the isotropic swelling index. The isotropic hardening (softening) relation is defined in terms of evolution of p'_p with plastic volumetric strain (ε_p^p)

$$dp'_p = \frac{vp'_p}{\lambda - \kappa} d\varepsilon_p^p \quad (6)$$

The bulk modulus (K) depends on p' and κ

$$K = \frac{vp'}{\kappa} \quad (7)$$

The yield condition of the elastic-perfectly plastic MC model consists of following six yield functions in terms of principal stresses

$$\begin{aligned} f_{1a} &= \frac{(\sigma'_2 - \sigma'_3)}{2} + \frac{(\sigma'_2 + \sigma'_3) \sin \phi}{2} - c \cos \phi \leq 0 \\ f_{1b} &= \frac{(\sigma'_3 - \sigma'_2)}{2} + \frac{(\sigma'_3 + \sigma'_2) \sin \phi}{2} - c \cos \phi \leq 0 \\ f_{2a} &= \frac{(\sigma'_3 - \sigma'_1)}{2} + \frac{(\sigma'_3 + \sigma'_1) \sin \phi}{2} - c \cos \phi \leq 0 \\ f_{2b} &= \frac{(\sigma'_1 - \sigma'_3)}{2} + \frac{(\sigma'_1 + \sigma'_3) \sin \phi}{2} - c \cos \phi \leq 0 \\ f_{3a} &= \frac{(\sigma'_1 - \sigma'_2)}{2} + \frac{(\sigma'_1 + \sigma'_2) \sin \phi}{2} - c \cos \phi \leq 0 \\ f_{3b} &= \frac{(\sigma'_2 - \sigma'_1)}{2} + \frac{(\sigma'_2 + \sigma'_1) \sin \phi}{2} - c \cos \phi \leq 0 \end{aligned} \quad (8)$$

In addition to the yield functions, six plastic potential functions for the MC model are defined below

$$\begin{aligned}
g_{1a} &= \frac{(\sigma'_2 - \sigma'_3)}{2} + \frac{(\sigma'_2 + \sigma'_3) \sin \psi}{2} \\
g_{1b} &= \frac{(\sigma'_3 - \sigma'_2)}{2} + \frac{(\sigma'_3 + \sigma'_2) \sin \psi}{2} \\
g_{2a} &= \frac{(\sigma'_3 - \sigma'_1)}{2} + \frac{(\sigma'_3 + \sigma'_1) \sin \psi}{2} \\
g_{2b} &= \frac{(\sigma'_1 - \sigma'_3)}{2} + \frac{(\sigma'_1 + \sigma'_3) \sin \psi}{2} \\
g_{3a} &= \frac{(\sigma'_1 - \sigma'_2)}{2} + \frac{(\sigma'_1 + \sigma'_2) \sin \psi}{2} \\
g_{3b} &= \frac{(\sigma'_2 - \sigma'_1)}{2} + \frac{(\sigma'_2 + \sigma'_1) \sin \psi}{2}
\end{aligned} \tag{9}$$

In the above equations, c , ϕ , ψ are the cohesion, friction and dilatancy angle, respectively. In case of soil behaviour prediction through MC model, the elastic response is assumed linear with constant elastic parameter values. The constitutive model parameters for MC and MCC model and their values used for FEM simulation have been listed in Table 1.

Table 1. MCC and MC model parameter values considered for FEM simulation

Model	Parameter	Values
MCC	λ	0.077
	κ	0.006
	M	1.2
	p'_p	200 kPa
	v	0.3
MC	c	0
	ϕ	30°
	ψ	0°, 15°, 30°
	v	0.3
	E	20 MPa

Figure 1 presents the stress-strain and volumetric predictions of single element triaxial test for both the models at 200 kPa confining pressure with the parameter sets given in Table 1. It can be observed from Fig. 1(a) that the predicted maximum shear stress from two models nearly becomes same (400 kPa) at an axial strain, i.e., at 2.1%. Interestingly, no change has been noticed in the shear stress response predicted from MC model due to change in the dilation properties. The MCC model aptly captures the compressive volumetric response of the normally consolidated soil at 200 kPa confining pressure (Fig. 1(b)); whereas, a dilative response has been predicted by the associative MC model. The excessive dilation prediction of the associative MC model may have significant impact on the manifestation of the failure mechanism in the

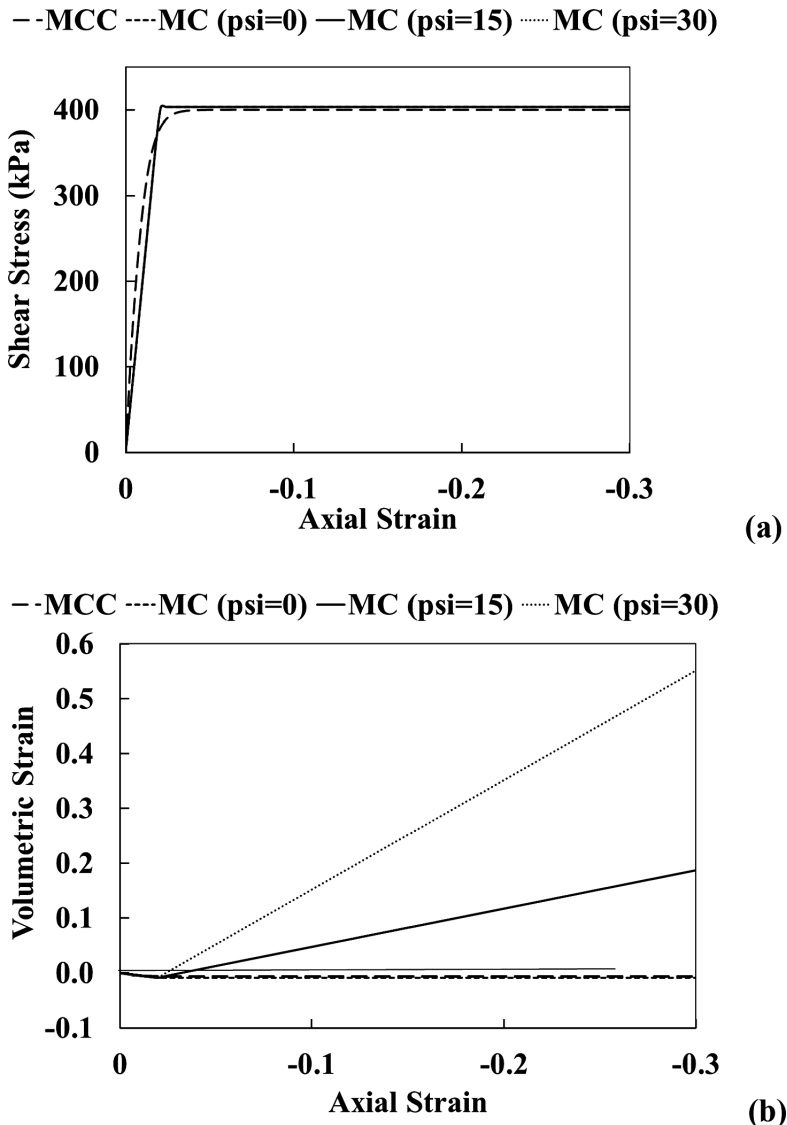


Fig. 1. Triaxial test predictions for MCC and MC model at 200 kPa confining pressure with the parameter set given in Table 1 (a) stress-strain behavior (b) volumetric strain-axial strain behavior

bearing capacity simulation (Dey et al. 2018). Such excessive dilation of MC model can be handled by incorporation of non-associative flow rule, i.e. by introducing the dilation angle in the formulation. Figure 1(b) illustrates the influence of the dilation angle on the volumetric behaviour as predicted by non-associative MC model. A gradual change from dilative to contractive volumetric response can be observed as

the dilation angle has been changed from 30^0 to 0^0 and it becomes very similar to the associative MCC model for the case with dilation angle of 0^0 . It is to be noted that the volumetric strain in MCC model nearly becomes constant when the maximum shear stress has been achieved, which denotes the critical state and marks the failure of the material.

3 Finite Element Modeling

In the present study, the bearing capacity of a square footing, resting on normally consolidated clayey foundation soil, has been assessed with the aid of three-dimensional finite element simulation using PLAXIS 3D AE.01. This software package is sufficed by several features to deal with complex geotechnical problems related to deformation, stability and flow through geotechnical media. Additionally, the availability of a large number of varying constitutive models for representing the stress-strain-time behaviour of soil makes it a very useful investigative tool to study the response of geotechnical entities (PLAXIS Material model manual 2015).

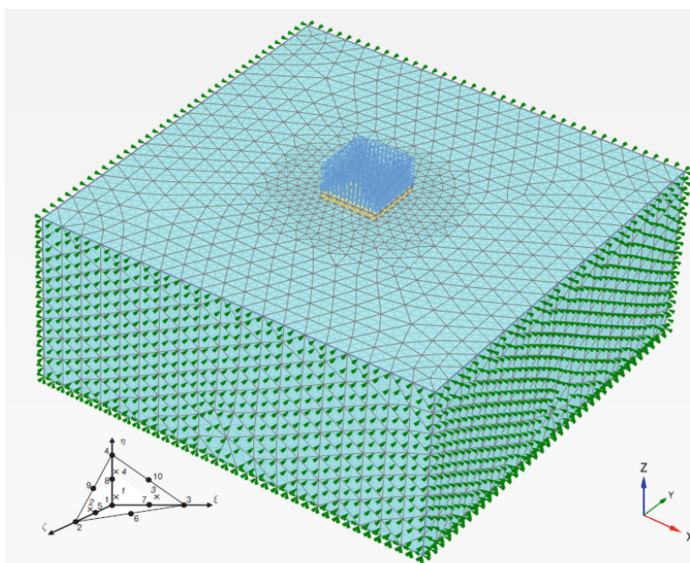


Fig. 2. Typical meshing, standard fixities and basic element used in the FE model

Figure 2 depicts the typical FE model used for the present study. Following the procedure described in Acharyya et al. (2018a), the size of the model domain (14 m in length and breadth with a height of 6 m) has been so decided that the existing lateral boundaries do not influence the stress or strains generated beneath the loaded footing. Standard fixity has been applied to the FE model such that the lateral boundaries are

allowed only vertical deformation, while the bottom boundary is considered non-yielding. The model geometry has been discretised with the aid of 10-noded tetrahedral elements providing a second-order interpolation of displacements, accompanied by a 4-point Gaussian integration scheme. Various types of meshing schemes can be adopted in PLAXIS, governed by the ‘mesh coarseness factor’. For the present case, mesh convergence study had been carried out (Acharyya et al. 2018a) and, accordingly, an optimal fine mesh has been chosen, associative with local refinements adjacent to the footing. Further details of the FE analysis can be found in PLAXIS 3D Reference Manual (2015).

The rigid square footing of width 2 m, made of M20 concrete, is represented by Linear Elastic (LE) element (unit weight $\gamma = 25 \text{ kN/m}^3$, elastic modulus $E = 22 \text{ GPa}$, Poisson’s ratio $\nu = 0.15$) comprising 10-noded tetrahedral elements, and accompanied by an interface element (at the boundary of soil and concrete material) ensuring no-slipage condition. In order to comprehend the influence of constitutive behaviour of soil on the bearing characteristics of a square footing, the soil is represented by two types of constitutive behaviour, namely Mohr-Coulomb (M-C) and Modified Cam Clay (MCC) models.

4 Results and Discussions

The load bearing response of the footing resting on the NC clayey medium has been assessed through load-settlement plots, along with the displacement and stress distributions within the foundation. Figure 3 shows the load-settlement response obtained at the mid-point of the footing. It can be observed that load-settlement response obtained from MC and MCC models are noticeably different. While the MC soil exhibited a nearly elastic-perfectly plastic behaviour as expected, the MCC model illustrated a non-linear elasto-plastic behaviour. It is worth mentioning that the model parameters were so chosen that both the MC and MCC models exhibited elastic-perfectly plastic behaviour (as shown in Fig. 1a). However, the overall representation of the load-deformation response of the MCC model does not follow the single element test, while the overall behaviour from the MC model nearly represents the behaviour from the single element test. This difference is observed because, as mentioned earlier, MC model represents a plane-strain behaviour that is nearly replicated in its overall behaviour as well. However, the MCC model, which can account for 3D volumetric compression, exhibited the overall effect that is different from that of the single element test. Hence, it can be stated that the MCC model is more suitable to represent the 3D response of the square footing on NC soil. Further, the influence of flow rule can be seen on the bearing capacity estimates. The ultimate bearing capacity obtained considering the non-associative flow rule ($\psi = 0$) is obtained to be lesser than that obtained for the associative flow rules (for both partially dilative and fully dilative soils, $\psi = \varphi/2$ and $\psi = \varphi$). The bearing capacity for the former case is obtained to be approximately 370 kPa, while, for the latter, the same is obtained as 420 kPa. The bearing capacity obtained from the MCC model (obtained by double-tangent method) is obtained approximately 460 kPa. Hence, although the bearing capacity estimates are quite comparable to each other, the difference in the MCC and MC estimates are again

attributed to the efficacy of the MCC model in properly capturing the 3D response of the foundation. It can be observed that at an allowable settlement of the 10% of the footing width (settlement = 0.2 m, where width of footing is 2 m), the allowable bearing capacity estimates are also comparable to each other, although the allowable bearing capacity obtained from the MCC model is lesser than that obtained from MC models.

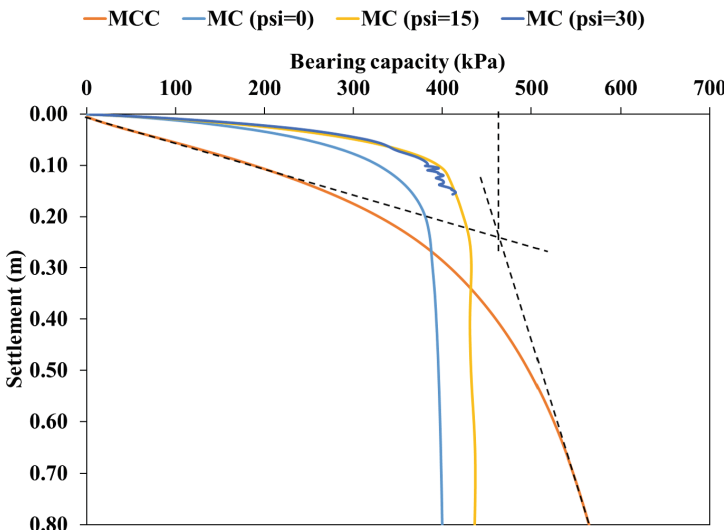


Fig. 3. Load-settlement response obtained from MC and MCC models

Figure 4 shows the typical failure deformations of the footing resting on MC soil. It can be observed that the deformation pattern beneath the footing closely follows a general shear failure, wherein the soil elements beneath the footing is pushed downwards, which induces an outward and upward radial shear in the adjacent soil elements towards the edge of the footing. This behavioural response is similar to the formation of the slip lines beneath a loaded footing. In comparison, the deformation beneath the section of the footing resting on MCC soil (Fig. 5) represents a dominant downward compressive deformation beneath the footing. This observation is in line with the volumetric compression behaviour of the MCC soil represented in Fig. 1b. Further, Fig. 4b and c, respectively highlights, the influence of dilation angles on the typical failure deformation beneath the footing. In case of MC soil with non-associative flow rule, i.e. $\psi = 0$ (Fig. 4a), it can be seen that dominant deformation is vertically downwards towards the foundation soil, exhibiting lesser dilation or heaving at the surface adjacent to the footing. On the contrary, for the case of MC soil with associative flow rule, i.e. $\psi = \varphi$, the dominant deformation comprises of radial outward and upward deformation towards the surface adjacent to the footing, thereby exhibiting prominent heaving at the surface. This is a typical exhibition of dilative behaviour, which is also represented in the volumetric strain behaviour in Fig. 1b.

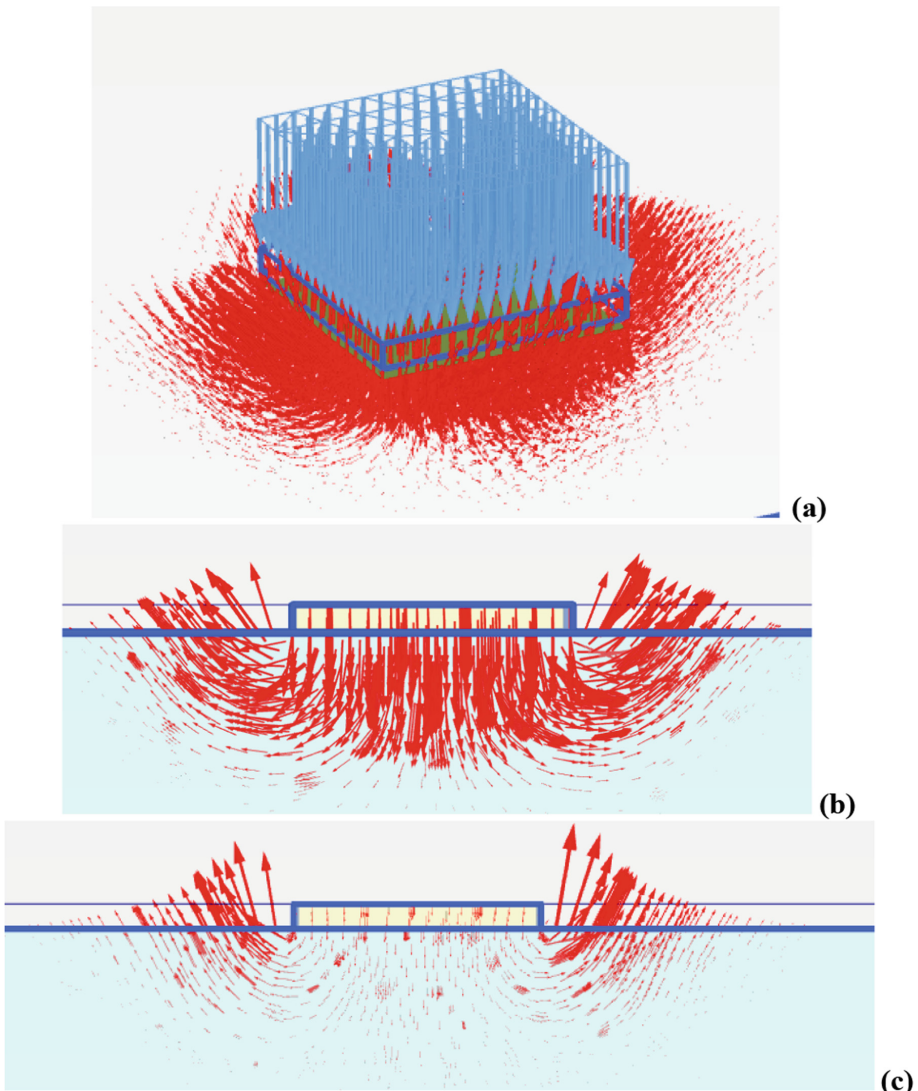


Fig. 4. Failure deformation pattern considering MC model for soil (a) 3D deformation beneath the footing (b) Deformation beneath a section passing through the center of the footing for $\psi = 0$ and (c) for $\psi = \phi$

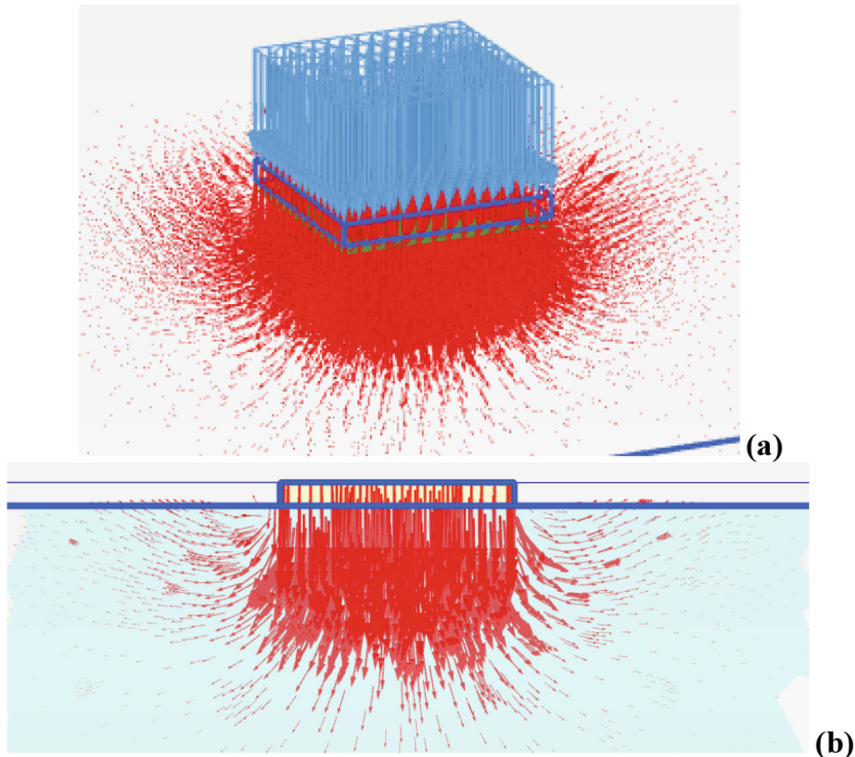


Fig. 5. Failure deformation pattern considering MCC model for soil (a) 3D deformation beneath the footing (b) Deformation beneath a section passing through the center of the footing

Figure 6 illustrates the typical deformation isosurfaces developed in the MC and MCC soils at failure. The isosurfaces typically represent the zone of influence of the foundation soil, which provides resistance against the deformation of the loaded footing. It can be clearly observed that the deformation pattern for the footing on MC soil is mostly confined to the edges of the footing, while, in the MCC soil, it is distributed to the entire foundation soil beneath the footing, represented by hemispherical domes. This observed difference in the influence zone of soil is primarily attributed to the characteristic difference in the material model used to represent the foundation soil. MC soil model represents a plane-strain condition, thus unable to capture properly the overall volumetric compression beneath the footing, and exhibits outward radial heaving at the surface adjacent to the footing. The dominance of upward heaving is visualized for the full dilative MC soil following associative flow rule. On the other hand, MCC soil model is effective in delineating the three-dimensional response of such regular shaped foundations, and thereby effectively captures the volumetric compression behaviour of the NC soil.

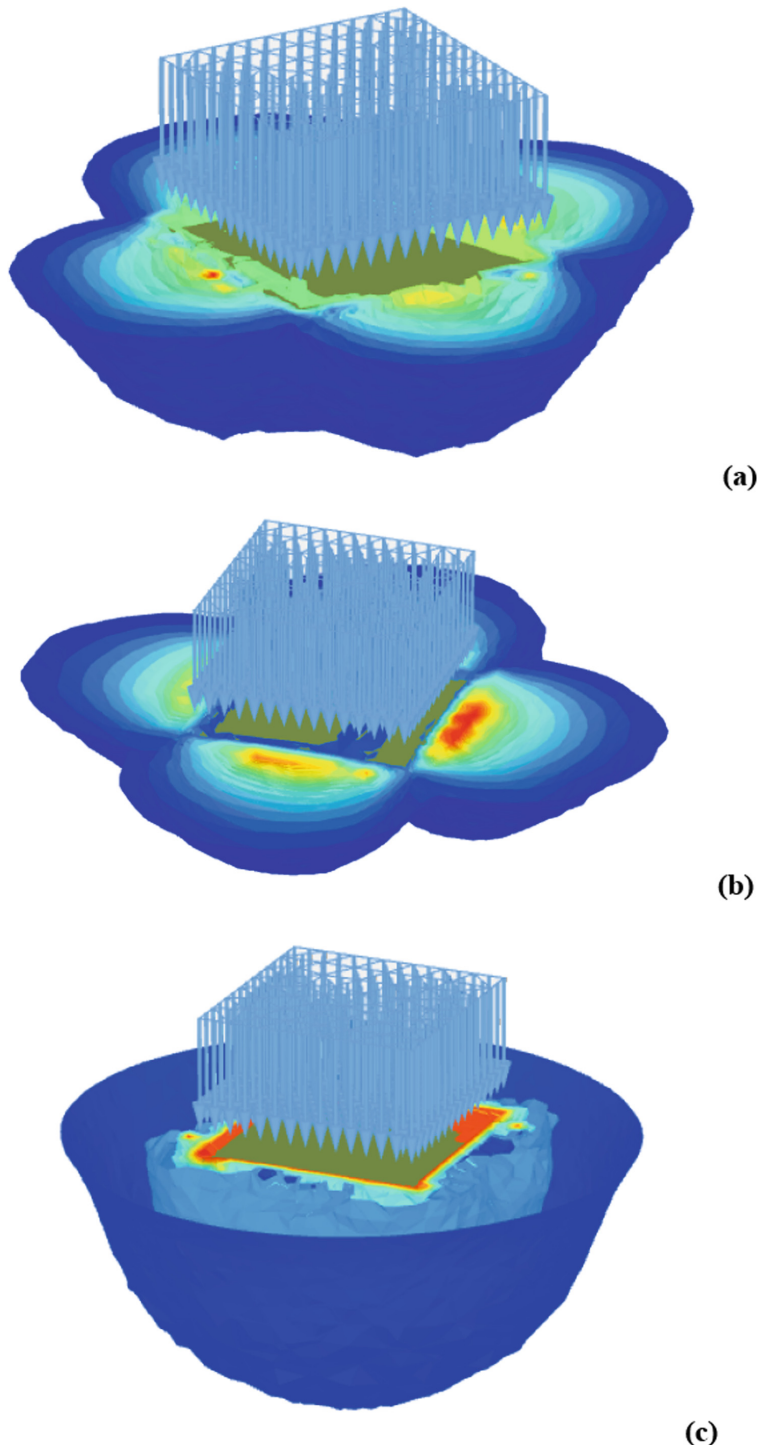


Fig. 6. Deformation isosurfaces developed during footing failure (a) MC soil model with $\psi = 0$
(b) MC soil model with $\psi = 0.10$ (c) MCC soil model

5 Conclusions

This article presents the influence of two different constitutive models, Mohr-Coulomb and Modified Cam-Clay, on the assessment of bearing capacity of a square footing resting on the surface of a normally consolidated soil medium. For the MC model, the influence of soil dilatancy is also presented considering non-associative, partially associative and fully associative flow rules. The load-deformation behaviour, failure deformation patterns and deformation isosurfaces clearly indicate markedly different failure mechanisms of the MC and MCC soils, which, in turn, notably affects the bearing capacity of the square footing. It is observed that even through the stress-strain behaviour of the MC and MCC models obtained from the single element test can be similar through appropriate choice of parameters, yet the overall load-deformation response can be vividly different. Though the MC model exhibited an overall elastic-perfectly plastic behaviour, the MCC model, however, represented an overall nonlinear elasto-plastic behaviour. It is concluded that the excessive dilative behaviour of the MC model fails to represent the volumetric compression of the NC clayey soil, which is justifiably represented by the MCC model. Such findings call for the adoption of MCC model for finding the response of NC clayey soil and the supported structures.

Acknowledgments. The authors would like to thank Dr. Rana Acharyya, Post-Doctoral Researcher, IIT Bombay for his help in creating the PLAXIS 3D models.

References

- Abed, A.A., Vermeer, P.A.: Numerical simulation of unsaturated soil behavior. In: Proceedings of the 1st Euro Mediterranean Conference on Advances in Geomaterials and Structures, Tunisia, pp. 1–8 (2004)
- Acharyya, R., Dey, A.: Evaluation of slip mechanism beneath the shallow footing resting on plane ground by altering flow-rules. In: National Seminar on Advanced Construction and Computational Tools in Geotechniques – Practice to Theory, Indian Geotechnical Society, Kolkata, West Bengal, India, pp. 1–8 (2018)
- Acharyya, R., Dey, A.: Importance of dilatancy on the evolution of failure mechanism of a strip footing resting on horizontal ground. INAE Lett. **3**(3), 131–142 (2018a)
- Acharyya, R., Dey, A.: Assessment of failure mechanism of a strip footing on horizontal ground considering flow rules. Innov. Infrastruct. Solut. **3**(49), 1–16 (2018b)
- Acharyya, R., Dey, A. Kumar, B.: Finite element and ANN-based prediction of bearing capacity of square footing resting on the crest of c- ϕ soil slope. Int. J. Geotech. Eng. (2018). <https://doi.org/10.1080/19386362.2018.1435022>
- Benmabrek, S., Remadna, M.S., Benmabrek, N., Belounar, L.: Numerical evaluation of the bearing capacity factor N'_γ of ring footings. Comput. Geotechn. **44**, 132–138 (2012)
- Bolton, M.D., Lau, C.K.: Vertical bearing capacity factors for circular and strip footings on Mohr-Coulomb soil. Can. Geotech. J. **30**, 1024–1033 (1993)
- Cerato, A.B., Lutenegger, A.J.: Bearing capacity of square and circular footings on a finite layer of granular soil underlain by a rigid base. J. Geotech. Geoenviron. Eng. **132**(11), 1496–1501 (2006)

- Dey, A., Mukherjee, M., Acharyya, R.: Importance of constitutive model in assessing 3-D bearing capacity of square footing on clayey soil using finite element analysis. In: 11th Structural Engineering Convention, Kolkata, India, pp. 1–6 (2018)
- Drescher, A., Detournay, E.: Limit load in translational failure mechanisms for associative and non-associative materials. *Geotechnique* **43**(3), 443–456 (1993)
- Hanna, A., Rahman, A.M.E.: Ultimate bearing capacity of triangular shell strip footings on sand. *J. Geotech. Geoenviron. Eng.* **116**(12), 1851–1863 (1990)
- Hanna, A.M.: Bearing capacity of foundations on a weak sand layer overlaying a strong deposit. *Can. Geotech. J.* **19**(3), 392–396 (1982)
- Lim, A., Ou, C.-Y., Hsieh, P.G.: Evaluation of clay constitutive models for analysis of deep excavation under undrained conditions. *J. GeoEng.* **5**, 9–20 (2010)
- Loukidis, D., Salgado, R.: Bearing capacity of strip and circular footings in sand using finite elements. *Comput. Geotech.* **36**, 871–879 (2009)
- Manoharan, N., Dasgupta, S.P.: Bearing capacity of surface footings by finite elements. *Comput. Geotech.* **54**(4), 563–586 (1995)
- Meyerhof, G.G.: The ultimate bearing capacity of foundations. *Geotechnique* **2**, 301–332 (1951)
- Meyerhof, G.G., Koumoto, T.: Inclination factors for bearing capacity of shallow footings. *J. Geotech. Geoenviron. Eng.* **113**(9), 1013–1018 (1987)
- Nova, R., Montrasio, L.: Settlements of shallow foundations on sand. *Geotechnique* **41**(2), 243–256 (1991)
- Oh, W.T., Vanapalli, S.K.: Modeling the stress versus settlement behaviour of shallow foundations in unsaturated cohesive soils extending the modified total stress approach. *Soils Found.* **58**, 382–397 (2018)
- Reddy, A.S., Singh, A.K., Karnik, S.S.: Bearing capacity of clays whose cohesion increases linearly with depth. *J. Geotech. Geoenviron. Eng.* **117**(2), 348–353 (1991)
- Shiau, J.S., Lyamin, A.V., Sloan, S.W.: Bearing capacity of a sand layer on clay by finite element limit analysis. *Can. Geotech. J.* **40**, 900–915 (2003)
- Terzaghi, K.: Theoretical Soil Mechanics. Wiley, New York (1943)
- Vermeer, P.A., de Borst, R.: Non-associative plasticity for soils, concrete and rock. *Heron* **29**(3), 1–64 (1984)
- Vesic, A.S.: Analysis of ultimate loads of shallow foundation. *J. Soil Mech. Found. Div.* **99** (SM1), 45–73 (1973)
- Wang, D., Bienen, B.: Numerical investigation of penetration of a large-diameter footing into normally consolidated Kaolin clay with a consolidation phase. *Geotechnique* **66**, 947–952 (2016)
- Yang, F., Zheng, X.C., Zhao, L.H., Tan, Y.G.: Ultimate bearing capacity of a strip footing placed on sand with a rigid basement. *Comput. Geotech.* **77**, 115–119 (2016)
- Zhao, L., Yang, F., Dan, H.: The influence of horizontal confinement on the bearing capacity factor N_y of smooth strip footing. *Comput. Geotech.* **61**, 127–131 (2014)



A Micro-mechanical Study for Constant Shear Drained Behaviour of Granular Material

Hoang Bao Khoi Nguyen¹, Mizanur Rahman^{2(✉)},
and Hung-Chun Wang¹

¹ School of Natural and Built Environments, University of South Australia,
Adelaide, Australia
Khoi.Nguyen@unisa.edu.au,
wanhy118@mymail.unisa.edu.au

² Water and Natural Resources Natural and Built Environments Research Centre
(NBERC) and Geotechnical Engineering, School of Natural
and Built Environments, University of South Australia, Adelaide, Australia
Mizanur.Rahman@unisa.edu.au

Abstract. Soil liquefaction has been often reported in undrained condition (lack of drainage), in which pore water pressure is continuously generated until flow deformation. However, it has been also found that the flow deformation may happen in drained condition due to lateral stress relief. Such phenomenon, also known as constant shear drained (CSD) response, is not uncommon, but the knowledge about CSD condition is still not fully understand. A discrete element method (DEM) is used to investigate the CSD condition by performing stress-controlled simulations on 3D specimens of ellipsoid particles. After consolidation, the specimens were sheared in drained condition. Then, shear stresses (τ) were kept constant and the normal effective stresses (σ'_N) reduced until failure. It was found that the specimens started to fail when the effective stress paths approached the critical state line. At the point of failure, the axial and volumetric strains have abrupt changes. The study will also provide more in-sights in the micro-mechanical quantities such as soil fabric, which was believed to control the overall observed behavior of soils.

1 Introduction

The critical state soil mechanics (CSSM) framework for granular materials has been well established in the laboratory experiments, most of which are undrained and drained compression tests. Such testing is performed by controlling the principle stress and strain components in 3 orthogonal directions; where σ'_{11} and ε_{11} are the major principle effective stress and strain, respectively; σ'_{33} (equal to σ'_{22}) and ε_{33} (i.e. equal to ε_{22}) are the minor principle effective stress and strain, respectively. In undrained condition, three types of behavior are observed: non-flow, limited flow and flow (shown in Fig. 1). Non-flow behavior associates with strain hardening (i.e. deviatoric stress, q increases) throughout the shearing process, while limited flow and flow behavior associates with strain soften after initial peak q ; where $q = (\sigma'_{11} - \sigma'_{33})$. On the other hands, the observed response to drained shearing has been commonly

classified into two categories, which are contractive and dilative as shown in Fig. 1. Dilative behavior in drained shearing associates with the volumetric dilation, while contractive behavior associates with volumetric contraction; where volume in triaxial condition is often measured as volumetric strain (ε_v). It should be noted that the observed behavior (drained or undrained) of a soil highly depends on its initial state (i.e. initial void ratio, e_0 and initial mean normal effective stress, p'_0); where $p' = (\sigma'_{11} + 2\sigma'_{33})/3$.

With increasing deviatoric strain i.e. $\varepsilon_q = 2/3(\varepsilon_{11} - \varepsilon_{33})$, the soil will eventually reach an equilibrium state, at which there is no increment in stress (q or mean effective stress, p'), pore water pressure (Δu) and volume i.e. $dq = 0$, $dp' = 0$, $d\Delta u = 0$ and $d\varepsilon_v = 0$, regardless of its initial state. Such equilibrium state is referred to as the critical state (CS) in the triaxial condition, which has been extensively investigated in the classical CSSM framework (Been et al. 1991; Mizanur and Lo 2012; Rahman and Lo 2014; Wei and Yang 2018; Zhang et al. 2018). It has been also reported that CS is unique for soil. However, achieving a clear CS under laboratory conditions is often not easy, particularly for F and NF. Some of these may be overcome by extrapolation (Carrera et al. 2011; Murthy et al. 2007; Rahman and Lo 2014) and an acceptable critical state line (CSL) in the classical e -log(p') space, with a tolerable scatter can be achieved.

Both flow and limited flow are often known as static liquefaction and are triggered at a stress ratio, $\eta_{IS}(q/p')$, which occurs at peak q . Its occurrence in the field often leads to devastating effects, such as quick flow slides (Fourie et al. 2001; Lade and Yamamuro 2011; Olson et al. 2000). There have been some methods to characterize the liquefaction triggering point in order to predict the liquefaction potential of a soil (Mizanur and Lo 2012; Rabbi et al. 2018). However, it has been also found that the flow deformation may happen in drained condition due to lateral stress relief. Such phenomenon, also known as constant shear drained (CSD) response, is not uncommon. The knowledge about CSD condition under CSSM framework has been investigated in the experimental studies (Lashkari et al. 2019; Rabbi et al. 2019). However, the true mechanics of such a phenomenon is not yet to be fully understood.

Alternatively, the discrete element method (DEM) has been widely used to study the micro-mechanical behavior of granular material and develop the link between micro- and macro-mechanics. Such a technique was adopted to investigate the CSD condition by performing stress-controlled simulations on 3D specimens of ellipsoid particles. The study will also provide more in-sights in the micro-mechanical quantities such as soil fabric, which was believed to control the overall observed behavior of soils.

2 Methodology

An open source DEM software called OVAL, developed by Kuhn (2006), was adopted for the investigation in this study. The DEM, proposed by Cundall and Strack (1979), applies two laws of physics for particle interactions: the Newton's second law to provide particle movement and the force-displacement law to determine the contact forces between the particles. Both linear and non-linear (Hertzian rule) contact models have been widely used in the literature. However, a linear contact model and periodic boundary were used in this study, wherein particles are able to overlap one another at their contacts, by a small amount compared to their size, which is treated as the

deformation of the particles. All these particles were assigned a normal contact stiffness of 10^8 N/m, a ratio of tangential to normal contact stiffness of 1.0, a coefficient of friction at particle contacts of 0.50 and the coefficient of (rotational and translational) body damping of 0.05.

Note, the time step of 1 was considered in this study, which is not the really clock time. The purpose of using such a time step is to reduce the computational demand. Consequently, the particle density was scaled up to 9.766×10^8 (kg/m³), which is approximately 3.69×10^5 times larger than 2650 kg/m³ for real geo-material as reported in Perez et al. (2016). Such a method is common to optimize the simulation time in DEM literature (Ng 2006; Thornton 2000). The strain rate of 0.00001% per time step was found as suitable for all DEM simulations (Nguyen and Rahman 2017; Nguyen et al. 2015).

Specimen of approximately 5000 ellipsoid particles, as shown in Fig. 1, was considered in this study. As the purpose of this study is to investigate the constant shear behavior, the existing CSL for the same specimens was adopted from the previous study (Nguyen et al. 2017; Nguyen et al. 2018). The specimens were isotropically consolidated to desired mean effective stress (p'). After consolidation, the specimens were sheared in drained condition. Then, deviatoric stresses (q) were kept constant and the p' reduced until failure.

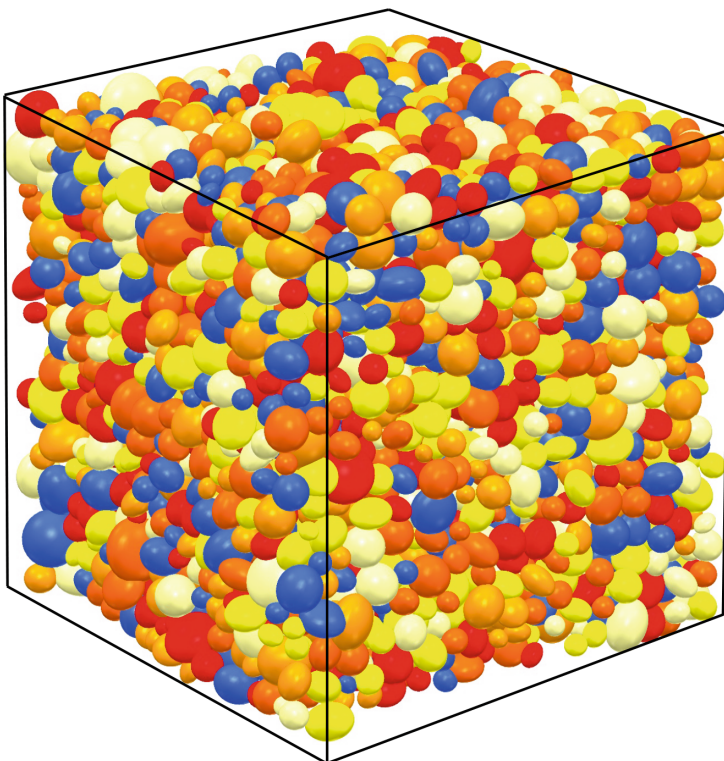


Fig. 1. Specimen of approximately 5000 particles for constant shear drained simulations

3 Constant Shear Drained Behavior

Figure 2 showed the constant shear response of granular material in DEM. All simulations (CSD-ISO12-01, CSD-ISO12-02 and CSD-ISO12-03) had similar initial states i.e. e_0 and p'_0 . It was found that the specimens started to fail when the effective stress paths reached the critical state line (CSL), which was achieved by conventional drained and undrained triaxial simulations (Nguyen et al. 2017; Nguyen et al. 2018). It can be seen that the simulations showed instability (q slightly reduces) after reaching CSL.

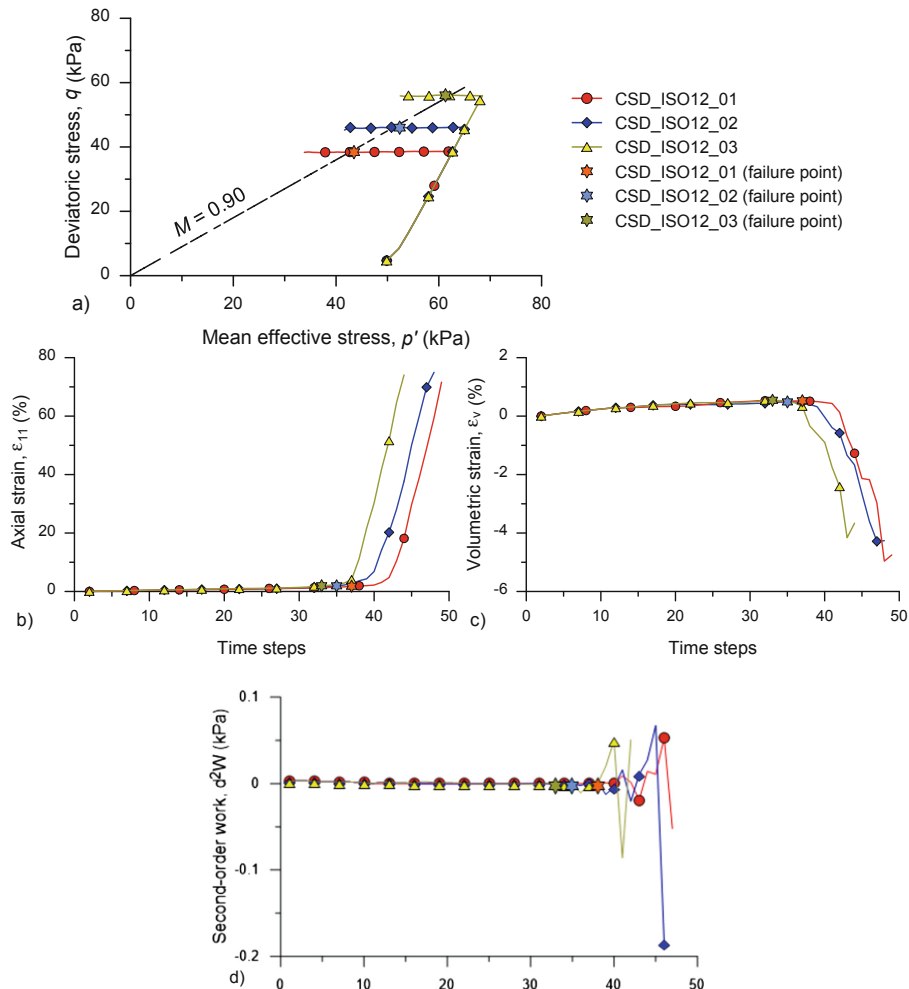


Fig. 2. Behaviour of granular material under constant shear condition in (a) $q - p'$, (b) ε_{11} -time, (c) ε_v -time and (d) d^2W -time spaces.

At the point of failure, the axial and volumetric strains have abrupt changes in Figs. 2b and c. Note, there have been different method to identify instability of soil. Abrupt change in axial or volumetric strain during shearing is one of the common methods. Note, after the abrupt change of axial strain, the simulations terminated as there was numerical instability happening.

In addition, the second-order work (d^2W) (Drucker 1957; Hill 1958) has been commonly adopted to identify the liquefaction triggering or instability behavior in the triaxial condition (Mizanur and Lo 2012; Rabbi et al. 2018). In triaxial condition, it has been reported that a significant change of d^2W happens at onset of instability (Chu et al. 2015; Rabbi et al. 2019); where $d^2W = d\sigma d\epsilon$; σ and ϵ indicate the stress and strain tensor respectively; the notation ‘d’ indicates the rate of change. The d^2W evolution paths were shown in Fig. 2d. d^2W also started decreasing less than zero after the failure point.

4 Micro-mechanical Quantity During Constant Shear

In addition, the micro-mechanical quantity, von Mises fabric (F_{vM}), was also analyzed during constant shear simulations. Note, the structural anisotropy can be determined by the fabric tensor (\mathbf{F}), which was firstly introduced in Satake (1982) and expressed as the following equation:

$$\mathbf{F} = F_{ij} = \frac{1}{N} \sum_{k=1}^N \mathbf{n}_i^k \mathbf{n}_j^k = \begin{bmatrix} F_{11} & F_{12} & F_{13} \\ F_{21} & F_{22} & F_{23} \\ F_{31} & F_{32} & F_{33} \end{bmatrix} \quad (1)$$

where n^k is the direction (unit vector) of the k^{th} contact and N is the number of contacts in the specimen. The bold character (e.g. \mathbf{F}) indicates the tensor whereas the italic character (e.g. F_{ij}) indicates the scalar value of the tensor. F_{11} , F_{22} and F_{33} are the fabric in the principal directions ($i = j$), and F_{12} , F_{13} , F_{21} , F_{23} , F_{31} and F_{32} are the fabric in the shear directions ($i \neq j$). The scalar values of shear components in opposite direction are equal i.e. $F_{12} = F_{21}$, $F_{13} = F_{31}$ and $F_{23} = F_{32}$. The fabric tensor can be formulated based on the theory of Cauchy stress tensor (σ), and second invariant (J_2) of the fabric tensor can be defined as:

$$J_2 = \frac{1}{2} \text{tr}(\mathbf{s}\mathbf{F}^2) = \frac{1}{6} \left[(F_{11} - F_{22})^2 + (F_{11} - F_{33})^2 + (F_{22} - F_{33})^2 \right] + F_{12}^2 + F_{13}^2 + F_{23}^2 \quad (2)$$

Based on von Mises stress yield criterion, a similar scalar quantity of equivalent deviatoric fabric i.e. von Mises fabric (F_{vM}) can be defined as:

$$F_{vM} = \sqrt{3J_2} \quad (3)$$

Figure 3 showed the evolution paths of F_{vM} during constant shear drained condition. It can be noted that F_{vM} reached the CS zone at its failure point. The CS zone for such a specimen can be found in Nguyen et al. (2018). After the failure points, it seemed like that numerical instability happened i.e. the high fluctuation in F_{vM} .

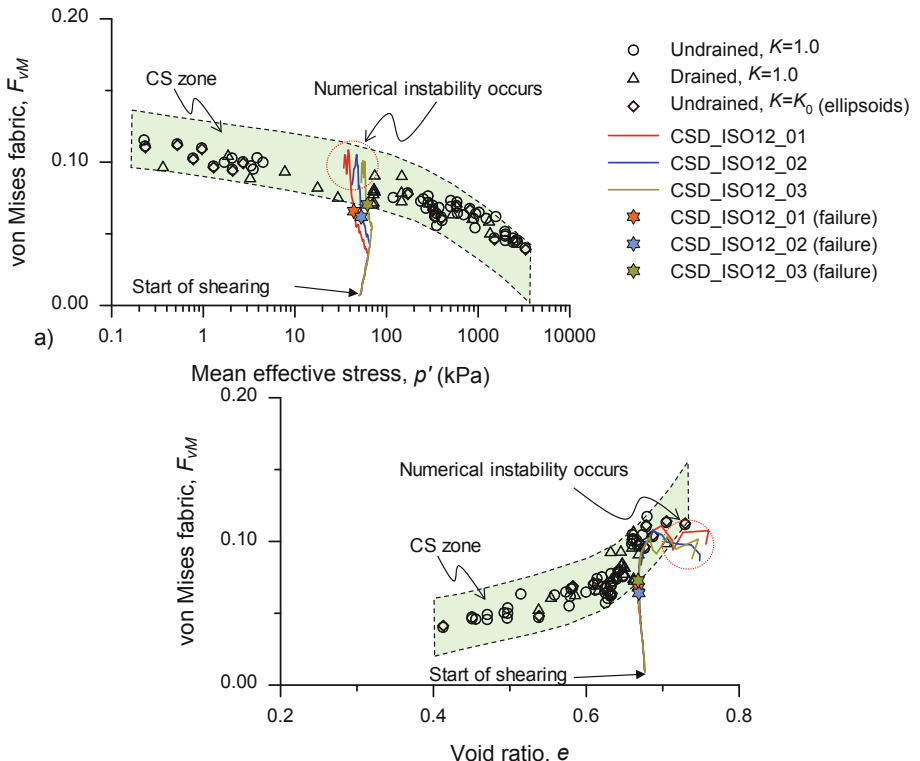


Fig. 3. The fabric evolution paths during constant shear drained condition in (a) $F_{vM} - p'$ and (b) $F_{vM} - e$ spaces.

5 Conclusions

This study adopted DEM to investigate the constant shear drained behavior of granular materials under the critical state soil mechanics (CSSM) framework. It was found that after reaching CSL, abrupt change in axial and volumetric strains happened and the simulations exhibited instability. The micro-mechanical parameter such as deviatoric fabric (F_{vM}) also confirmed the instability behavior of those simulations.

References

- Been, K., Jefferies, M., Hachey, J.: The critical state of sands. *Geotechnique* **41**(3), 365–381 (1991)
- Carrera, A., Coop, M., Lancellotta, R.: Influence of grading on the mechanical behaviour of stava tailings. *Geotechnique* **61**(11), 935–946 (2011)
- Chu, J., Wanatowski, D., Leong, W.K., Loke, W.L., He, J.: Instability of dilative sand. *Geotech. Res.* **2**(1), 35–48 (2015)
- Cundall, P.A., Strack, O.D.: A discrete numerical model for granular assemblies. *Geotechnique* **29**(1), 47–65 (1979)
- Drucker, D.C.: A definition of stable inelastic material. Brown Univ Providence RI (1957)
- Fourie, A., Blight, G., Papageorgiou, G.: Static liquefaction as a possible explanation for the Merriespruit tailings dam failure. *Can. Geotech. J.* **38**(4), 707–719 (2001)
- Hill, R.: A general theory of uniqueness and stability in elastic-plastic solids. *J. Mech. Phys. Solids* **6**(3), 236–249 (1958)
- Kuhn, M.R.: OVAL and OVALPLOT: Programs for analyzing dense particle assemblies with the discrete element method, 98p (2006)
- Lade, P.V., Yamamuro, J.A.: Evaluation of static liquefaction potential of silty sand slopes. *Can. Geotech. J.* **48**(2), 247–264 (2011)
- Lashkari, A., Khodadadi, M., Binesh, S.M., Rahman, M.M.: Instability of particulate assemblies under constant shear drained stress path: DEM approach. *Int. J. Geomech.* **19**(6), 04019049 (2019)
- Mizanur, R.M., Lo, S.: Predicting the onset of static liquefaction of loose sand with fines. *J. Geotech. Geoenvir. Eng.* **138**(8), 1037–1041 (2012)
- Murthy, T.G., Loukidis, D., Carraro, J.A.H., Prezzi, M., Salgado, R.: Undrained monotonic response of clean and silty sands. *Geotechnique* **57**(3), 273–288 (2007)
- Ng, T.: Input parameters of discrete element methods. *J. Eng. Mech.* **132**(7), 723–729 (2006)
- Nguyen, H.B.K., Rahman, M.M.: The role of micro-mechanics on the consolidation history of granular materials. *Aust. Geomech. J.* **52**(3), 27–35 (2017)
- Nguyen, H.B.K., Rahman, M.M., Cameron, D.A., Fourie, A.B.: The effect of consolidation path on undrained behaviour of sand - a DEM approach. In: Fusao Oka, A.M., Uzuoka, R., Kimoto, S. (eds.) *Computer Methods and Recent Advances in Geomechanics*. CRC Press: Taylor & Francis Group, pp. 175–180 (2015)
- Nguyen, H.B.K., Rahman, M.M., Fourie, A.B.: Undrained behaviour of granular material and the role of fabric in isotropic and K0 consolidations: DEM approach. *Géotechnique* **67**(2), 153–167 (2017)
- Nguyen, H.B.K., Rahman, M.M., Fourie, A.B.: Characteristic behaviour of drained and undrained triaxial tests: a DEM study. *J. Geotech. Geoenvir. Eng.* **144**(9), 04018060 (2018)
- Olson, S.M., Stark, T.D., Walton, W.H., Castro, G.: 1907 static liquefaction flow failure of the north dike of wachusetts dam. *J. Geotech. Geoenvir. Eng.* **126**(12), 1184–1193 (2000)
- Perez, J.C.L., Kwok, C.Y., O'Sullivan, C., Huang, X., Hanley, K.J.: Exploring the micro-mechanics of triaxial instability in granular materials. *Geotechnique* **66**(9), 725–740 (2016)
- Rabbi, A.T.M.Z., Rahman, M.M., Cameron, D.A.: Undrained behavior of silty sand and the role of isotropic and K0 consolidation. *J. Geotech. Geoenvir. Eng.* **144**(4), 04018014 (2018)
- Rabbi, A.T.M.Z., Rahman, M.M., Cameron, D.A.: Critical state study of natural silty sand instability under undrained and constant shear drained path. *Int. J. Geomech.* **19**(8), 04019083 (2019)
- Rahman, M., Lo, S.: Undrained behavior of sand-fines mixtures and their state parameter. *J. Geotech. Geoenvir. Eng.* **140**(7), 04014036 (2014)

- Satake, M.: Fabric tensor in granular materials. In: Proceedings of the IUTAM Symposium on Deformations and Failure of Granular Materials 1982, the Netherlands: Balkema, Rotterdam, pp. 63–68 (1982)
- Thornton, C.: Numerical simulations of deviatoric shear deformation of granular media. *Geotechnique* **50**(1), 43–53 (2000)
- Wei, X., Yang, J.: A critical state constitutive model for clean and silty sand. *Acta Geotechnica* **14**, 329–345 (2018)
- Zhang, J., Lo, S.-C.R., Rahman, M.M., Yan, J.: Characterizing monotonic behavior of pond ash within critical state approach. *J. Geotech. Geoenviron. Eng.* **144**(1), 04017100 (2018)



Stiff Degradation of Granular Material – A DEM Approach

Md. Mizanur Rahman^{1(✉)}, Hoang Bao Khoi Nguyen²,
and Hung-Chun Wang²

¹ Water and Natural Resources Natural and Built Environments Research Centre (NBERC) and Geotechnical Engineering, School of Natural and Built Environments, University of South Australia, Adelaide, Australia
Mizanur.Rahman@unisa.edu.au

² School of Natural and Built Environments, University of South Australia, Adelaide, Australia
Khoi.Nguyen@unisa.edu.au,
wanhyll18@mymail.unisa.edu.au

Abstract. The stiffness degradation of granular materials such as soils due to cyclic loading has been widely explored in the experimental studies, mostly in triaxial or oedometer apparatus. Such behaviour can be observed due to the cyclic loading at very small strains, which is considered as elastic range. While increasing the cyclic strain amplitude, the stiffness or secant shear modulus (G) reduces non-linearly and forms a S-shaped curve with the shear strain (γ). A discrete element method (DEM) is adopted in this study to have enhance the understanding of soil response to cyclic strain amplitude. It was found later in this study that the stiffness of granular material reduced as void ratio (e) increased. The maximum stiffness was highly dependent on e , but not p' . However, the normalized stiffness degradation curve was influenced by both initial states i.e. e and p' ; p' seemingly had more impact of the normalized stiffness degradation than e .

1 Introduction

Stiffness degradation is the phenomenon that stiffness or shear modulus (G) reduces with increasing applied strain amplitude. This phenomenon reflects the instability of granular material due to earthquake (or cyclic) loading. Idriss et al. (1978) reported that the stiffness of soils reduced non-linearly with the progression of cyclic loading cycle. Vucetic and Dobry (1988) found that the non-linear degradation progress was dependent on the consolidation history (over-consolidation, or normal consolidation), cyclic strain amplitude and number of cycles. The stiffness or shear modulus at small strain was reported as the maximum value. To predict the small strain stiffness (G_0), Hardin and Richart Jr. (1963) proposed an empirical equation of G_0 by considering the initial states of soil i.e. void ratio (e) and mean effective stress (p'). Yang and Gu (2013) later reported that G_0 may not be dependent on the particle size. Under critical state soil mechanics (CSSM) framework, some studies (Goudarzy et al. 2017; Goudarzy et al. 2016; Rahman et al. 2012) predicted G_0 by using the state parameter (ψ), which was

proposed by Been and Jefferies (1985). However, there are some limitations for laboratories study of cyclic behavior such as membrane penetration, non-uniformity, etc. In addition, the soil interaction or soil's internal structure cannot be fully explored in the laboratory.

Therefore, discrete element method (DEM), proposed by Cundall and Strack (1979), has been widely adopted to capture the qualitative behavior of granular material (Huang et al. 2014; Nguyen and Rahman 2017; Nguyen et al. 2015; Nguyen et al. 2018a, b; Rahman et al. 2018; Yang and Dai 2011; Zhao and Guo 2013). Such a technique does not suffer from experimental limitation of non-uniformity and allows the understanding of internal structure of soil. Gu et al. (2013) adopted 2D circular particle to investigate the small strain stiffness and reported that the stress state or ratio (i.e. isotropic and anisotropic) can affect the G_0 value. Nguyen et al. (2018a, b) also investigate the effect of anisotropic stress states on small strain stiffness under true-triaxial condition by using DEM.

The purpose of this study is to determine whether DEM can qualitatively capture the stiffness degradation behavior of granular material. Due to the angularity features of natural soils, this study considered the assemblies of 3D ellipsoid particles to observe the cyclic shearing response of granular material. The main objective of this research is to investigate the effect of the state of granular material on the overall stiffness degradation.

2 Methodology

2.1 DEM Parameters

The specimen of ellipsoid particles was generated within periodic boundary. All these particles were assigned a normal contact stiffness of 10^8 N/m, a ratio of tangential to normal contact stiffness of 1.0, a coefficient of friction at particle contacts of 0.50 and the coefficient of (rotational and translational) body damping of 0.05. A linear contact model and periodic boundary condition were used in this study.

2.2 Controlling Feedback

The cyclic strain-controlled simulations under undrained (constant volume) condition were performed to investigate the stiff degradation phenomenon due to strain amplitude. The procedure for the simulations

- Isotropic consolidation: The DEM specimens were isotropically consolidated by stress-controlled mode.
- Undrained cyclic shearing: Shearing was applied in the major principal directions (ε_1). To maintain undrained or constant volume condition, the strains in minor principle directions (ε_2 and ε_3) were adjusted so that there is no volume or void ratio change i.e. $d\varepsilon = 0$; where 'd' indicates the rate of change.

Note, the cyclic shearing was applied with increasing strain amplitude. For one strain amplitude, 5 cycles were performed to define the slope of stress-strain curve.

3 Define Stiffness in DEM

Figure 1 showed the method to define the stiffness for different strain amplitude. The stiffness or secant modulus (G) is the gradient of the curve in the shear stress (τ) - strain (γ) space. These parameters can be expressed as the following

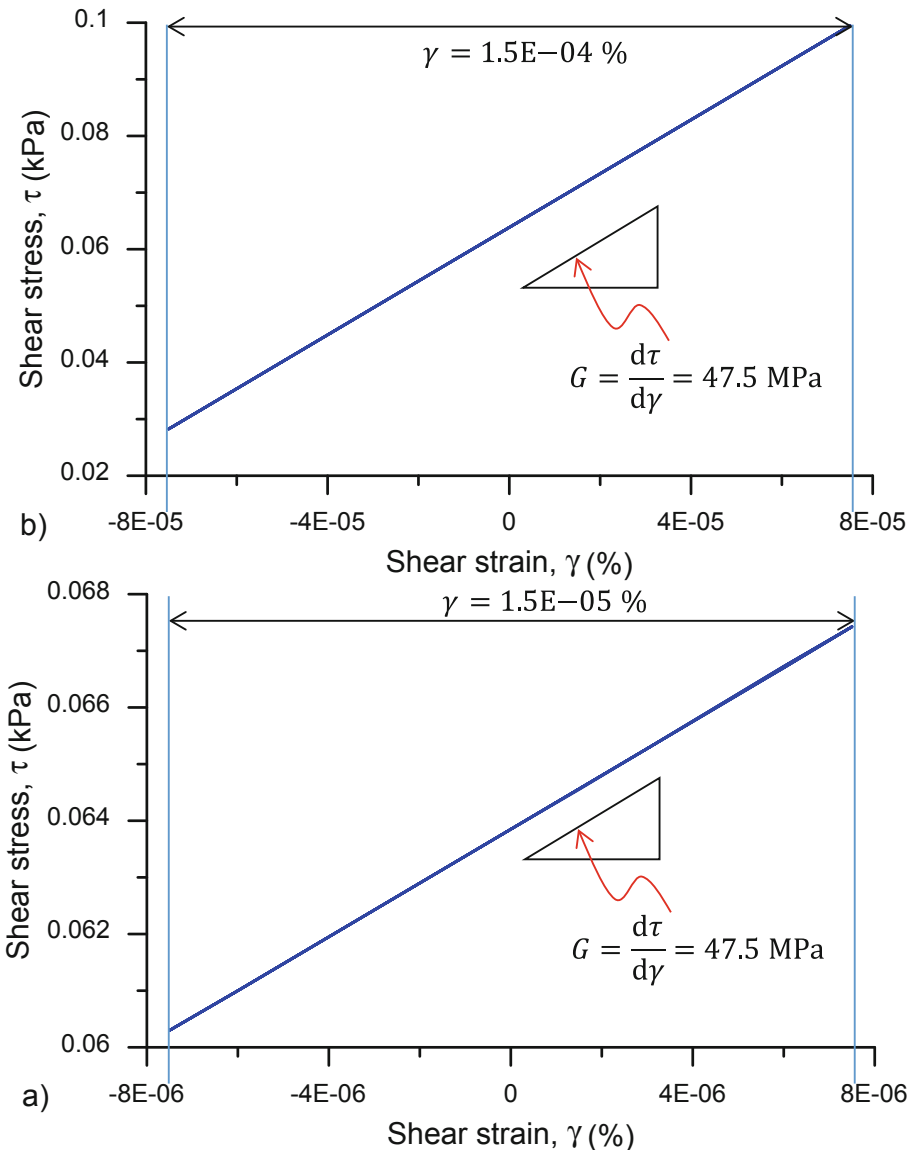


Fig. 1. Define the stiffness of granular material due to cyclic loading

$$\tau = (\sigma'_1 - \sigma'_3)/2 \quad (1)$$

$$\gamma = (\varepsilon_1 - \varepsilon_3)/2 \quad (2)$$

At very small strain i.e. 1.5E–5%, the maximum secant modulus (G_0) was defined. It was found that G remained the same even with higher strain amplitude i.e. 1.5E–4% (see Fig. 1b). Therefore, these strain amplitudes were still in elastic range, where there is no stiffness degradation happening. Note, as the shearing was still in elastic range, the loading and unloading paths coincided as the straight line in Fig. 1.

4 Results

Figure 2 showed the stiffness degradation with the progression of cyclic loading for the simulation CYC1. It can be clearly seen that G still remained constant at its maximum value ($G/G_0 = 1$) until reaching 0.1% strain. This indicated that this specimen still behaved like elastic body up to 0.1% strain. After 0.1% strain, G gradually reduced with increasing strain amplitude. It should be noted that G steeply decreased between 0.1 to 2%. After that, the rate of reduction was seemingly lower.

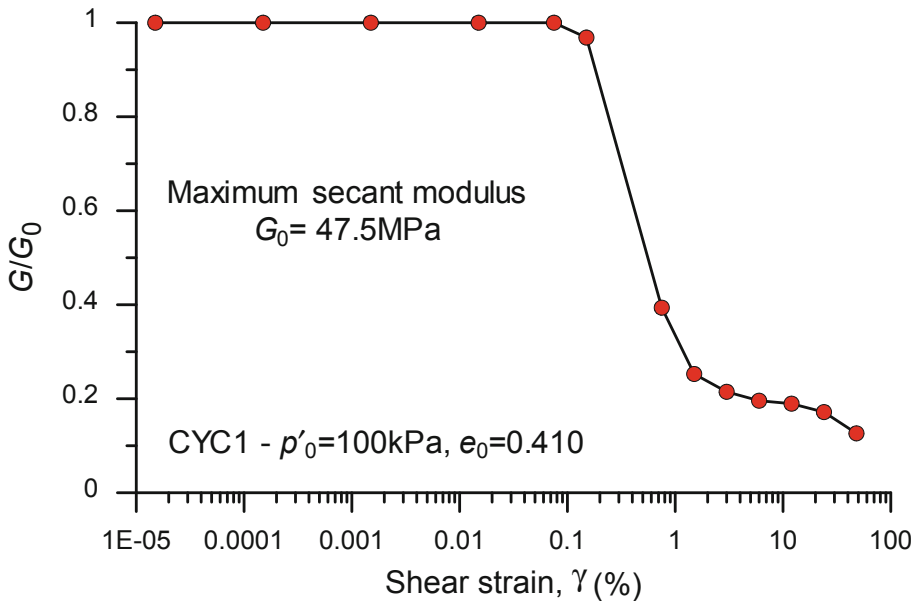


Fig. 2. Stiffness degradation curve

It was reported in the literatures (Hardin and Richart Jr. 1963) that the stiffness of soil may affected by the soil's initial states (e and p'). Figure 3a showed the effect of e and p' on G . Two simulations, CYC1 and CYC2, had different p'_0 (i.e. 100 kPa and

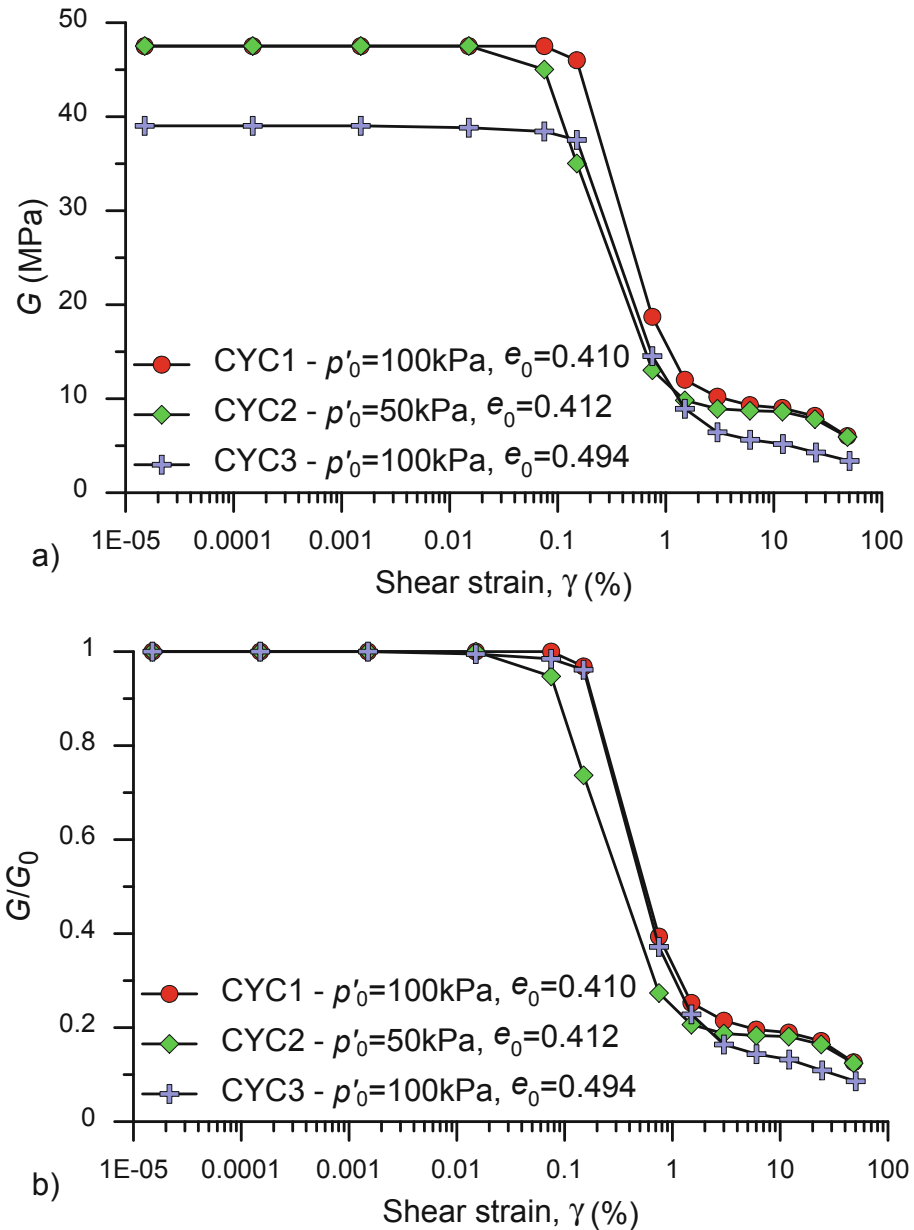


Fig. 3. Effect of initial states on the stiffness degradation curve in (a) $G - \gamma$ and (b) G/G_0 spaces.

50 respectively) and very close e_0 values (i.e. 0.410 and 0.412 respectively). It can be seen that p' does not have clear impact on the maximum G (G_0). However, after elastic range (between 0.1% to 2% strains), CYC2 with p'_0 of 50 kPa showed steeper reduction

in G compared to CYC1 with p'_0 of 100 kPa. However, the two curves coincided at higher strains i.e. 10%. Therefore, p' only have significant influence on G within a small range of strains (after elastic range up to approximately 10%).

On the other hand, two simulations, CYC1 and CYC3, had different e_0 (i.e. 0.410 and 0.494 respectively) and similar p'_0 values of 100 kPa, were performed to investigate the effect of e on G . G_0 for CYC3 (39 MPa) was smaller than CYC1 (49 MPa). It seemed that the gradients of the stiffness curve were quite similar (only the magnitudes were different). Figure 3b showed the normalized stiffness degradation curve. Because p' have high impact on G after the elastic range up to high strains (i.e. 10%), the normalized curve were seemingly affected by p' rather than e . As e only affects the magnitude of G , the normalized curves for CYC1 and CYC3 were identical until approximately 2%, where the plastic deformation may be more dominant than elastic deformation.

5 Conclusions

This study adopted the DEM to investigate the stiffness (G) degradation behavior of granular material. The findings of this study are listed as the followings:

- DEM can be qualitatively captured the stiffness degradation behavior of granular material, which can provide more in-depth understanding of such a behavior.
- The maximum stiffness (G_0) of a granular material can be achieved at very small strains i.e. less than 0.01%, where elastic deformation is dominating.
- The initial states of granular material also have significant impact on G . p' has more effect on the gradient of the stiffness degradation curve, whereas e has more effect on the magnitude of G .

References

- Been, K., Jefferies, M.G.: A state parameter for sands. *Géotechnique* **35**(2), 99–112 (1985)
- Cundall, P.A., Strack, O.D.: A discrete numerical model for granular assemblies. *Geotechnique* **29**(1), 47–65 (1979)
- Goudarzy, M., Rahemi, N., Rahman, M.M., Schanz, T.: Predicting the maximum shear modulus of sands containing nonplastic fines. *J. Geotech. Geoenviron. Eng.* **143**(9), 06017013 (2017)
- Goudarzy, M., Rahman, M.M., König, D., Schanz, T.: Influence of non-plastic fines content on maximum shear modulus of granular materials. *Soils Found.* **56**(6), 973–983 (2016)
- Gu, X., Yang, J., Huang, M.: DEM simulations of the small strain stiffness of granular soils: effect of stress ratio. *Granular Matter* **15**(3), 287–298 (2013)
- Hardin, B.O., Richart Jr., F.: Elastic wave velocities in granular soils. *J. Soil Mech. Found. Div.* **89**(Proc. Paper 3407) (1963)
- Huang, X., O'Sullivan, C., Hanley, K., Kwok, C.: Discrete-element method analysis of the state parameter. *Géotechnique* **64**(12), 954–965 (2014)
- Idriss, I.M., Dobry, R., Sing, R.: Nonlinear behavior of soft clays during cyclic loading. *J. Geotech. Geoenviron. Eng.* **104**(ASCE 14265) (1978)

- Nguyen, H.B.K., Rahman, M.M.: The role of micro-mechanics on the consolidation history of granular materials. *Aust. Geomech.* **52**(3), 27–36 (2017)
- Nguyen, H.B.K., Rahman, M.M., Cameron, D.A., Fourie, A.B.: The effect of consolidation path on undrained behaviour of sand - a DEM approach. In: *Computer Methods and Recent Advances in Geomechanics*, pp. 175–180. CRC Press (2015)
- Nguyen, H.B.K., Rahman, M.M., Fourie, A.B.: Characteristic behaviour of drained and undrained triaxial tests: a DEM study. *J. Geotech. Geoenviron. Eng.* **144**(9), 04018060 (2018a)
- Nguyen, H.C., O'Sullivan, C., Otsubo, M.: Discrete element method analysis of small-strain stiffness under anisotropic stress states. *Géotechnique Lett.* **8**(3), 183–189 (2018b)
- Rahman, M.M., Cubrinovski, M., Lo, S.R.: Initial shear modulus of sandy soils and equivalent granular void ratio. *Geomech. Geoengin.* **7**(3), 219–226 (2012)
- Rahman, M.M., Nguyen, H.B.K., Rabbi, A.T.M.Z.: The effect of consolidation on undrained behaviour of granular materials: a comparative study between experiment and DEM simulation. *Geotech. Res.* **5**(4), 199–217 (2018)
- Vucetic, M., Dobry, R.: Degradation of marine clays under cyclic loading. *J. Geotech. Eng.* **114**(2), 133–149 (1988)
- Yang, J., Dai, B.: Is the quasi-steady state a real behaviour? A micromechanical perspective. *Géotechnique* **61**, 175 (2011)
- Yang, J., Gu, X.: Shear stiffness of granular material at small strains: does it depend on grain size? *Géotechnique* **63**(2), 165 (2013)
- Zhao, J., Guo, N.: Unique critical state characteristics in granular media considering fabric anisotropy. *Géotechnique* **63**(8), 695–704 (2013)



Conventional Method to Estimate Settlement of Plate Subjected to Bi-Axial Loading – Part II

Khaled R. Khater¹(✉) and Mohamed Abouzied²

¹ Civil Engineering Department, Fayoum University, Fayoum, Egypt
krk26@fayoum.edu.eg

² Consultation Center, Fayoum University, Fayoum, Egypt

Abstract. A plate bi-axially loaded presents the general loading case of shallow foundations. Raft its columns load resultant does not lay on its center of area is one example. Isolated footing subjected to moment and vertical load eccentric or concentric is another example. Not to mention if wind or seismic effect is considered or involved. Even though, most of conventional methods were developed to predict settlement induced due to concentric loading conditions. This research presents novel simplified method for settlement prediction of rigid plate center and corners subjected to bi-axial load. The method works for rectangular plate rests on Mohr-Coulomb soil having any L/B ratio, starting from square up to strip footing. Also it suits any E_s and μ_s values. This method uses one graph that contains two curves; alternatively two empirical equations have been given. The generalization of this method is proved analytically. The used methodology and method to develop this technique was parametric study, finite element, Plaxis 3D, and first principals. Furthermore, an experimental investigation has been performed. A physical model has been manufactured and used to run series of tests. Steel rigid plates rest on dense sand and bi-axially loaded have been tested. Various lengths to breadth ratio L/B as well as several bi-axial eccentricities are examined. Moreover and above, the experimental study has been extended to cover field work. There a series of bi-axially loaded plates having different length to breadth ratios L/B were researched. The behaviour of the plate based on experimental work confirms and match the suggested conventional method behaviour. However, elimination of scale effect could be achieved by using more advanced physical models, such as wind tunnel. This is suggested as a further research work.

1 Introduction

This paper is part (II) of a previously published paper has the same title hyphenated, with index (I). Part (I) is a numerical study based on the finite element method. The current extension, i.e. part (II) is an experimental investigation. It consists of two categories; first one is a laboratory routine work and physical model tests while the second is a field investigation, i.e. in-Situ study. The main outcome of the first part (I) is a simplified, novel and general conventional method suggested to calculate the settlement of a plate corner and center subjected to bi-axial concentrated load, as a first approximation. It has been denoted as “Khater method”. The running part, i.e. (II),

studies experimentally the behavior of the biaxial loaded plates, as well as assuring the credibility of the suggested novel and general conventional method.

2 Literature Review

This main title consists of two sub-titles. The first one briefly highlights samples of previously published technical papers oriented to topic. The reviewed references are focused on the key words, settlement, eccentric and plate. The presented papers have been arranged methodologically. The second sub-title summarizes the previously published paper, i.e. (I). This connects and integrates the two papers together. Lastly, the literature review ended-up by research question, hypothesis and theme.

2.1 Literature Review: Published by Others

Salimath and Pender (2014) studied the stress beneath square footing subjected to vertical load and moment applied at its centroid. A 3D-finite element model was carried out by using PLAXIS 3D, with soil-footing interface element and the hardening soil model. Enkhtur et al. (2013) improved the settlement influence factors for foundations subjected to concentric loading previously suggested by Mayne and Poulos (1999). Zedzn and Maulood (2017) presented a study investigating the behavior of square footing subjected to eccentric inclined loading with respect to vertical and horizontal displacement. The 3D finite element analysis, Mohr-Coulomb criterion to model the soil and rigid foundation concept were adopted.

Patra et al. (2013) achieved a series of physical model tests to study the strip footing subjected to vertical and inclined eccentric loads. Based on the obtained settlement results, an empirical technique has been developed to estimate the average settlement. The empirical procedure is valid for D_f/B ratio varying from zero to 1.0 and the eccentricity ratio e_x/B changes from zero to 0.15. Braim et al. (2016) investigated the effect of load eccentricity on settlement of strip footing rested on medium dry sand. A series of small-scale 1 g physical models was carried out. A rigid plate was used to represent the case of strip footing. Three different eccentricities have been considered, they are located at 0.0 B, 0.05 B and 0.1 B measured from the long axis. Photogrammetry and image velocimetry (PIV) methods were used to examine the failure pattern and rotations.

Kaya and Ornek (2013) performed 48 model tests and numerical investigation concerning the case of T-shaped footings subjected to eccentric load. The tests were performed on loose and dense sand conditions. The experimental stage was followed by numerical analyses based on 2D computer program. The numerical results underestimated the physical model results. Nandakumaran and Senathipathl (1981) suggested a simple and approximate method to estimate the settlement of footings subjected to eccentric load. It is concluded that when footings are subjected to vertical loads and moments, as during a seismic, the proposed method can be employed with advantage.

Algin (2009) introduced analytical solution for estimating the settlement under eccentrically loaded rectangular surface footings resting on elastic mass. The presented

solution obtained by integrating a strain expression based on Boussinesq stress equations. The paper represents a significant step forward in calculating the elastic settlement, under eccentrically loaded rectangular footings.

Lutenegger and DeGroot (1995) prepared a comprehensive state-of-the-art reviewing the procedures used to estimate settlement of shallow foundations resting on granular soil. The results of the project indicate that a number of methods are outdated and should not be used. The report enables researchers to improve the existing methods to allow more reliable settlement estimation.

2.2 Literature Review: Published by Authors

Khater et al. (2019) recently published technical paper has the same title as this one, but hyphenated with index (I). Within this subtitle a short summary is reported to connect the running paper with the previous one. To avoid un-needed elongation any figure, equation, analysis, prove or conclusion abstracted from part (I) and stated here will be taken for granted, as a restricted rule. If anyone is interested in the details, kindly refer to the paper itself;

2.2.1 Methodology and Method

The methodology or the strategy used to fulfill the goal of the research was the parametric study technique. Figure 1 shows the plate plan and the bi-axial eccentricity route. The investigated plate aspect ratios L/B were 1.0, 1.50 and 2.0. The considered eccentricity ratios e_x/B and e_y/L varied from 0.00 to 0.15 in a uniform interval.

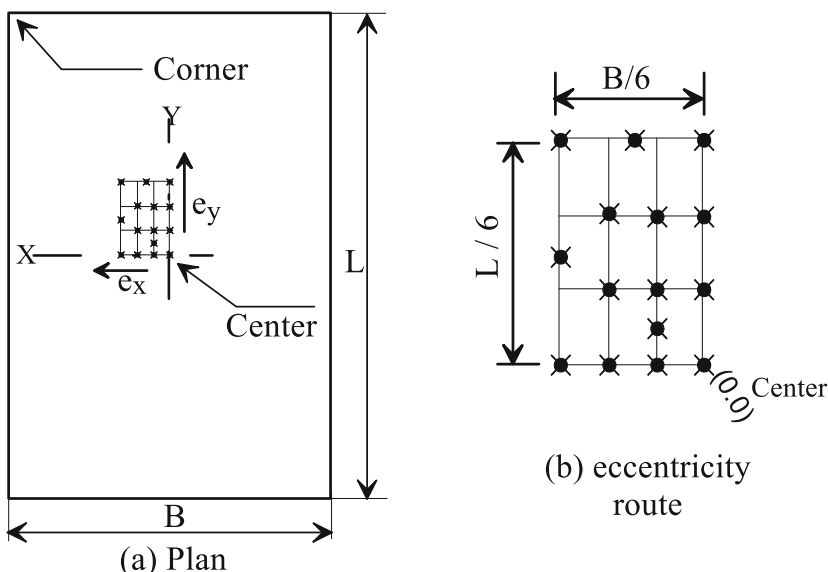


Fig. 1. Plate plan and eccentricity route

The used research method was the finite element analysis because it is an outstanding method to manage settlement problems. Accordingly, Plaxis 3D-Foundation has been selected to be the research tool due to its ranking. Three types of integrated elements have been combined then used to build up a representative finite element model. They are plate, interface and wedge elements. The rough interface option has been considered, i.e. $R_{\text{inter}} = 1.0$. This study deals with bi-axial loading and the plate tilting is a must. The virtual thickness of the interface element will not be uniform beneath the plate. To avoid this no slip or gapping option was adopted. Mohr-Coulomb model adopted because it is suitable one to analyze cases of dry dense sand deformations.

2.2.2 Model Parameters and Verification

The dense sand and the concrete plate element parameters have been abstracted based on Patra et al. (2013). For soil, the dry unit weight is 14.37 kN/m^3 , Young modulus $E_s = 42000 \text{ kN/m}^2$, Poisson's ratio $\mu_s = 0.33$, friction angle $\Phi = 40.8^\circ$ and dilatancy angle $\Psi = 10.8^\circ$. For the concrete plate element the unit weight is 24.0 kN/m^3 , Young modulus $E_p = 2 \times 10^7 \text{ kN/m}^2$ and Poisson's ratio $\mu_p = 0.20$.

Same models with different dimensions had been tested and the results compared with closed form solutions. Based on evaluation of results a plate has width B and length L , the sufficient dimensions of finite element model are; [7B by (L+6B)] in plan and 5B in depth. The vertical stresses beneath the center point of a square flexible loaded area has been calculated vs. depth based on Fadum (1948) and compared with the finite element model results and agree well.

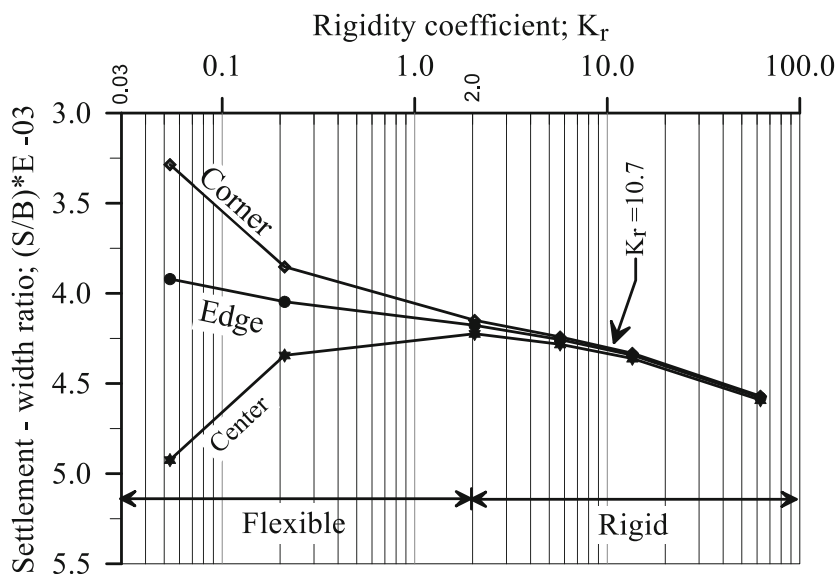
To choose the thickness of the plate that presents the rigid case, it has been assumed that a rigid plate is the plate of a thickness "d" and the settlements of any three of its points are nearly the same. The monitored points were center, corner and the mid side. Different plate thickness have been examined, the finite element model runs, the settlements recorded then plotted, Fig. 2. The figure y-Axis is the normalized settlement and x-Axis is rigidity coefficient, K_r given by Eq. 1, Borowicka (1936).

$$K_r = \frac{1}{6} \left(\frac{1 - \mu_p^2}{1 - \mu_s^2} \right) \left(\frac{E_p}{E_s} \right) \left[\frac{d}{B} \right]^3 \quad (1)$$

Where E 's and μ 's are the elastic constants of the plate and soil, d is the plate depth. Figure 2 shows, as K_r increases settlement of plate center decreases while settlement of the corner and the mid side increases. At $K_r = 2.0$ three curves became one, i.e. plate is rigid. Based on Eq. 1 the K_r of the used plate of $d = 1.0\text{-m}$ is 10.7, i.e. rigid.

2.2.3 Performing the Parametric Study

The parametric study has been performed for three ratios of L/B , i.e. 1.0, 1.5 and 2.0 and 15 bi-axial eccentricity per each ratio. The outcome were settlement of plate corner S_{ECr} , settlements of plate center S_{EC} and S_{CC} , the latter is concentric loading.

Fig. 2. Rigidity coefficient K_r vs. S/B ratios

2.2.4 Relative Eccentricity Hypotenuse Concept

This article is the key of part (I) and its main contribution. It is a hypothetical, imaginary thought convinced us. It is a matter of argument, one may agree and another may not. It is born and introduced by us for the first time, see Fig. 3-b.

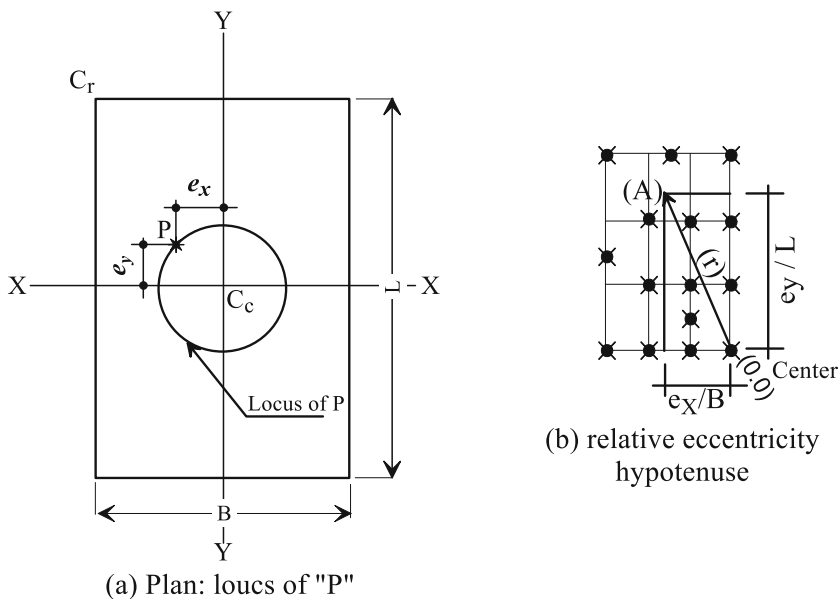


Fig. 3. Relative eccentricity hypotenuse, “r”

The arrow join plate center with point (A) is denoted “relative eccentricity hypotenuse”, r . To convert eccentricities e_x and e_y from “real” numbers to “imaginary” ratios, divide each “e” by a parallel side of the plate, i.e. (e_x/B) and (e_y/L) . For that, “ r ” is called relative eccentricity. The term hypotenuse came from its way of calculation, Eq. 2. The value of “ r ” could be calculated but not possible to be drawn because it has no units, i.e absolute value. This is the idea of part (I).

$$r = \sqrt{(\frac{e_x}{B})^2 + (\frac{e_y}{L})^2} \quad (2)$$

During part (I), “ r ” presents x-axis of all curves the above strategy normalized the values of x-axis, and also generalized the solution for any plate dimensions B and L. Y-axis of a settlement curves is normalized by dividing the corner settlement, S_{ECr} and center settlement S_{EC} of eccentrically loaded plate by the settlement of its center when concentrically loaded, S_{CC} . Two ratios denoted by R_S and called “Settlement correction factor” have been introduced, Eqs. 3 and 4.

$$R_S = \frac{S_{ecr}}{S_{cc}}; \text{ for plate corner} \quad (3)$$

$$R_S = \frac{S_{ecc}}{S_{cc}}; \text{ for plate center} \quad (4)$$

The above strategy normalized the x-axis and y-axis co-ordinate and generalized the solution for any values of the deformation parameter, i.e. E_S and μ_S .

2.2.5 Presentation of the Results: Khater Method

Based on Eqs. 2, 3 and 4, two sets of data have been generated and then plotted for the three L/B ratios as well as all the performed eccentricities on one graph of two curves. Then the curve fitting technique had been used to reproduce two empirical curves. One curve is used for predicting the settlement of the plate corner. The other one is used for predicting the settlement of the plate center, Fig. 4.

Figure 4, “Khater chart” introduces the goal of part (I) and needed for part (II) to complete this series of research work. It presents a simple approximate conventional method used to predict the settlement of rectangular plate center and corner, the plate bi-axially loaded. Three important aspects should be discussed before further going on. They are the Khater method procedures, its usage and advantages and finally its scope of application. At the end of this subtitle a numerical example has been given.

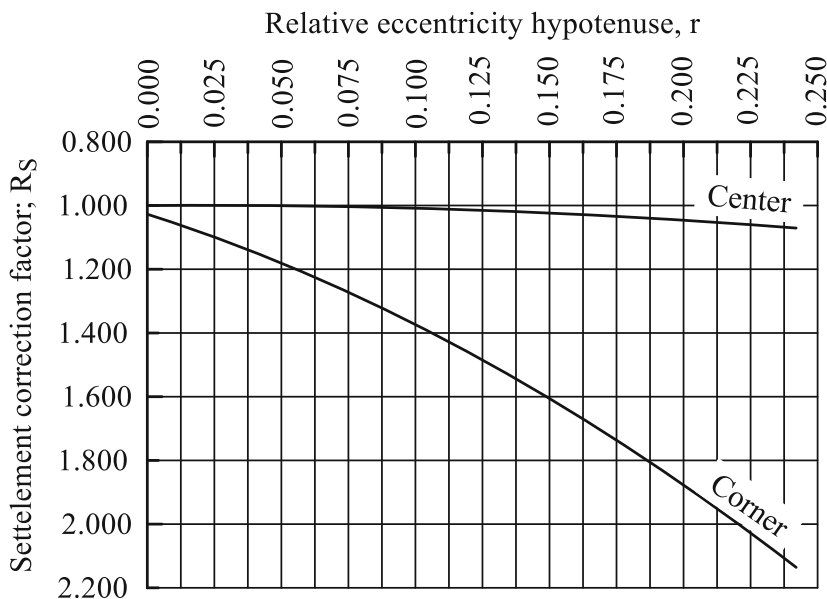


Fig. 4. “r” vs. “R_S” - “Khater chart”

The method procedures are as follows:

1. Calculate the elastic settlement of the center of area of flexible rectangular plate subjected to uniform concentric pressure, S_e.
2. Any closed form solution could be used, Fadum, R.E. 1948 is recommended.
3. Use Fig. 2 to convert the settlement of flexible loaded area S_e to settlement of a rigid plate S_{CC} based on its K_r. However, S_{CC} could be taken as 85% of S_e as an acceptable approximation in most cases.
4. Use Eq. 2 to calculate the relative eccentricity hypotenuse “r” based on the variables e_x, e_y, B and L. Then use Fig. 4 to get R_S-center and R_S-corner from the intersections of “r” with each curve and the y-axis.
5. Based on Eqs. 3 and 4, calculate the settlement of the plate corner S_{ECr} and the settlement of the plate center S_{EC}, respectively.

N.B: an alternative to Fig. 4, the following two empirical equations “Khater equations” could be used. Those two equations created based on curve fitting technique, polynomials of the second order with regression factors R equal to 98%:

$$R_{S-Corner} = 1.03 + 2.68r + 7.67r^2 \quad (5)$$

$$R_{S-Center} = 1.06 - 0.06r + 1.47r^2 \quad (6)$$

The above mention simple conventional method has many beneficial applications and usages such as the follows or similar:

1. Raft foundation its load resultant is shifted of its center of area.
2. Isolated footing not symmetrically loaded.
3. Footing or raft subjected to concentric loads and bi-axial moments.
4. Shallow foundation subjected to vertical loads and active seismic action.

The scope of application of this method may be divided into two categories. The first category is any rectangular rigid plate rests on dense sand and subjected to bi-axial loading and its length to breadth ratio L/B is 1.0, 1.5 and 2.0 or in between. These are the limitation of the cases of studied, hence they presents its scope and range of application by default. It is believed that the scope of application and use is much wider than the above. The author believes this method could be applied and used for:

1. Any plate has “at least” one axis of symmetry, regardless of its the shape or its aspect ratios.
2. Any type of loading, as long as, it could be re adjusted to simulate bi-axial vertical concentrated load.
3. Any type of soil, regardless its elastic properties, i.e. E_s and μ_s .

The following paragraphs are the prove of the above three opinions. The strategy will be used to investigate validity of Fig. 4 for any value of L/B ratio depends on the normal stress concept, Eq. 7 and Fig. 3.

$$\sigma_{Cr} = \frac{N}{A} \mp \frac{M_{xy}}{I_x} \mp \frac{M_{yx}}{I_y} \quad (7)$$

Where, $M_x = P \cdot e_y$, $M_y = P \cdot e_x$, $A = BL$, $N = P$, $y = 0.5 L$, $x = 0.5 B$, $I_x = B L^3/12$ and $I_y = L B^3/12$.

Substituting in Eq. 7 and re-arrange terms;

$$\sigma_{Cr} = \frac{P}{BL} \left(1 \mp 6 \frac{e_y}{L} \mp 6 \frac{e_x}{B} \right) \quad (8)$$

$$\sigma_{Cc} = \frac{P}{BL} \quad (9)$$

$$\frac{\sigma_{Cr}}{\sigma_{Cc}} = \left(1 \mp 6 \frac{e_y}{L} \mp 6 \frac{e_x}{B} \right) \quad (10)$$

σ_{Cr} is the stresses at the plate corner when it is eccentrically loaded, while σ_{Cc} is the stresses at the plate center when it is concentrically loaded. The elastic settlement, S_e equation in its simplest form is a function of the increases of stresses σ , the soil layer thickness h , and the soil elastic modulus E_s .

$$S_e = \frac{\sigma h}{E_s} \quad (11)$$

The values of h and E_s are constant beneath the same plate, if one multiply the numerator and denominator of the left hand side of Eq. 10 by (h/E_s) and then combined Eqs. 10 and 11 we get:

$$\frac{\sigma_{Cr}h/E_s}{\sigma_{Cc}h/E_s} = \frac{S_{Cr}}{S_{Cc}} = \left(1 \mp 6\frac{e_y}{L} \mp 6\frac{e_x}{B}\right) \quad (12)$$

Referring to Eqs. 3 and 4 in addition to Eq. 12, the equation of settlement correction factor, R_s is:

$$R_s = \left(1 \mp 6\frac{e_y}{L} \mp 6\frac{e_x}{B}\right) \quad (13)$$

The equation of relative eccentricity hypotenuse, r is Eq. 2, presents equation of an imaginary circle its center is the plate center and its circumference is the locus of the bi-axial load, hypothetically. Equations 3 and 12 are the x-axis and y-axis, respectively on which Fig. 4 has been constructed, all the variables are in dimensionless and repeated along both axes with the same power. This presents a general form for any B/L , e_y/L and e_x/B . Also, Fig. 4 could be used to any elastic soils regardless its properties. Based on Eq. 12, the modulus E_s exists in numerator and denominator.

A hint for logical verification, write-up Eqs. 2 and 13 for case of strip footing where $L = \infty$, infinity and $e_y = 0.0$

$$r = \sqrt[2]{\left(\frac{e_x}{B}\right)^2} = \frac{e_x}{B} \quad (14)$$

$$R_s = \left(1 \mp 6\frac{e_x}{B}\right) = (1 \mp 6r) \quad (15)$$

It is obvious that r and R_s as well as Fig. 4 are independent on the absolute values of B and/or e_x , for case of strip footing which is a special case of rectangular plate. This conclusion is extended to the case of $B = \infty$ and $e_x = 0.0$. Those two special cases presented the case of two ends of quarter of the circle shown in Fig. 3, logically the above conclusion is valued in between.

2.2.6 Khater Method: Numerical Example

Square rigid plate 3.0-m side-length subjected to eccentric vertical concentrated load of 1800 kN, eccentricity, $e_x = e_y = 0.30\text{-m}$. Rests on top of dense sand its $E_s = 50000 \text{ kN/m}^2$, Poisson's ratio $\mu_s = 0.35$ and its thickness 8.0-m. Calculate the settlement of its center and corner, as a first approximation.

Solution: (No equation numbering within this item will be used)

Based on Fadum (1948), $z = 0.5$ $h = 4.0\text{-m}$.

$m.z = B/2$ and $n.z = B/2$, $n = m = 0.375$ accordingly $I_r = 0.055$

$$\begin{aligned}\sigma_{\text{center}} &= 4.0 \{q I_r\}_{\text{quarter}} \\ &= 4.0\% 1800/9\% 0.055 = 44.0 \text{kN/m}^2\end{aligned}$$

$$S_{\text{center}}(\text{flexible}) = 44\% 8.0\% 1/50000 = 0.704 \text{ cm.}$$

$$S_{\text{center}}(\text{rigid}) = 0.85\% 0.704 = 0.598 \text{ cm} = 0.60 \text{ cm}$$

$e_x/B = e_y/L = 0.3/3.0$, substitute in Eqs. 2, 5 and 6;

$$\begin{aligned}r &= \left\{ (0.1)^2 + (0.1)^2 \right\}^{0.5} = 0.141 \\ R_{S-\text{Corner}} &= 1.03 + 2.68(0.141) + 7.67(0.141)^2 = 1.56 \\ R_{S-\text{Center}} &= 1.06 - 0.06(0.141) + 1.47(0.141)^2 = 1.08 \\ S_{e-\text{corner}} &= 1.56\% 0.60 = 0.936 \text{ cm} \\ S_{e-\text{center}} &= 1.08\% 0.60 = 0.648 \text{ cm}\end{aligned}$$

3 Experimental Investigation

An experimental program has been designed and performed as an extension and harmonizing to the numerical study. The main purpose of this experimental study is to explain the behavior of the bi-axial loaded plates, in the first place. Then, it may support the suggested conventional design method. It should be clear that, the shape factor effect prevents us from performing any numerical compressions.

Figure 5, introduces the flow chart of the performed experimental study. Briefly, the study consists of two main parts. Part one presents a physical laboratory model. While part two, presents the field investigation, i.e. plate load tests.

The physical model flow chart consists of three main activities. First one is the routine laboratory tests. Second activity is the model construction, manufacture, calibration and filling procedures by the soil sample. Last activity is the cases study. Five tests have been performed presenting two plates with two different aspect ratios.

The field investigation consists of five plate load tests with different plate shapes and aspect ratios. All plates have been loaded concentrically and eccentrically.

3.1 Physical Model

The physical model has been chosen to perform plate loading tests on a small size plates with different aspect ratios as well as different eccentricities, i.e. e_x and e_y . The foundation soil is well graded sand, SW. The tested plates are made of thick steel plates, 12-mm thickness and loaded by mechanical type Jack. The loads have been applied and measured by calibrated proving rings while the settlements have been measured by mechanical dial gauges. The following subtitles present the full details.

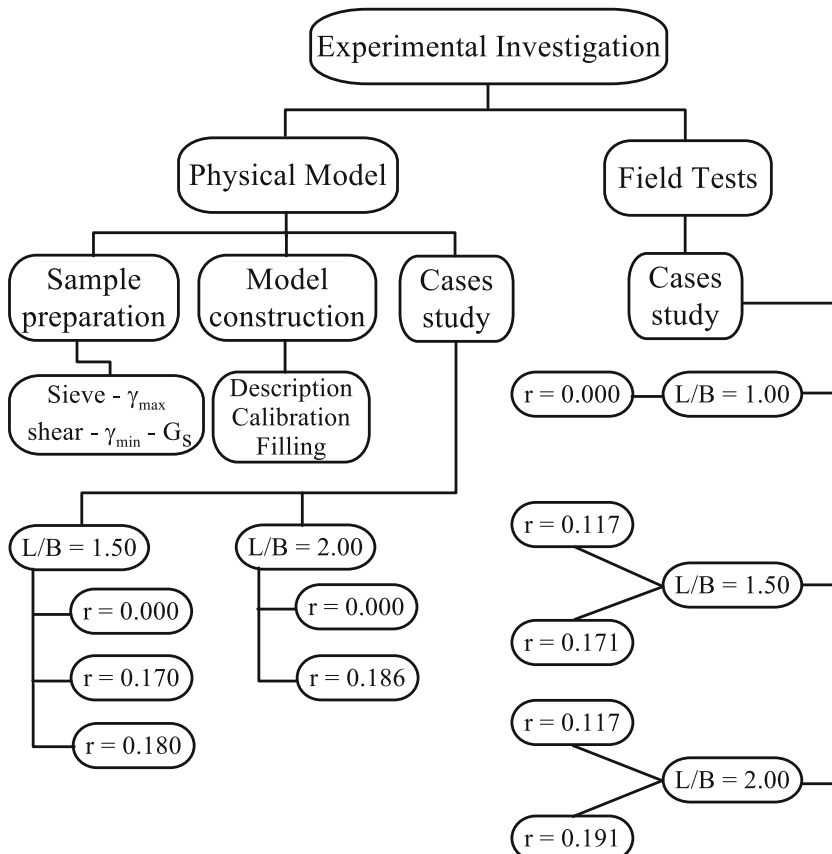


Fig. 5. Experimental program flow chart

3.1.1 Routine Tests: Sieve Analysis

The test has been run based on ASTM C136 standard test method. The graduation curve of the natural sample is shown in Fig. 6-B. Then reconstituted sample has been constructed as shown in Fig. 6-A, to fill the physical model sand tank.

The details of the reconstituted sample are shown in Table 1. It presents a well graded sand SW having $C_c = 1.81$, $C_u = 6.21$ and completely clean of fines and gravels.

3.1.2 Routine Tests: Compaction Test

The compaction test has been run on reconstituted sample by modified Proctor test with respect to ASTM D698-12e2. Figure 7 shows the maximum dry density as 19.10 kN/m^3 at 8.3% optimum moisture content.

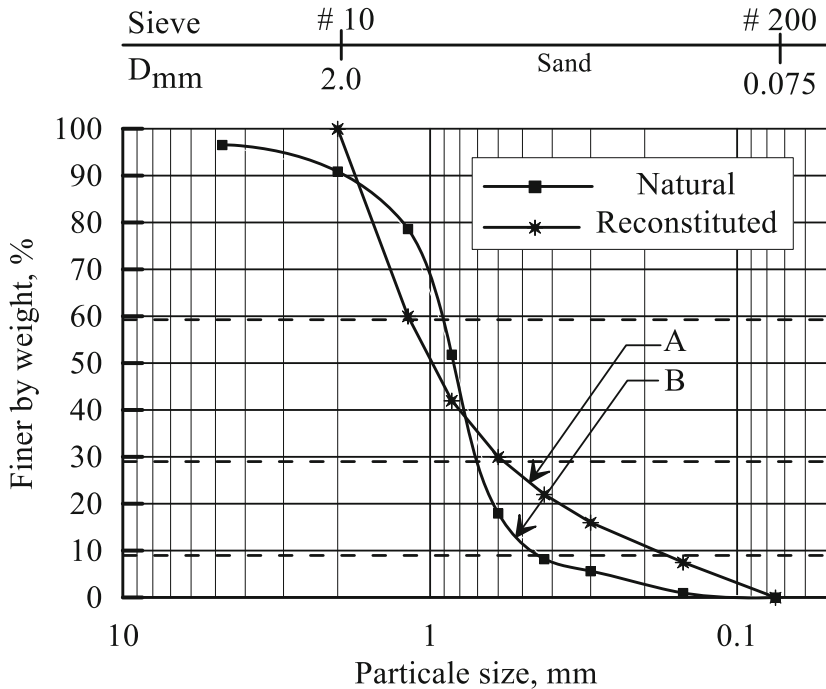


Fig. 6. The sieve analysis: natural and reconstituted sample

Table 1. The components of the reconstituted[♥] sample

Sieve number - ASTM	16	20	30	40	50	100	200
Opining, D mm	1.18	0.85	0.60	0.43	0.30	0.15	0.075
% Retained, by weight	40	18	12	8	6	8.5	7.5
% Finer, by weight	60	42	30	22	16	7.5	0

[♥] 1st author suggests denoting sample with these components as Fayoum sand.

3.1.3 Routine Tests: Shear Box

The shear box test has been run on the reconstituted sample with respect to ASTM D3080/D3080 M-11, standard test method. The sample were placed inside the shear box and compacted up to its maximum dry density, which equal to 19.10 kN/m^3 . As shown in Fig. 8, the angle of internal friction is 36.7° and apparent cohesion is 30.57 kN/m^2 . The equation of Mohr-Coulomb failure criterion envelope is;

$$\tau_f = 0.75\sigma_f + 30.6; \text{ kN/m}^2 \quad (16)$$

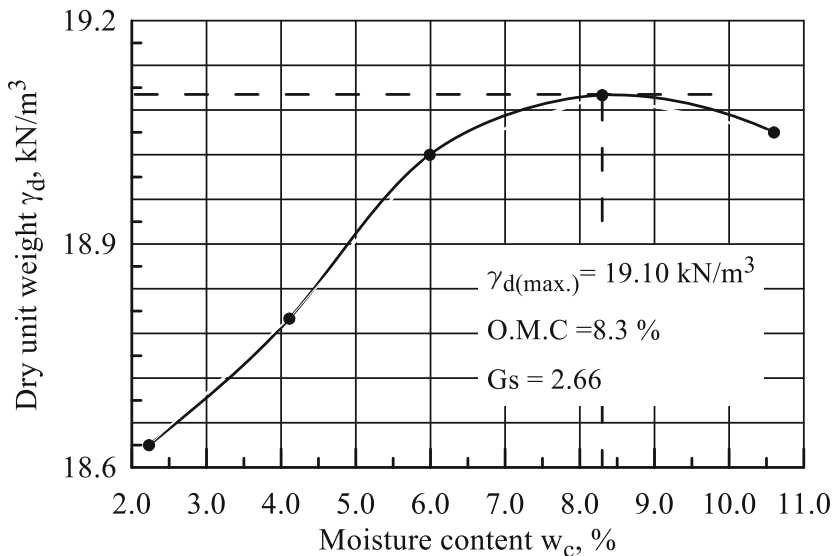


Fig. 7. The compaction: modified proctor test

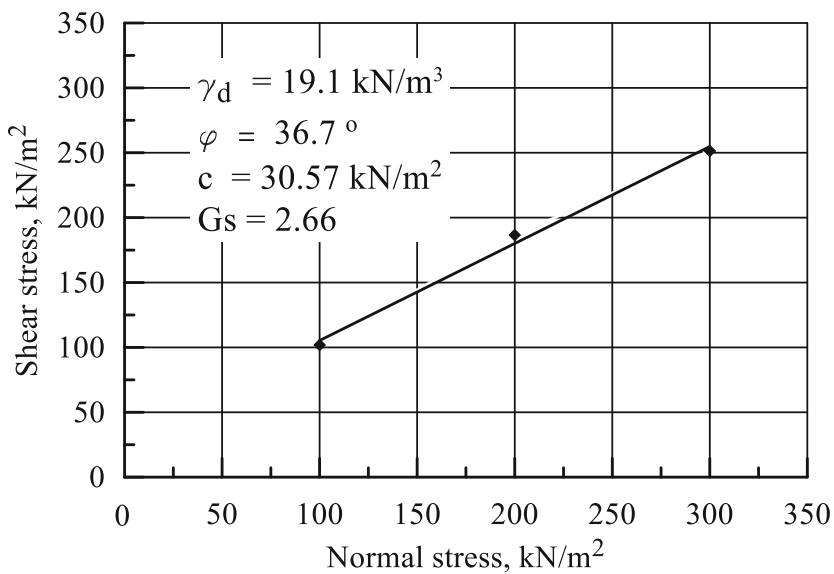
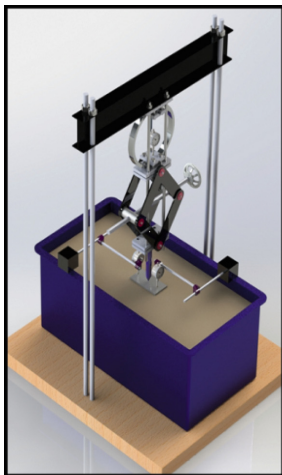


Fig. 8. The direct shear box test results

Furthermore, the minimum and maximum void ratios are calculated as 0.39 and 0.62 respectively. Moreover, the minimum dry density and solid specific gravity are 16.4 kN/m^3 and 2.66 respectively. Also, the angle of repose has been found 30.0° .



a. Schematic



b. Physical model



c. Plate & gauge



d. Sand tank

Fig. 9. Physical laboratory model

3.1.4 Model Description and Components

The model that used is a home-made one, i.e. manufactured by the first author. Simply, it applies vertical concentrated load on a point lies on the steel plate surface. The applied load is predetermined and increases manually and gradually starting from zero and up to 1.5 kN by any desired intervals. The load could be applied concentric, eccentric or bi-axial loading. The settlement of the steel plate is measured by mechanical dial gauges mounted on the corners of the plate.

Figure 9 shows the physical model and its components. Picture (a) presents schematic prepared by Solid Works software. Picture (b) is the mode itself filled with sand. Picture (c) shows steel plate loaded concentrically and two dial gauges mounted on two opposite corners. Picture (d) shows the sand tank which is built up from a skeleton of steel angles covered by steel plate all around. The sand tank dimensions are 75 × 35-cm in plan projection and 30-cm height. As shown in Fig. 9-b, the physical model itself consist of base steel plate and four vertical tension bolts. The bolts supporting horizontal I-Beam hanging on its mid span a proving ring connected to

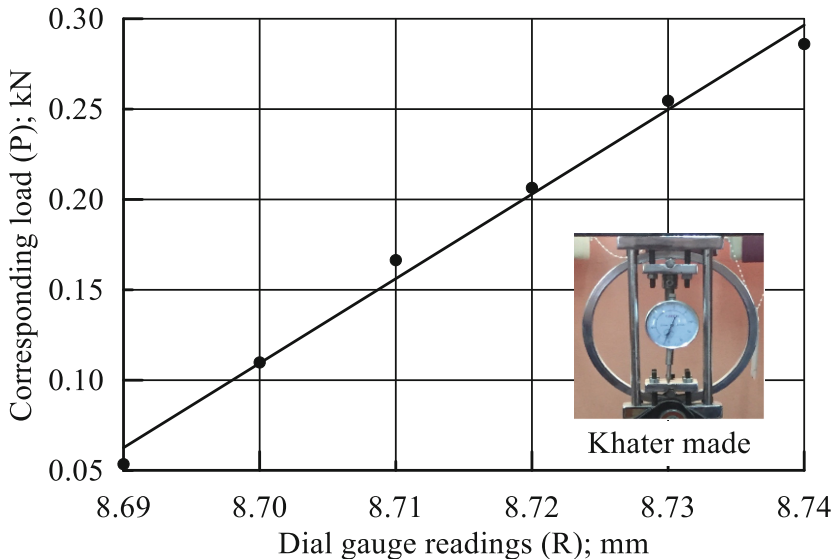


Fig. 10. Proving ring calibration chart

mechanical type Jack. The lower tip of the jack has a loading road used to apply the jack load to the tested steel plate to simulate the case shallow foundation.

3.1.5 Model Proving Ring Calibration

A proving ring has been designed, manufactured and calibrated to measure the applied force. Figure 9-b shows the proving ring, its location and connections. It has outer, inner diameter of 190 and 180 mm respectively. The ring thickness is 10 mm and its breadth is 15 mm. It has been made of spring steel has tensile strength of 685 MPa, yield strength 525 MPa, Poisson's ratio 0.29 and elastic modulus 200 GPa.

The proving ring has been calibrated with its connections and with its dial gauge and all mounted to the model during the calibration process. It has been calibrated with the aid of sensitive balance by using the jack to apply the load and measures the corresponding dial gauge divisions. Thirty trials forming six loads have been used and the calibration chart shown in Fig. 10 has been drafted. The line equation is;

$$P = 4.678 R + 40.579 \quad (17)$$

Where P is the load in kN, R is the dial gauge readings in mm and the equation confidence factor is 0.99.

3.1.6 Filling the Sand Tank

The sand tank has been filled twice; to present two different relative densities. The empty sand tank internal dimensions are 0.35 by 0.70 by 0.30 m, only 0.25-m height is filled with sand. Hence, the volume of sand is constant, i.e. 0.06125-m³. Preparing upper density, the input weight of sand was 1.128 kN, i.e. the dry density is 18.4

kN/m^3 . With respect to maximum and minimum dry densities, the relative density of this group is $Dr = 0.77$. For lower density the input weight of sand was 1.0474 kN , i.e. the dry density is 17.1 kN/m^3 and the relative density is $Dr = 0.29$. It is clear that relative density range covers herein cases of medium density sand.

The procedures of filling the sand tank starts by spreading the sand in 25 layers each 1.0 cm thickness after its compacting with a hammer weighs 0.022 kN and drops of 20 cm height, 11 time repeatedly. Then the hammer moves to the adjacent batch on the same layer and repeats the same process until the plan projection of the tank covered in a homogeneous way, horizontally. Then next layer placed and the process repeated so on and so far 25 times; this gives dry density of 18.4 kN/m^3 . For filling the sand tank with dry density 17.1 kN/m^3 the above procedure is kept the same but, the number of hammer drops have been decreased to be 8 drops.

3.1.7 Cases of Study

With reference to Fig. 5 the flow chart, as well as Table 2 and Fig. 11 below the cases of study are presented. However, two rigid steel plates have been tested. The dimensions of the first plate are 6.0 cm by 9.0 cm . The second plate dimensions are 6.0 cm by 12.0 cm , i.e. the plates breadth kept constant. They introduced five cases of studies, depends on the variation of relative eccentricity “ r ” and dry density.

Table 2. Physical model cases of study

Plate dimensions	$B = 6.0 \text{ cm}$ and $L = 9.0 \text{ cm}$		$B = 6.0 \text{ & } L = 12.0 \text{ cm}$	
Dry density	17.1 kN/m^3			18.4 kN/m^3
Relative eccentricity	$r = 0.00$	$r = 0.17$	$r = 0.18$	$r = 0.00$
Case study number	(3)	(4)	(5)	(1)
Figure number	Figs. 12	Fig. 13	Fig. 13	Fig. 12

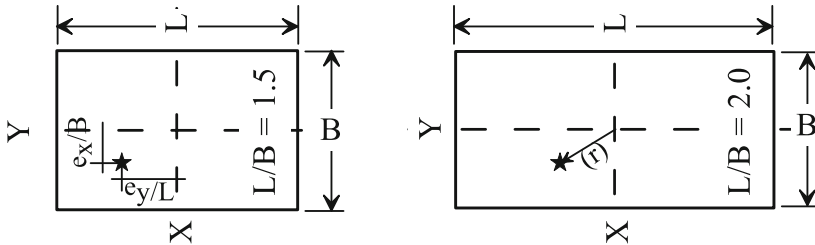


Fig. 11. Tested plate relative eccentricities and aspect ratio

3.1.8 Cases of study (1) and (3)

The main objective of these two tests is to measure the modulus of elasticity of the foundation soil inside the sand tank at the dry density of 18.4 kN/m^3 ($Dr = 0.77$) and 17.1 kN/m^3 ($Dr = 0.29$). Each plate has been loaded concentrically, i.e. $r = 0.00$ and the

applied stresses has been measured based on the proving ring, Fig. 10, as well as the plate area. The corresponding settlement of plate center with respect to each load increment has been reported. Due to the concentric loading conditions, the settlement of the plate center is the average settlements of its corners, because the plate is rigid. Then, two stress strain curves have been plotted in Fig. 12, the strain was calculated as the settlement divided by 1.5 B. As the plate's breadth is the same, the influenced zone is constant and both curves could be served by the same Y-Axis. Curve "A" presents case (1) while "B" presents case (3). The two curves have been fitted as two straight lines, the dashed lines, and then the inverse of the straight line slope presents the modulus of elasticity per each density. It is obvious from Fig. 12 that the measured curves are very close to the fitted lines, the regression factor is 0.99.

The following notes are concluded based on Fig. 12:

1. At relative density $Dr = 0.77$ the Modulus of elasticity is 87720 kN/m^2 . These are compatible with the upper limit of Medium density sand status.
2. At relative density $Dr = 0.29$ the Modulus of elasticity is 26040 kN/m^2 . These are compatible with the lower limit of Medium density sand status.
3. The dramatically losses of Modulus of elasticity and relative density is huge even though, the reduction of compaction energy during filling the sand tank seems small. It means the accuracy of the filling process is very sensitive.
4. Consistency of results gives confidence in model representativity.

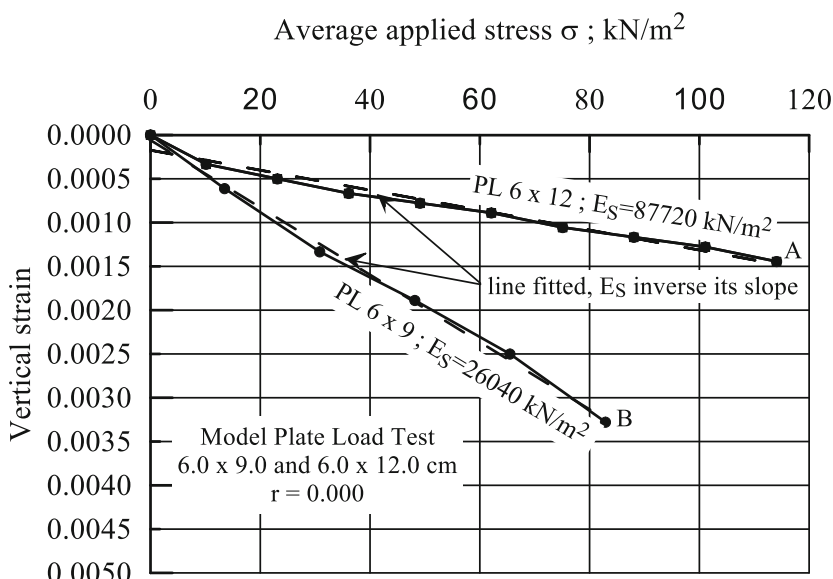


Fig. 12. Modulus of elasticity of the tested soils

3.1.9 Cases of Study (1)-(2)-(3)-(4)-(5)

As shown in Table 2 as well as Fig. 11, cases (1) and (2) represent the rigid plate of 6.0 by 12.0-cm rests on sand its modulus of elasticity is 87720 kN/m^2 and its dry density is 18.4 kN/m^3 . While cases (3) to (5) stand for a rigid plate of 6.0 by 9.0-cm rests on sand its modulus of elasticity is 26040 kN/m^2 and its dry density is 17.1 kN/m^3 . These choices covered different aspect ratios having the same plate width and also cover the case of medium dense sand by considering its borders.

Throughout case (1), the 6% 12-cm plate is loaded concentrically, i.e. the relative eccentricity $r = 0.000$, Fig. 13-A. Case (2) is the same as case (1) but the loading pin is shifted to apply bi-axial load with a relative eccentricity $r = 0.187$, Fig. 13-C. From case (3) to (5), the technique is the same, Fig. 13-B is concentric loading of $r = 0.000$, whiles Fig. 13-D and 13-F present the loading of the 6% 9-cm plate by different relative eccentricities, i.e. $r = 0.170$ and 0.180 respectively.

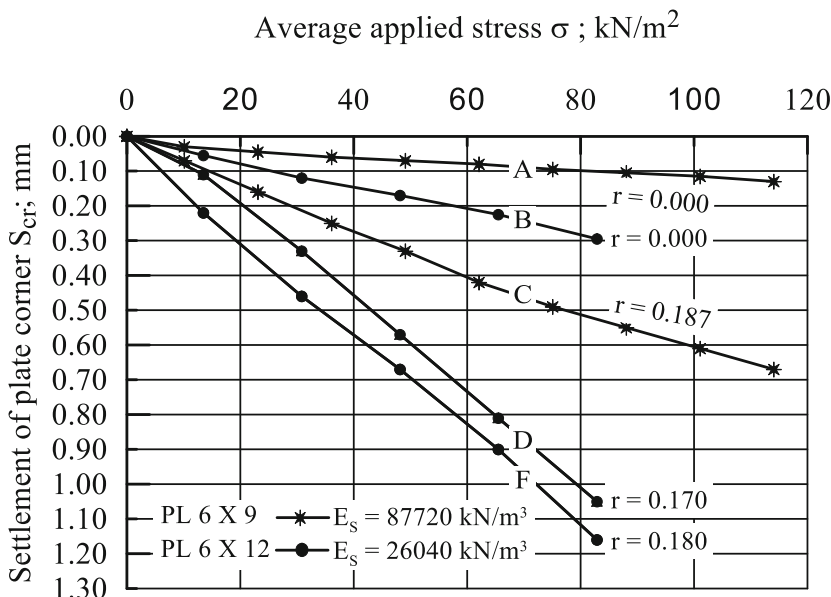


Fig. 13. Review of the physical model results

Based on Fig. 13, the following notes have been carefully abstracted:

1. All curves are straight lines, this is due to low stress level normally used in physical models, for that it is used for behavior explanation rather than measuring values. Accordingly, wind tunnel simulators were developed.
2. Comparing curve A with B or C with F, as E_s increases the settlement of the plate center or corner decreases, it is expected and shows the model trust.
3. The value of $r = 0.187$ presents eccentricity $e \approx B/6$, there the settlement of the corner is about 5 to 6 times the settlement of the center even though the stress level is modest, i.e. $\approx 80:100 \text{ kN/m}^2$, and the sand is dense.

4. The effect of the applied stresses value on the induced settlement dramatically increases with the increases of relative eccentricity. Accordingly, the eccentricities in high rise building should be avoided.
5. Comparing curve F with D, shows they are parallel, means the concept of relative eccentricity “r” is a locus of a circle makes sense, see Eq. (2).
6. Comparing curves A with C and B with F shows that there is a possibility of predicting the settlement of the plate corner based on the previous knowledge of the plate center settlement that concentrically loaded as it is mentioned earlier, subtitle Khater method.
7. The above note “6” needs intensive model tests based on more advanced model techniques, this advice to be further research work.

3.2 Field Work: In-Situ Plate Load Tests

This field experimental work is a continuation to the physical model. Simply, it is a group of in-situ plate load tests. The main target of these tests is loading plates having bigger dimensions rather than plates tested within the physical model scope of work. Moreover, to subject the tested plates to higher stress levels. Furthermore field results, generally, give more confidence and assure the obtained results of physical or theoretical models. This field investigation is limited but illustrative.

The field investigation consists of five plate load tests with different plate shapes and aspect ratios. They have been loaded concentrically and eccentrically. As shown in Fig. 5 the flow chart, a circular plate of 45 cm in diameter has been used, theoretically speaking $L/B = 1.0$ and loaded concentrically, $r = 0.000$ and only. A rectangular plate it's aspect ratio $L/B = 1.5$ has been tested eccentrically twice, first with $r = 0.117$ then $r = 0.171$. Furthermore another rectangular plate it's $L/B = 2.0$ has been tested eccentrically twice too, first $r = 0.117$ then $r = 0.191$, throughout the studied cases the plate breadth is 0.24 cm and kept constant, the thickness is 20-mm.

Table 3. In-situ plate load test

L/B	1.0	1.50	2.0
Plate dimensions	$D = 0.45\text{ m}$	$B = 0.24 \& L = 0.36\text{ m}$	$B = 0.24 \& L = 0.48\text{ m}$
Relative eccentricity	$r = 0.000$	$r = 0.117$	$r = 0.171$
Case study number	(6)	(7)	(8)
Figure number	Fig. 13 and 14	Fig. 18	Fig. 18

Table 3 summarized the in-situ plate load five cases of study. However, the previously mention Figs. 5 and 11 as well as Table 3 give all the needed data and parameters that will be explained in the following sub-titles.

3.2.1 Plate Load Test: Case (6)

The tested soil is well compacted mixture of sand – gravel engineering backfill, 1: 1 has unknown mechanical properties. Accordingly, this case of study has been performed to predict the compacted backfill modulus of elasticity, E_S . A circular rigid steel plate its diameter is 0.45-m has been used to perform the tests. The plate has been loaded concentrically, i.e. $r = 0.000$ by calibrated hydraulic jack. The stress and the

corresponding settlement with every load increment have been reported. Then the effective compressed zone is assumed to be $1.5 B$, i.e. 0.675-m is used to calculate the strain as the settlement divided by $1.5B$. Then, Fig. 14 drafted and the modulus of elasticity E_S calculated and found to be 185185 kN/m^2 . This value of E_S stands for very dense sand. Figure 15 presents load settlement curve while drafted on log-scale to predict the ultimate bearing capacity that found to be 370 kN/m^2 .

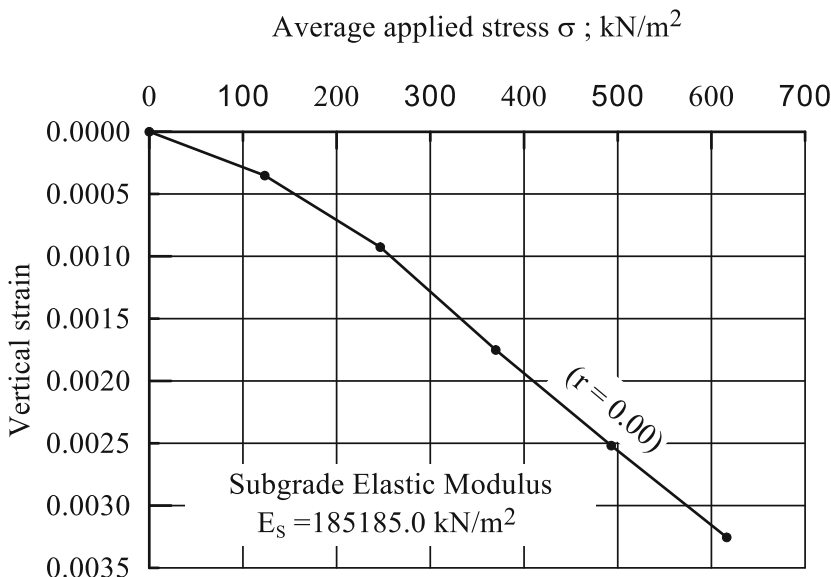


Fig. 14. Elastic modulus from plate loading test; E_S

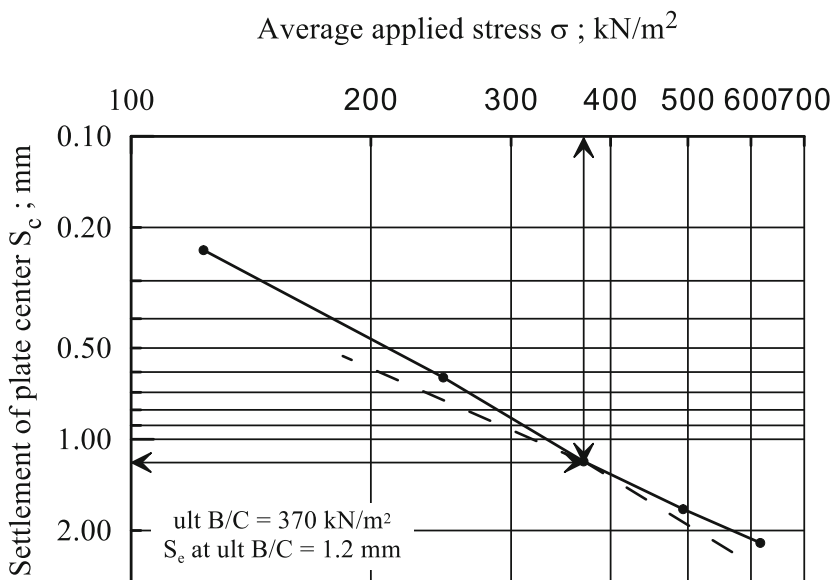


Fig. 15. Ultimate bearing capacity of the tested soil

3.2.2 Eccentric Plate Load Test: Test Arrangement and Preparation

The well known plate load test with its equipment's and preparation is the one that used here in, ASTM D1196/d1196 M-12(2016). The only modification that added to perform in-situ eccentric loading conditions is as follows; Figs. 16, 17 and 18.

1. The tested plate is marked in a shape of a bowl 5-mm depth, "a".
2. This mark presents a specific eccentricity, e_x and e_y .
3. A square rigid plate glued to the base of the test Jack, it has central mark same and identical as "a" mentioned above.
4. The Jack rests on the square plate and both rest on 15-mm steel ball "b" which in turn partially sink inside the bowl mark "a".
5. The above arrangement simulates the case of eccentrically loaded plate.
6. As the Jack lightly pushed up against the counter weight the Jack and system of plates that mentioned above, item 4, became stable then the test could start.

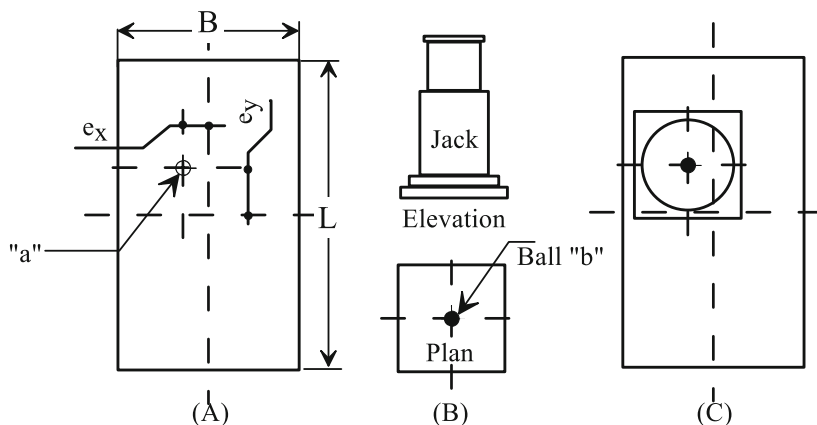


Fig. 16. Plate load test arrangement and preparation



a. Ball & plate

b. Perspective

Fig. 17. Plate, ball and eccentricity arrangement

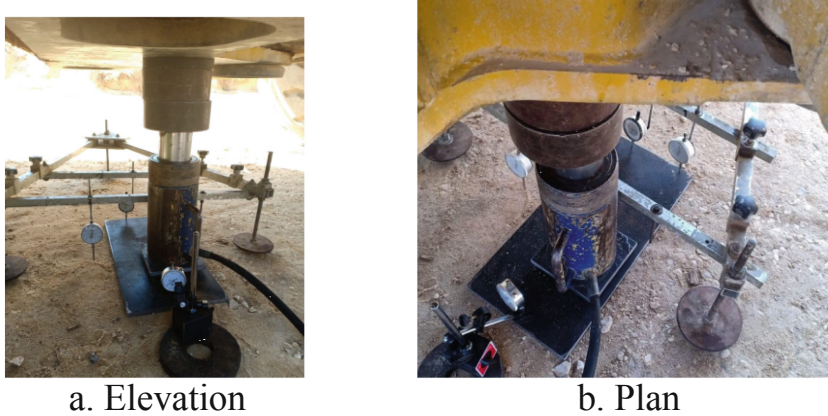


Fig. 18. In-situ eccentrically plate loading test

3.2.3 Plate Load Test: Case (7) and (8)

Those two cases present rectangular plate its dimensions are $0.24 \times 0.36\text{-m}$ and aspect ratio $L/B = 1.50$. Two bi-axial eccentricities have been investigated, numerically they are $r = 0.117$ and $r = 0.171$, as shown in Fig. 19. Only the settlement of the plate corner has been measured because it was not possible to measure the settlement of plate center due to the large diameter of the Jack, Fig. 18.

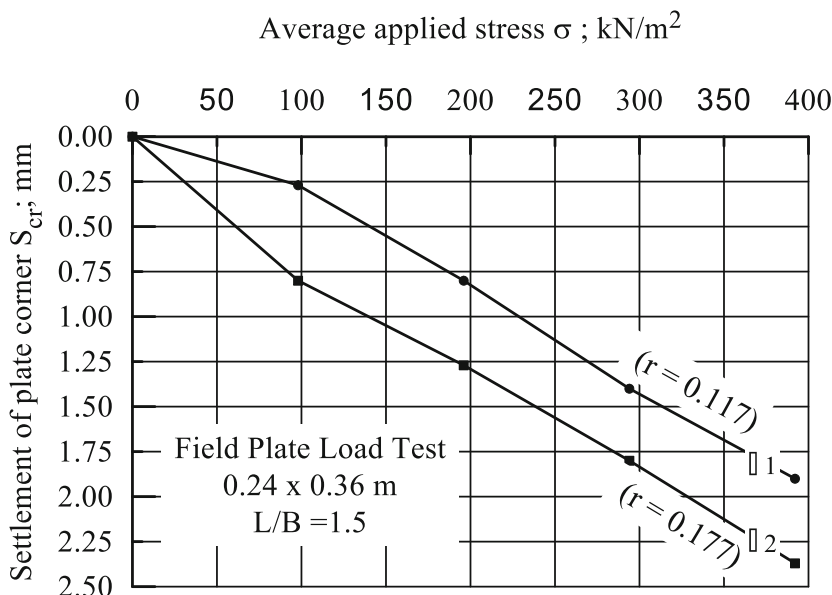


Fig. 19. Field plate load test $24 \times 36\text{ cm}$

The trend of the two curves ω_1 and ω_2 is identically the trend of the two curves D and F Fig. 13. The two curves of ω 's are parallel and if "r" increases by 50% the corner settlement increases by 65%, i.e. roughly the same percent.

3.2.4 Plate Load Test: Case (9) and (10)

Those two cases present rectangular plate its dimensions are $0.24 \times 0.48\text{-m}$ and aspect ratio $L/B = 2.00$. Two bi-axial eccentricities have been investigated, numerically they are $r = 0.117$ and $r = 0.191$, as shown in Fig. 20. Only the settlement of the plate corner has been measured because it was not possible to measure the settlement of plate center due to the Jack large diameter, Fig. 18.

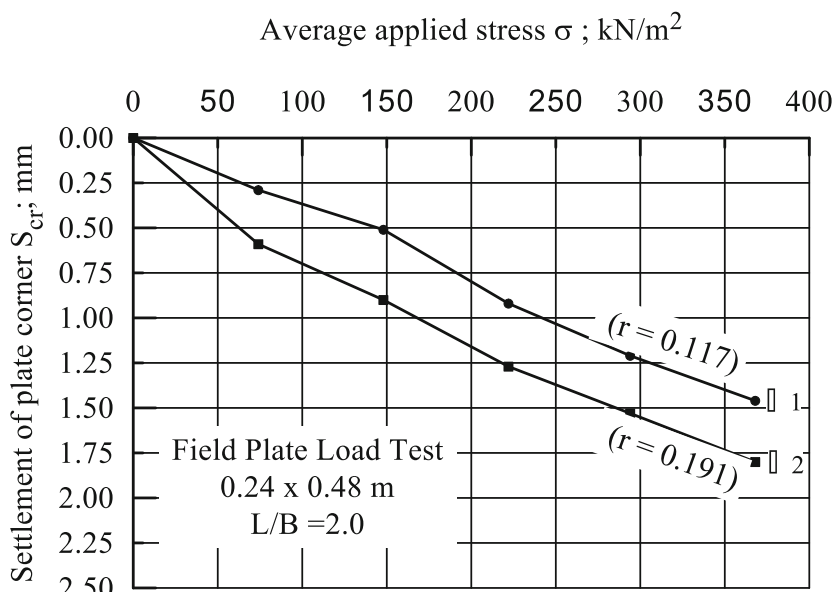


Fig. 20. Field plate load test $24 \times 48\text{ cm}$

The trend of the two curves ω_1 and ω_2 is identically the trend of the two curves D and F Fig. 12. The two curves of ω 's are parallel and if "r" increases by 60% the corner settlement increases by 70%, i.e. approximately the same percent.

4 Conclusions

This division presents the summing up of the research findings. It has been divided into four subtitles. It starts by the findings due to the numerical part, and then the finding obtained from the experimental investigation. The general findings have been gathered in a separate subtitle. Lastly, this division has been ended up by the further, suggested and needed research work in topic.

4.1 Numerical Part Conclusions

1. The main conclusion of this work is a novel simplified conventional method for predicting settlement of rigid plate center and corner, where the plate is bi-axially loaded and the predicted settlement is first approximation.
2. The method is valid for every plate has at least one axis of symmetry regardless the plate shape or its aspect ratios, i.e. general.
3. The approximation decreases to its minimum possible value, if the plate is circular, square or rectangular shape with breadth to length ratio L/B [2.0.]
4. It is valid for sandy soil with any density or elastic properties, i.e. general.
5. The method procedures and steps are reported within the subtitle “Presentation of the results: Khater method”, together with Fig. 4, Eqs. 5 and 6. Also, numerical example is given there, no need to repeat again here.
6. This method could be serve any case of shallow foundation its loads could be broken down to be vertical bi-axial load. Unsymmetrically loaded raft or isolated footing concentrically loaded and subjected also to moment are two examples. Let alone, involving the seismic effect or wind loads.

4.2 Experimental Part Conclusions

7. The most difficult part of the experimental modeling is the filling of the sand tank to form a soil mass has pre determine specific homogeneous dry density. It is an experience created, developed and improved during the course of the work. It is advised to run few fake tests before the research work to build up that personal non-written or reported experience, so far.
8. The most sensitive part of filling the sand tank process is the number of blows used during the compaction of each layer. The decrease of number of blows from 11 to 8 decreases the Dr from 0.77 to be 0.29.
9. Due to the low stress level used by the model, the soil behaves as an elastic material as all its activities lies in the early beginning of the stress strain curve, regardless of the value of Dr or the dimensions of the tested plate.
10. The measured Modulus of elasticity at $Dr = 0.77$ is 87720 kN/m^2 , while its value at $Dr = 0.29$ is 26040 kN/m^2 . The consistency of results is good and also matches the typical values of the borders of medium dense sand.
11. At $r = 0.187$ the eccentricity $e \approx B/6$, there the settlement of the corner is about 5 to 6 times the settlement of the center even though the stress level is modest, i.e. $\approx 80: 100 \text{ kN/m}^2$, and the sand is dense. Accordingly, the eccentricities in high rise building should be avoided.
12. The model results shows there is a possibility to predict the settlement of the plate corner based on the previous knowledge of the plate center settlement that concentrically loaded as it is mansion earlier, subtitle Khater method.
13. The suggested preparation for performing in-situ eccentric plate load test shows great function ability and it is recommended.

4.3 General Conclusions

14. Reconstituted sample components are given in Table 1. It presents a well graded sand SW having $C_c = 1.81$, $C_u = 6.21$, denoted Fayoum sand. It is given to be used in other research work as it is.
15. The reconstituted sample properties are; $\sigma_{d\text{-max}} = 19.1 \text{ kN/m}^3$, $\sigma_{d\text{-min}} = 16.4 \text{ kN/m}^3$, O.M.C = 8.3%, $G_s = 2.66$, $\phi = 36.7^\circ$, $\varphi_{\text{repose}} = 29.5^\circ$.
16. For physical models that apply vertical point load, home-made proving ring, mechanical type Jack and mechanical dial gauges techniques as the one shown in Fig. 9 is simple, accurate, economical and recommended.
17. A proving ring of spring steel have outer, inner diameter of 190 and 180 mm respectively, ring thickness 10-mm and breadth 15-mm could transfer working load up to 125 kN undamaged.
18. Celebrating proving ring by using sensitive digital balance as it is fixed to the model frame with all its connections on is the best technique.
19. It was not possible to measure the settlement of the center of small size plates, and the average of its corner settlements was taken instead.
20. It was not possible to measure the settlement of the center of the plates when eccentrically loaded during the in-situ test the Jack diameter is huge.

4.4 Remarks About Ordinary in-Situ Plate Load Test

21. The tested back fill was performed very dense its modulus of elasticity is huge, i.e. 185185 kN/m^2 , also the plate of 45.0 cm diameter ultimate bearing capacity is high, i.e. 370 kN/m^2 .
22. With reference to Fig. 14, the stress strain curve it is not the textbook typical curve used to be drawn to present the general shear failure of dense sand. The one shown in Fig. 14 is more real and suits the case of plate load test.
23. The concept of the effective zone of stress is $1.5 B$ is fine with calculating the strain to draw the plate load tests stress strain curve, it is conservative.
24. Fig. 15 proves clearly, that the method of re-draw the stress-settlement curve on log scale is correct and accurate for the case of predicting ultimate bearing capacity for sand bed in general. Needs expert eyes to read the breaking point for cases of moderate density. But when it is used to evaluate a soil replacement, it should be dense or rejected. Therefore, the evaluation must be, is there is a breaking point or not.
25. It is recommended from our side to add comment number 25 to the codes.

Personal Opinion: For numerical analysis of foundations rests on dense sand and the applied stress level is moderate the Mohr-Coulomb soil model is adequate. In other words, more sophisticated soil model should be used for researchs rather than design purposes, even it could be more conservative or more costly, my opinion.

Further Research Work

It is advised to perform more advanced laboratory physical model to verify the accuracy of the suggested method. It is believed that advanced model should be capable

to apply high stress levels. The method of filling the sand tank should take more attention as a point of research, itself, and codes must standardize it. The use of in-situ plate load test as a soil replacement evaluation test needs more investigation and standardization in local codes. More unsymmetrical foundation shapes need to be investigated such as trapezoidal, L-Shape or un-equal wings U-Shape and etc.

Acknowledgments. The authors present their deep gratitude to Prof. Dr. Ahmed El Lathy, Dr. Hamdy El Lathy, Dr. Waled Hammad and Dr. Mohamad Morad for their valuable comments during the review of manuscript. Also, the appreciations should be extended to Eng. Nahla El-Sirsy HBRC, Eng. Ahmad Ramadan, and the group of the graduation project 2019: Eng.'s Islam M., Amer S., Kareem T. and Kareem M. for their assistance during the experimental investigation.

References

- Algin, H.M.: Elastic settlement under eccentrically loaded rectangular on sand deposit. *J. Geotechn. Geo-environmental Eng. ASCE* **135**, 1499–1508 (2009)
- ASTM (2014): American Society for Testing and Materials, Annual Book of ASTM Standards
- Borowicka, H.: Influence of rigidity of a circular foundation slab on the distribution of pressures over the contact surface. *Proc. 1st Int. Conf. Soil Mech. Found. Eng.* **2**, 144–149 (1936)
- Braim, K.S., Ahmad, S.N., Rashid, A.S., Mohammad, H.: Strip footing settlement on sandy soil due to eccentricity load. *Int. J. GEOMATE.* **11**(27), 2741–2746 (2016)
- Enkhtur, O., Nguyen, T.D., Kim, J.M., Kim, S.R.: Evaluation of the settlement influence factor of shallow foundation by numerical analyses. *KSCE Journal of Civil Engineering*, Springer. **17** (1), 85–95 (2013)
- Fadum, R.E.: Influence values for estimating stresses in elastic foundations. In: Proceeding 2nd International Conference SMFS, Rotterdam, vol. 3, pp. 77–84 (1948)
- Kaya, N., Ornek, M.: Experimental and numerical studies of T-shape footings. *Acta Geotechnica Solvenica* **1**, 43–58 (2013)
- Khater, Kh., Abouzied, M.: Conventional method to estimate settlement of plate subjected to bi-axial loading – Part I. Paper ID: 296. GeoSt.John's 2019. The 72nd Canadian Geotechnical Conference. Newfoundland and Labrador, Canada (2019)
- Lutenegger, A.J., DeGroot, D.J.: Settlement of Shallow Foundation on Granular Soils. Report of Research Conducted for Massachusetts Highway Department. University of Massachusetts, Boston (1995)
- Mayne, P.W., Poulos, H.G.: Approximate displacement influence factors for elastic shallow foundations. *J. Geotech. Geo-environ. Eng. ASCE.* **125**(6), 453–460 (1999)
- Nandakumaran, P., Senathipathl, K.: Settlement and tilt of footings under eccentric loads. In: 1st International Conference on Recent Advances in Geotechnical Earthquake Engineering and Soil Dynamics, pp. 737–740, St. Louis. Missouri (1981)
- Patra, C.R., Behera, R.N., Sivakugan, N., Das, B.M.: Estimation of average settlement of shallow strip foundation on granular soil under eccentric loading. *Tech. Note. Int. J. Geotech. Eng.* **7** (2), 218–222 (2013). W.S. Maney & Ltd
- Salimath, R.S., Pender, M.J.: Moment Capacity of Shallow Foundation on Clay Under Fixed Vertical Load. 2014 NZSEE, vol. P28, pp. 1–8. Aoles Center, Auckland (2014)
- Zedzn, A.J., Maulood, H.J.: Pressure-settlement characteristics of shallow foundation using finite element method. *Tikrit J. Eng. Sci., TJES* **24**(1), 25–37 (2017)



Numerical Prediction of Thermo-Mechanical Behavior of Energy Pile in Pyroclastic Soil

Gianpiero Russo^(✉), Gabriella Marone, Luca Di Girolamo,
and Marianna Pirone

University of Napoli Federico II, Naples, Italy
{pierusso, gabriella.marone, luca.digirolamo,
marianna.pirone}@unina.it}

Abstract. The use of the ground as heat source or heat sink to manage the thermal loads within buildings through foundation is a well-established technology known as Energy Geostructures (EGS). The application of heat exchange via piles foundation known as Energy Piles (EP) are becoming increasingly popular in many European countries in the last few years. Field scale and small-scale laboratory tests represent a useful tool to get an insight in the mechanism governing pile-soil interaction under thermo-mechanical loading. In situ testing provides more realistic thermo-hydro-mechanical behavior of piles but is costly and time consuming. For these reasons laboratory small scale tests are often preferred. In such a case known stress-strain histories and controlled boundary conditions are more easily obtained. In this paper, class A predictions of small-scale laboratory tests are presented and discussed. The predictions are based on fully coupled thermo-mechanical 2D FEM simulations; these refer to a prototype cubical box made of PMMA designed to minimize boundary effects. The EP is embedded in a continuous homogeneous layer of a pyroclastic sandy soil and equipped with heat exchange pipes with circulating heat carrier fluid. Heating and cooling cycles are simulated under operational head axial load. The results of the numerical simulations are used for a proper design of the physical modeling that will be set up at laboratory and for calibration of the sensors to be installed.

1 Introduction

The thermo-mechanical interaction between pile foundation and soil has been largely investigated through various approaches: in situ testing, physical modelling and numerical analyses. However, several studies in literature provide the results of experimental tests, both at field and small scale, where often the thermal loads applied do not account for a realistic thermal demand of the upper structure.

Several laboratory tests at 1 g allow studying the effect on interaction between a small-scale pile and surrounding soil under thermo-mechanical loadings. For instance, Kalantidou et al. (2012) performed four thermo-mechanical tests on a closed-end aluminum pile in dry Fontainebleau sand. Axial loads in each test amounted to: 0%, 38%, 76%, and 95% of the estimated soil-pile bearing capacity. Two thermal cycles were applied during each test varying the temperature between 25 °C and 50 °C. Pile head

displacement versus the imposed temperature was monitored. Under loads greater than 40% of the pile final resistance, irreversible settlement was observed after the thermal cycles. Yavari et al. (2014) presented laboratory scale test, similar to that presented by Kalantidou et al. (2012), but varying the pile temperature between 5 °C and 30 °C. Seven tests, with axial load ranging from 0 to 70% of the pile estimated bearing capacity, were performed. The curves of pile head displacement–pile temperature changes, under nil axial load, show a perfectly thermo-elastic behavior while once a load began to be applied at the pile head, irreversible settlement began to appear. Wang et al. (2017) carried out thermo-mechanical tests on a small concrete pile in dry sand. Three different heat exchangers configurations, U-shaped, spiral and W-shaped, have been considered. Three heating and cooling cycles, at temperatures between 55 °C and 4 °C, were applied to the pile at a constant mechanical load equal to 50% of the ultimate pile-soil capacity. The displacement produced in each heating and cooling cycle decreased as the cycle increased. The settlement of a W-shaped heat exchanger pile was larger than other two piles reaching 0.56% of the pile diameter.

In Nguyen et al. (2017) small-scale tests on aluminum pile installed in dry Fontainebleau sand were presented. Thirty thermal cycles ranging between 21 °C and 19 °C were applied while the pile head load was maintained at 0, 20, 40 and 60% of the pile ultimate bearing capacity. The results confirm that the increment of irreversible settlement after 20 cycles becomes negligible for the cases of axial loads lower than 40% of the pile resistance. The irreversible settlement continues to increase after 20 cycles only when the pile head load is high (60% of the pile resistance).

Even if physical modeling allows further understanding on the behavior of heat exchanger piles under known stress-strain histories and controlled boundary conditions, field testing provides the most realistic solution to quantify stress and strain induced by the thermo-mechanical loads. Two main site investigations of EP have been leaded: the EPFL setup in Losanne (Laloui et al. 2006), and the Lambeth College setup in London (Bourne-Webb et al. 2009). Both studies have been used to characterize the main aspects of EP subjected to thermal and thermo-mechanical loadings (Amatyka et al. 2012). Many other studies had been carried out in the word: Akrouch et al. (2014) in Texas (USA), Murphy and McCARTNEY (2015) in Denver, Murphy et al. (2015) at the US Air Force Academy (USA), Mimouni and Laloui (2015) in Swiss, You et al. (2016) in Bejing, Faizal et al. (2016) in Melbourne, Santiago et al. (2016) in Valencia, Vasilescu et al. (2018) in Paris, Sutman et al. (2019) in Houston.

In the other hand, numerical analyses represent a powerful tool to investigate and predict the thermo-mechanical response of energy piles even after several cycles. Recently some studies about the numerical modelling of isolated pile and piles group with different level of complexity have been published. Numerical models have been used to reproduce field investigations of thermo-mechanical pile behavior (Yavari et al. 2013; Akrouch et al. 2014; Maiorano et al. 2019; Rui and Yin 2018), or results from small scale tests (Rotta Loria et al. 2015; Khodaparast et al. 2016; Russo et al. 2019), and to perform parametric analyses (Bodas Freitas et al. 2013; Saggù and Chakraborty 2014; Batini et al. 2015; Bourne-Webb et al. 2016; Rammal et al. 2018; Marone et al. 2018; Rammal et al. 2019; Marone et al. 2019; Maiorano et al. 2019).

In this study, CLASS A prediction of the thermo-mechanical behaviour of a small-scale aluminum pile embedded in pyroclastic sandy soil is reported. In particular

coupled thermo-mechanical modeling of the small-scale tests has been carried out by using the FEM software PLAXIS 2D. The numerical simulations reproduce the experimental tests in order to predict the magnitude of the stress, strains, and temperature that are going to establish into subsoil during the laboratory investigations.

The physical modeling that will be set up at laboratory consists of aluminum pile installed at the center of a transparent PMMA squared box filled by pyroclastic sandy soil. The design of laboratory test layout is similar to that presented by Kalantidou et al. (2012), Yavari et al. (2014) and Nguyen et al. (2017). As regard to thermal loads, a dynamic energy simulation of the thermal conditions typical of a building located in Naples (Italy) will be performed to compute the applied loadings by using ad hoc software.

In the following, first a brief description of small scale modelling that will be built at laboratory, the experimental tests to be performed and the pile and soil properties filling the box will be reported. Then, the paper will mainly deal with the numerical modeling of the small-scale investigations and the CLASS A numerical prediction of thermo-mechanical behavior of the single pile.

2 Design of the Physical Modelling

2.1 Description

The physical model, that is going to be setup at laboratory, consists of a small tubular aluminum pile to install in a container filled by pyroclastic sandy soil. After compacting a dry layer of 0.30 m, the pile will be inserted in the container box and then, by several steps, a layer of 0.40 m will be pluviated. The pile is a closed-ended aluminum tube with inner diameter of 0.027 m, outer diameter of 0.03 m and length of 0.40 m (slenderness ratio greater than 13). The material of the test pile is extrusion aluminum alloy EN AW-6060 characterized by an elastic modulus of 69000 MPa, a medium tensile strength of 120 MPa, a linear expansion coefficient of $24 \cdot 10^{-6} \mu\text{e K}^{-1}$ and a thermal conductivity of 200 W/m K. The test container has length, width and height respectively of 1.0 m, 1.0 m and 0.70 m. The walls of the experimental box are made of 20 mm thick PMMA while the base is made of steel.

According to Parkin and Lunne (1982), in order to minimize the boundary effects on pile behavior, the ratio between the diameter of the container and that of the pile should be 20 for loose sands and 50 for dense sands. Indeed, Kouby et al. (2014) suggested that the distance between the pile toe and base of the container should be greater than 10 times the pile diameter. Both the conditions are met in the described experimental setup. To increase the roughness of the aluminum pile, a coat of sand is stuck onto the pile shaft.

The displacements at the head of the pile will be measured by means of two LDVT transducers while the vertical strains along the shaft are measured by six electrical strain gauges. The latter ones are linear strain gauges of 6 mm length stuck to the pile shaft and covered by a protection that ensures the durability of the devices.

Five temperature gauges are placed in the soil in order to evaluate the variation of the temperature during the test. The details of the experimental set-up are presented in Fig. 1.

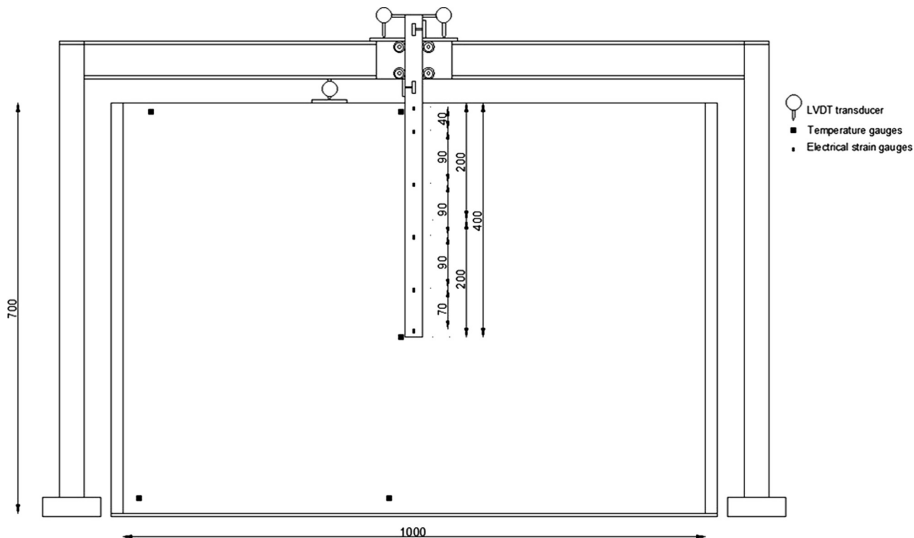


Fig. 1. Experimental set-up of the physical model.

2.2 Soil Physical and Mechanical Properties

The soil filling the container is a pyroclastic sandy soil collected from a site placed at north of Napoli. Physical and mechanical characterization was already carried out in a previous research (Raucci 2017). In particular, in situ tests including two boreholes, S1 and S2, grain size distribution, four CPTs, TXCID and 1D compression tests on undisturbed samples were carried out. A summary of the results of the tests performed by Raucci (2017) is reported below.

From both the boreholes and CPTs it was possible to identify the soil layering. In the first 5.50 m alternating pyroclastic silty sands and volcanic ashes were found. From 5.5 to 9 m grey tuff was detected overlying a sandy layer placed at 9 m up to 12 m. Below 12 m the grey tuff was again found. The cone resistance for the four CPTs are reported in Fig. 2. Durgunoglu and Mitchell (1975) and Robertson and Campanella (1983) methods provide a medium friction angle of 35° for the sand layer until 2.6 m depth. In situ Relative density D_R has been estimated about 44%, from the penetration tests, by means of Lancellotta (1983) and Baldi et al. (1986) methods. Young's and oedometric modulus have been computed by means of De Beer method (1965) considering that the soil is silty and fine sand.

From the samples collected at two different depths, three specimens were used to perform drained triaxial consolidated tests (CID). The three specimens from the S2-2 sample taken under the water table, were tested after a preliminary check of the initial full saturation.

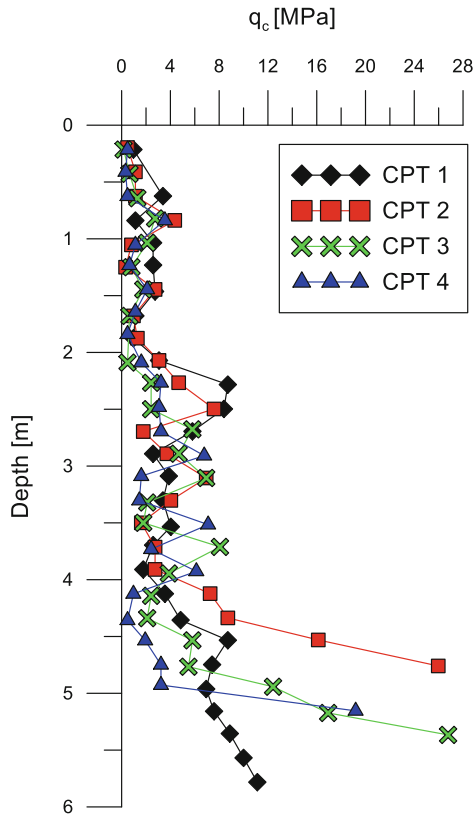


Fig. 2. CPTs test for Pascarola site from Raucci (2017).

Three CID tests have been carried out by applying different cell pressures: 50 kPa, 100 kPa and 200 kPa. Figure 3 shows the graphs of the stress path (a), deviatoric stress versus axial strain (b), deviatoric stress - mean effective stress ratio versus axial strain (c) and volumetric strain versus axial strain (d) obtained from the three tests. For each test, stress at peak and steady state have been detected and reported in Fig. 3(a) respectively in red and blue straight line. Critical state and peak friction angles are respectively 29.4° and 33.3° .

The sandy soil used for filling the model box via the pluviation system was collected from in-situ depth ranging between 2 m and 2.50 m. From the grain size distribution carried out on this sample, the median grain size, D_{50} , is 0.2 mm and the specific gravity is 2.56 g/cm³.

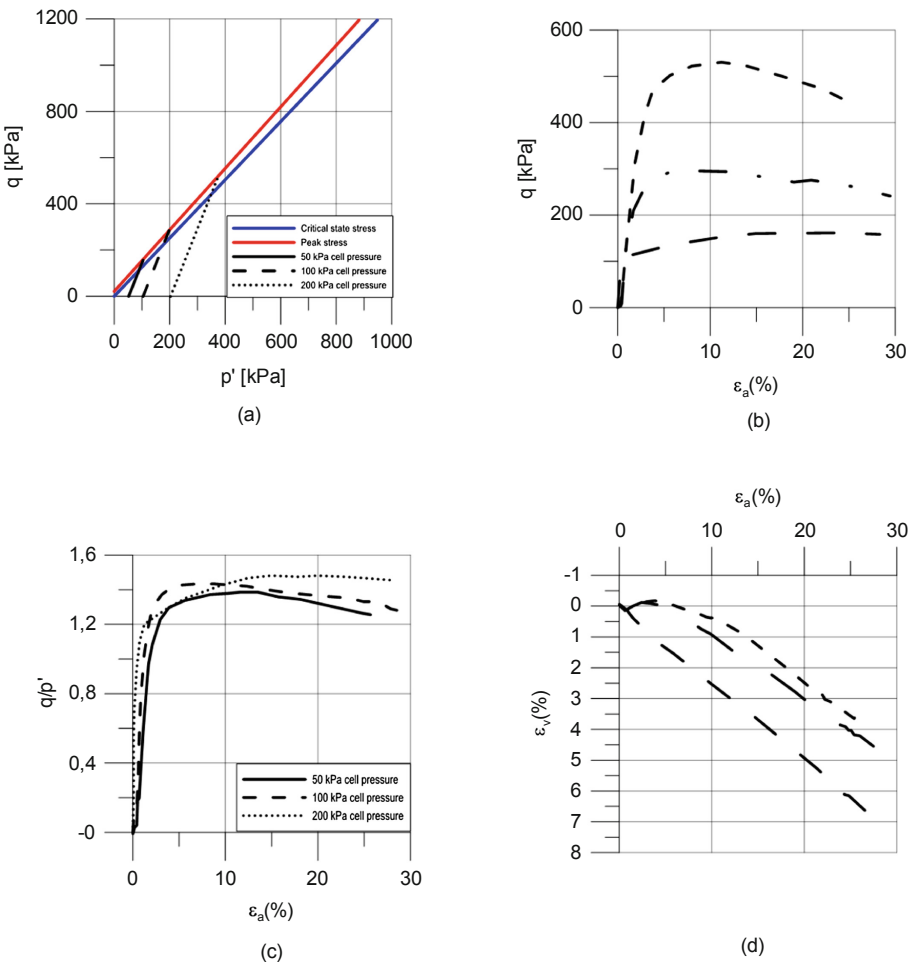


Fig. 3. Results of the triaxial tests on the s2-1 samples from Raucci (2017).

2.3 Plan of the Experimental Tests

Different kinds of test will be carried out to the aim of evaluating the effects of thermo-mechanical coupled loads on the soil-pile interaction: i. purely mechanical test, ii. purely thermal tests and iii. coupled thermo-mechanical tests.

Mechanical load will be applied by dead weights at the top of the pile. The aim of this test is to evaluate the behavior of the pile under conventional load and to obtain the load settlement curve and the bearing capacity of the soil-foundation system.

The thermal loads will be applied through circulating a heat carrier fluid into helical tube connected to temperature-controlled bath and a peristaltic pump. The real behavior of an energy foundation installed in the area of Naples under operational conditions will be simulated. In this regard, a mechanical load, corresponding to the 40% of the

estimated bearing capacity, will be applied at the head of the pile and is then combined with thermal cycles of heating and cooling. The thermal loadings to be applied on the physical modelling have been calculated through dynamic energy simulation of the thermal conditions typical of a building located in Naples (Italy) by using ad hoc software.

In fact EP thermal loads depend on climatic context where the building to be conditioned is located further to the building features in terms of air conditioning demand and solutions adopted for thermal isolation. Of course, the heating pump installed also plays a major role in defining the thermal exchange with the ground source (i.e. the pile). It is worth mentioning that a literature overview of field and laboratory tests on energy piles, shows that inlet temperature in pipes into piles could be very different and often there are not any details on the procedure adopted to determine it (Hamada et al. 2007; Pahud and Hubbuch 2007; Bourne-Webb et al. 2009; Park et al. 2013; Zarrella et al. 2013; Murphy and McCartney 2015; Luo et al. 2017). In the test to be carried on in the physical modelling, the thermal loads are evaluated considering a typical building in Napoli. As an additional information the air temperature values recorded in Naples in 2018 are shown in Fig. 4. This graph shows that cooling phases for building in summer season, corresponding to heating loads for the pile, are longer and with higher values magnitudes, respect to winter season. This is also confirmed by Morrone et al. (2014) that reports a ratio of about 2.5 between the energy needed to cool a building located in Napoli in the summer season and the energy required for heating it in the winter season.

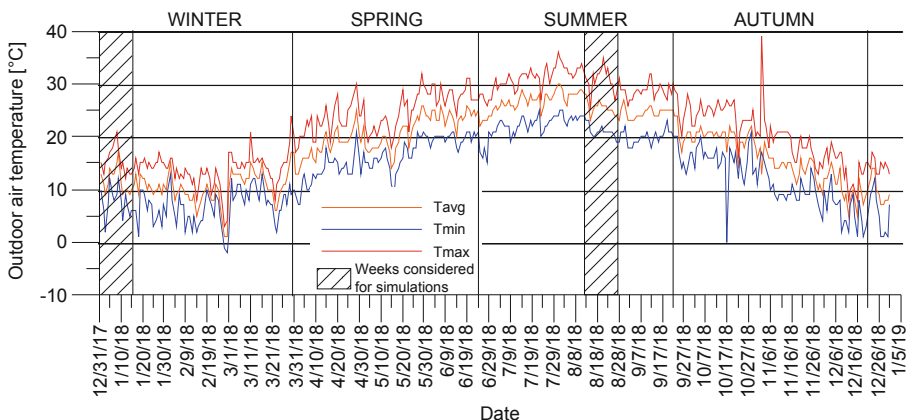


Fig. 4. Naples 2018 outdoor air temperature

2.3.1 Procedure to Derive the Thermal Loads

Magnitude of temperatures, number and duration of thermal cycles influence the thermo-mechanical behavior of EP. Thermal loads for the experimental small tests have been determined by dynamic energy simulations of an office building in Napoli by means of *Design Builder* software. It is an *Energy-Plus* based software tool that can

model building cooling, heating, lighting, ventilation and other energy flow. For the simulation, a hot and chilled water plant loops have been used, with the supply side of the heat pump connected to a ground heat exchanger.

To determine thermal loads of EP that will be used for the small-tests, temperature at supply side of geothermal heat pump has been considered at the end of the simulations. An annual simulation has been performed. However, the results on two weeks for each operational mode, heating and cooling, will be used to test the physical modeling at laboratory. The cycles of heating and cooling have been chosen in order to test the maximum thermal loads for both modes.

The plant used in the simulations, was modelled through the introduction of a Ground Sources Heat Pump (GSHP) water to water. Calculation of the peak thermal loads in Summer and Winter has been done to size the plant, its components, geothermal heat exchangers as well as the size and type of heat pumps.

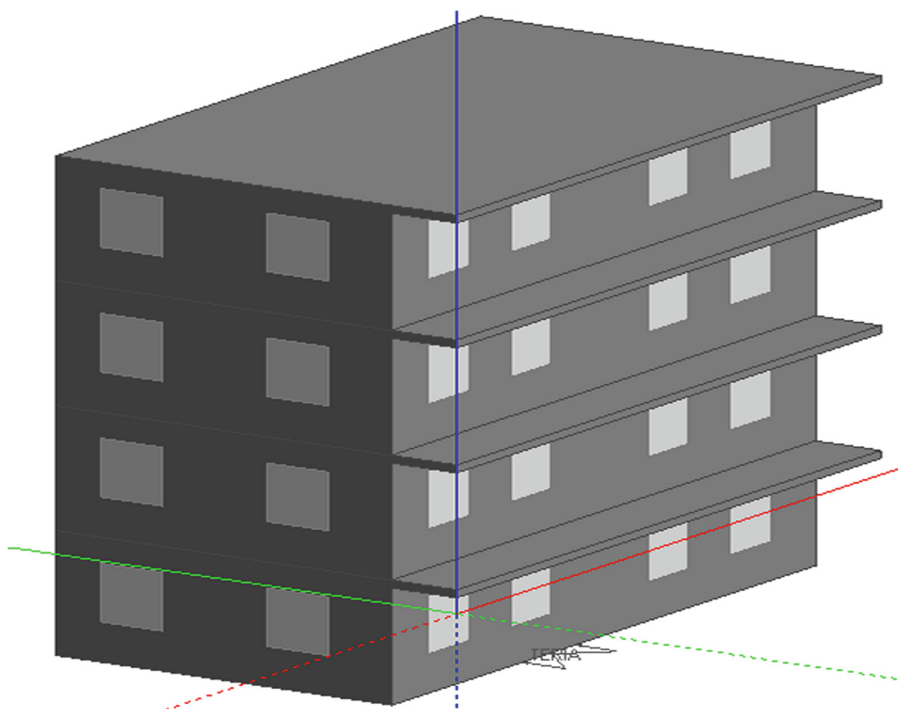


Fig. 5. 3D Model adopted for thermal analysis

The building used for the determination of the thermal loads is of rectangular shape of side $9.00\text{ m} \times 16.25\text{ m}$. The total building area is about 146 m^2 , composed by four stories all used for office use. The choice of the use destination is linked to a simpler determination of the hours of use of the structure and its plants. About the architectural/plant engineering part, the model was created assuming a new construction intervention and therefore taking into account regulatory features and the limit

parameters in terms of transmittance of the parts of the building envelope. The model adopted is shown in Fig. 5. Indeed, it has been assumed that each floor consists of a single Thermal Zone, i.e. a thermally homogeneous zone both for the activities carried out and for the minimum and maximum set point temperatures to be considered during the summer and winter seasons.

Modelled geothermal system is characterized by a primary circuit heat exchangers composed by 16 wells and a secondary circuit composed by radiant panel floors with maximum delivery temperatures of 35 °C and minimum of 12 °C. The indoor air set point temperatures have been established, according to UNI TS 11300 at 20 °C for the Winter season and 26 °C for the Summer season. From the simulation carried out, it was possible to determine the temperatures entering the underground collector, which in this case corresponds to the primary circuit in EP. The hourly results have been subsequently transformed into daily averages temperatures over the previously mentioned two weeks of operation (Fig. 6).

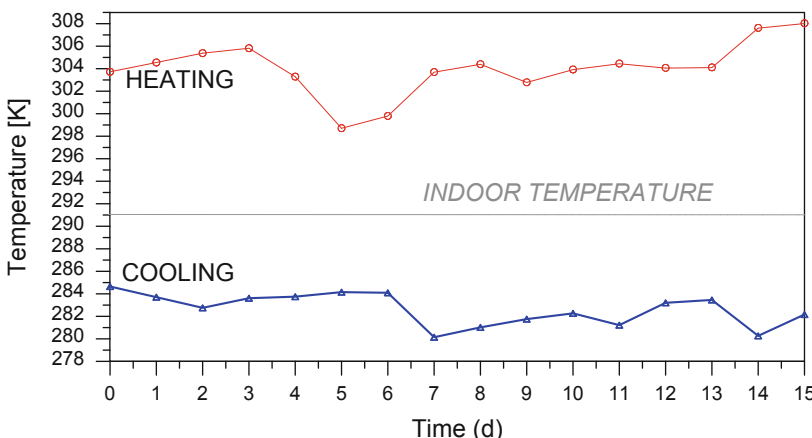


Fig. 6. Thermal cycles of heating (red line) and cooling (blue line) adopted in the numerical analyses.

3 Class a Prediction: Thermo-Mechanical Numerical Simulations

3.1 Geometry, Mesh, Material Properties

The numerical simulations have been carried out by means of FEM software, PLAXIS 2D, in order to predict the thermo-mechanical behavior of the aluminum pile installed in the physical modeling described in the previous sections. In particular thermo-mechanical coupled analyses in axisymmetric conditions have been performed. The axisymmetric option approximates the condition of the single pile in the square box by adopting an equivalent radius (Fig. 7). Triangular fine mesh of 15 nodes has been used to discretize the experimental model. Through defining the coarseness factor, the mesh around the pile was refined.

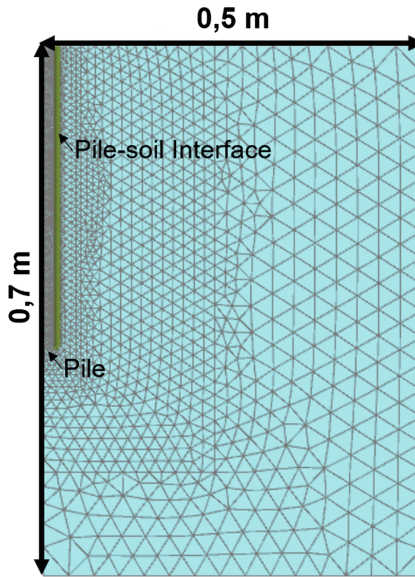


Fig. 7. Geometry and mesh of the numerical model

The soil has been modelled by an elasto-perfectly-plastic Mohr-Coulomb constitutive model, while the aluminum pile as an elastic material. For a proper modelling of soil-pile interaction an interface has been inserted to simulate the thin zone of large and concentrated shear strains. The friction angle at the interface was chosen equal to the that of the sand because the pile shaft was covered with a thin layer of sand. The stiffness and resistance of the soil are evaluated from the site and laboratory investigations reported in previous paragraph. The peak friction angle derived from the triaxial tests, 33° , and a dilatancy angle of 3° by considering the results of the tests and Bolton expression (1984) have been assumed. The stiffness of the soil, obtained from CPTs investigations, is scaled considering that the stress state in the container box is different to those found in situ. The average stress level at mid depth down the model aluminum is only about 2 kPa while in the situ at 1.25 m depth is about 10 kPa. Considering a value of porosity typical of pyroclastic soils in Campania region, equal to 0.65, the value of the dry weight of the unit volume is derived from the specific gravity and it is assumed equal to 8 kN/m^3 . The thermal conductivity of soil was assumed as 0.2 W/m/K common value for a dry sand with no high quartz content. The mechanical and thermal properties adopted in the FEM model are reported in the Table 1.

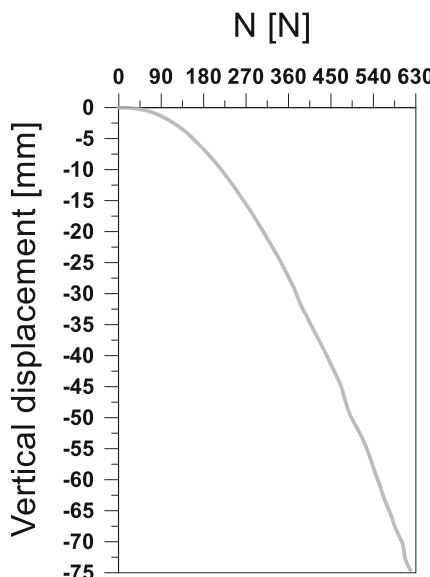
Table 1. Values of mechanical and thermal parameters used in the analyses.

Material	Friction angle Φ [°]	Dilatancy angle Ψ [°]	Elastic modulus [Mpa]	Heat conductivity λ [W/m K]	Specific heat capacity c_s [kJ/t K]
Pyroclastic sandy soil	33	3	1.69	0.2	800
Aluminum pipe	–	–	13000	200	900

3.2 Mechanical, Thermal and Thermo-Mechanical Tests Simulations

The same boundary conditions that will be tested on the physical modeling, have been applied to the numerical simulation in order to predict the axial load and displacements of the pile as response to thermo-mechanical loads.

The purely mechanical test is simulated considering two different phases that reproduce respectively the soil and pile installation and the loading phase. The initial phase, concerning the installation of the sand and the pile, is simply simulated by generating the initial stress field under K_0 evaluated as $1 - \text{sen}\phi$. Then the latter phase, executed as a plastic calculation, simulates the pile loading until failure. From this simulation, the pile bearing capacity was evaluated equal to 192 N. This value has been selected as corresponding to a settlement of the pile head equal to 25% of the pile diameter. The load-settlement curve obtained by the mechanical test simulation is reported in Fig. 8. From now so on, the compressive forces and upwards displacements are taken to be positive whereas the tensile forces and the downwards displacements

**Fig. 8.** Load-settlement curve obtained from numerical simulation by PLAXIS 2D.

are taken to be negative. The bearing capacity computed through the numerical simulation, comparable to the bearing capacity computed with the β method, has been used to define with an opportune safety factor the operational load of the pile. In this regard, a value of the axial load equal to 40% of the fixed bearing capacity has been kept in the thermo-mechanical analyses.

The aim of the thermal test is to reproduce the behavior of the pile only subjected to thermal loadings. The thermal tests are modelled considering two different phases. During the first phase the temperature of the soil is assumed equal to 18 °C, the average temperature of the groundwater in Naples. The same procedure adopted in the mechanical test is used to model the soil and pile installation. In the second phase, heating or cooling mode is simulated by applying the thermal loads of heating or cooling respectively. A fully coupled transient thermo-mechanical calculations of the problems is carried out. The time dependent effects of changes of temperature on stress and deformation are to be taken into account. During heating and cooling a set of thermal boundary conditions were imposed on the edges of the model. Temperature conditions are assigned at the bottom and at the side of the container allowing the heat exchange between the soil and the external environment (laboratory). Heat transfer coefficients are assigned at the boundaries accounting for the different thickness and thermal properties of the materials of tests box (PMMA and steel). At the ground surface a convection boundary condition is assigned in order to consider that the air temperature influences the temperature of the ground.

The heating and cooling thermal loadings are imposed as a temperature -time variable functions on a straight line inside the pile body roughly corresponding to the operational location of the primary circuit in the experimental tests. The heat exchanger, in both cases reproduces a coil-type primary circuit. The helix circuit has been shown to represent the configuration with a higher specific heat/extraction rejection rate (Fadejev et al. 2017) compared to single U shape pipes. This more efficient configuration when the pitch of the coil is very small can be simulated via a cylindric constant temperature surface (in the axisymmetric model a simple straight line) (Marone et al. 2019). The heat exchange in the numerical simulations does not account for the difference between inlet and outlet temperature of the fluid. This hypothesis remains acceptable because the magnitude of inlet and outlet temperatures differs typically only about 4 °C (Rammal et al. 2018).

In case of heating, the temperatures varies between 26 °C and 35 °C while during cooling mode the variation is between 6 °C and 11 °C (Fig. 6). The computed response of the pile under purely thermal cycles of heating and cooling is represented via the displacement of the head and the toe of the pile and the axial load along the shaft (Figs. 9 and 10). The axial load during heating is compressive while during cooling is tensile. From the displacement history reported in Fig. 9 it could be seen that the toe and the head of the pile movements confirm the trend of the pile to dilate or to contract respectively during heating and cooling. During the heating the head of the pile heaves while the toe settles, the opposite occurs during cooling. The displacement of the head of the pile during both the operational modes are very close to the theoretical value, equal to the temperature variation multiplied by the linear expansion coefficient and to the distance between the head of the pile and the null point. The maximum value of the displacement during heating and cooling is respectively about 0.11 mm and 0.08 mm.

The maximum axial compression induced by heating is about 14% of the operational load while the maximum tensile induced by cooling is about 6%. The maximum of the thermal axial load is achieved during heating and cooling respectively at a depth of 0.29 m and 0.26 m along pile shaft. The induced thermal axial load is very low in fact the calculated thermal displacements are very close to the theoretical ones, as consequence the restrained deformation is minimal and the behavior of the pile is close to “free column”.

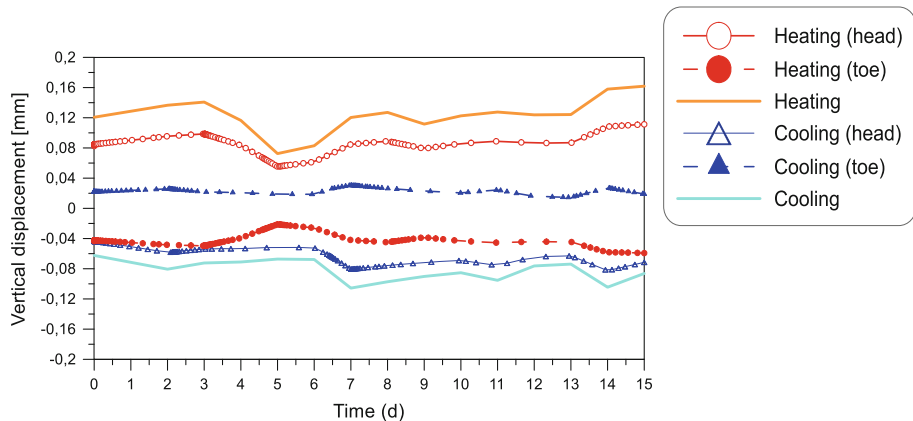


Fig. 9. Vertical displacement of the head (straight line) and the toe (dotted line) of the pile during heating (red line) and cooling cycle (blue line). Theoretical elongation of the pile during heating (orange line) and theoretical shortening of the pile during cooling (cyan line).

The thermo-mechanical simulations are carried out considering three steps. The first step corresponds to the first phase already described for mechanical and thermal tests. The second step is purely mechanical and pile's head is loaded in increments to the operational load (40% of the estimated bearing capacity). The third phase is thermo-mechanical. Fully coupled thermal analyses is carried out as in thermal tests but the thermal loadings of heating or cooling is imposed on pile by keeping the same live top load. Regarding the temperature conditions, in the first and second phases the temperature of the soil is assumed to be constant and equal to 18 °C. During the third phase, that is heating or cooling phase, a transient analyses is carried out. The set of thermal boundary conditions assigned in this phase correspond to those described for the purely thermal tests in the second phase.

The results of the thermo-mechanical tests are reported in terms of displacements of the head and the toe of the pile and axial load along the shaft of the pile. The axial load along the shaft is considered at the end of heating and cooling and they are reported, respectively, in red and blue continuous lines (Fig. 11). It is also reported the axial

induced thermal load during the heating and cooling phase when the thermal variations are maximum and minimum (respectively in red and blue dotted lines). The axial load along the shaft during both the operational modes is compared with the purely mechanical axial load (continuous black line Fig. 11). It can be noted that, respect to the purely mechanical case, heating corresponds to an increase of the load while for cooling the opposite occurs. However, at the end of cooling cycle, thermal axial load accumulates mostly at the toe. This is due to the typical cooling history applied to EP (Fig. 6b).

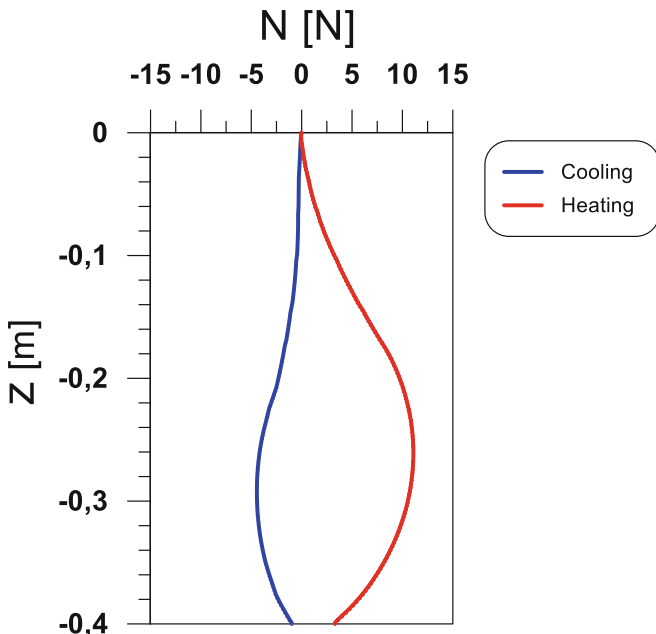


Fig. 10. Axial load induced by thermal loads along the pile shaft at the end of heating cycles (red line) and cooling cycles (blue line).

The displacements at the head and the toe of the pile follow the trend of the pile to dilatate and contract during heating and cooling respectively (Fig. 12).

The maximum values of total displacements of the head of the pile induced by thermo-mechanical loadings of heating and cooling are respectively 0.97 mm and 1.76 mm (Fig. 12).

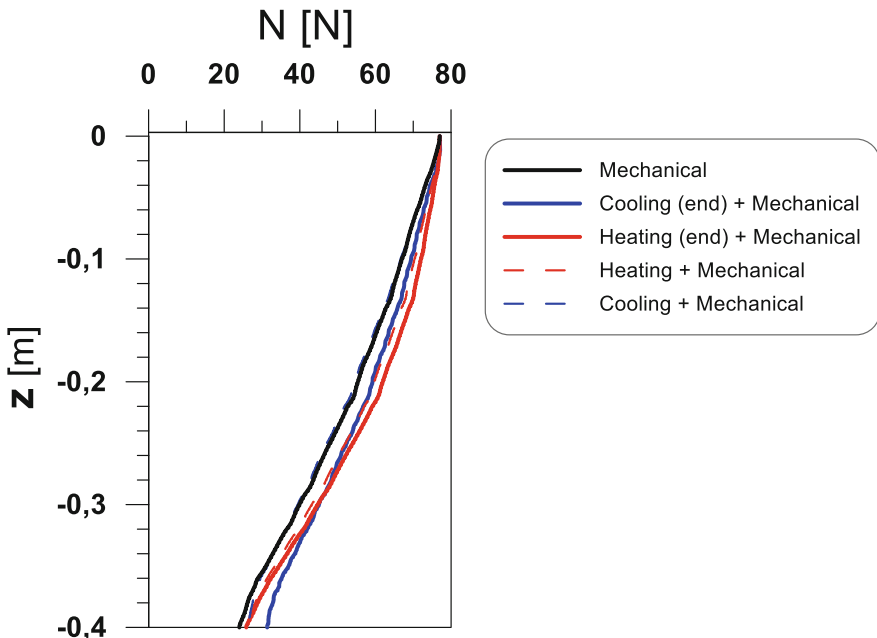


Fig. 11. Axial load along the pile shaft induced by operational mechanical load (black continuous line) compared with: axial load along the shaft induced by thermo-mechanical loads at the end (continuous red line) and during the heating cycle (dotted red line), at the end of the cooling cycles (continuous blue line) and during the cooling cycle (dotted blue line).

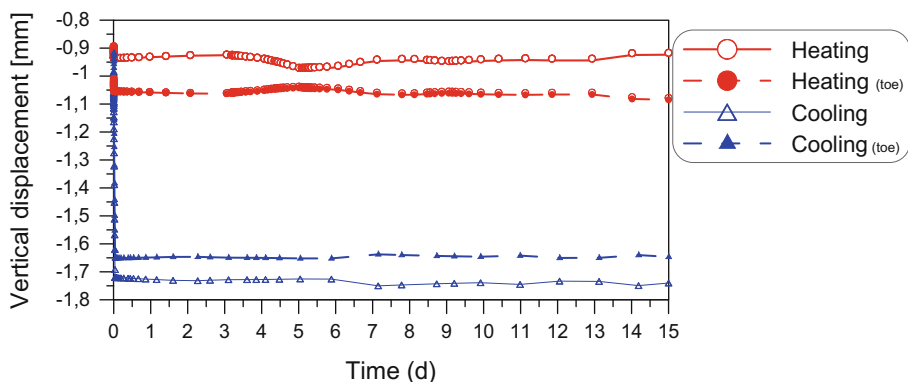


Fig. 12. Vertical displacement of the head (straight line) and the toe (dotted line) of the pile during heating (red line) and cooling cycle (blue line) combined with mechanical operational loads.

4 Conclusions

Numerical analyses have been carried out via the FEM code PLAXIS 2D to obtain CLASS A prediction of thermo-mechanical experiments at small-scale. Purely mechanical, thermal and coupled thermo-mechanical tests have been simulated. Thermal and mechanical loadings have been performed in order to reproduce potentially operational conditions of a single EP installed in the area of Napoli. Thermal loadings are evaluated via Design Builders software, modelling one year of thermodynamic simulation. For cooling and heating modes two weeks of operational conditions have been modelled. The effects of thermal and thermo-mechanical loadings on the soil-pile interaction have been evaluated in terms of displacements of the head and the toe of the pile and axial load along the shaft. The computed results show that the overall elongation of the pile embedded in the soil is very close to the theoretical value obtained on a free column with the height equal to the pile total length. The induced axial load along the pile shaft at the end of cooling and heating phases illustrate the complementarity of thermal deformation restraint and mobilized load change: larger pile head movements, closed to the theoretical values, are associated with lower internal load change (Bourne-Webb et al. 2019).

Axial load along the shaft obtained by thermo-mechanical tests of heating and cooling is compared to purely mechanical test. Heating and cooling combined to mechanical loadings determine respectively an increase or decrease of the axial load induced by purely mechanical loadings. However, at the end of cooling and heating cycles the trend of the axial load along the shaft shows that thermal load accumulates at the toe, particularly for cooling mode. The stress accumulation trend observed mostly in the case of cooling might be due to thermal history applied to the pile.

Lastly, the maximum displacements of the head pile due to the thermal load of heating and cooling are 0.65 lower and 10 times higher respectively than those calculated in absence of axial operational load (purely thermal simulations).

In fact, there is a clear coupling between mechanical and thermal loading even for this single free head pile. During the heating phase the mechanical loading acts as a constraint reducing the thermal induced movements while during cooling the opposite occurs. The effect of thermo mechanical coupling is noticeable and depends not only on the magnitude of mechanical loadings but also on thermal loadings type (cooling or heating).

References

- Adinolfi, M., Mauro, A., Maiorano, R.M.S., Massarotti, N., Aversa, S.: Thermo-mechanical behaviour of energy pile in underground railway construction site. In: Proceedings of 1st International Conference of Energy Geotechnics, Kiel, Germany, 29–31 August 2016 (2016). <https://doi.org/10.1201/b21938-15>
- Amatya, B.L., Soga, K., Bourne-Webb, P.J., Amis, T., Laloui, L.: Thermo-mechanical behaviour of energy piles. *Geotechnique* **62**(6), 503–519 (2012). <https://doi.org/10.1680/geot.10.p.116>. ISSN: 0016-8505

- Akrouch, G.A., Sanchez, M., Briaud, J.-L.: Thermo-mechanical behaviour of energy piles in high plasticity clays. *Acta Geotech.* **9**, 399–412 (2014)
- Baldi, G., Bellotti, R., Ghionna, V., Jamolkowski, M., Pasqualini, E.: Interpretation of CPT's and CPTU's. 2nd Part: drained penetration. In: Proceeding 4th International Geotechnical Seminar, Singapore, pp. 143–156. (1986)
- Bodas Freitas, T.M., Cruz Silva, F., Bourne-Webb, P.J.: The response of energy foundations under thermo-mechanical loading. In: Proceedings of the 19th International Conference on Soil Mechanics and Geotechnical Engineering, Paris (2013)
- Bolton M.D.: The strength and dilatancy of sands. Cambridge University Engineering Department (1984). ISSN: 1523–3812
- Bourne-Webb, P., Amatyka, B., Soga, K., Amis, T., Davidson, C., Payne, P.: Energy pile test at Lambeth College, London: geotechnical and thermodynamic aspects of pile response to heat cycles. *Geotechnique* **59**(3), 237–248 (2009). <https://doi.org/10.1680/geot.2009.59.3.237>
- Bourne-Webb, P.J., Soga, K., Amatyka, B.: A framework for understanding energy pile behaviour. *Geotech. Eng.* **166**(GE2), 170–177 (2013). <https://doi.org/10.1680/geng.10.00098>
- Bourne Webb, P.J., Bodas Freitas, T.M.: Freitas Assuncao R.M.: Soil-pile thermal interactions in energy foundations. *Geotechnique* **66**(2), 167–171 (2016). <https://doi.org/10.1680/jgeot.15.t.017>
- Bourne Webb, P.J., Bodas Freitas, T.M., Freitas Assuncao, R.M.: A review of pile-soil interactions in isolated, thermally-activated piles. *Comput. Geotech.* **108**, 61–74 (2019). <https://doi.org/10.1016/j.comgeo.2018.12.008>
- Robertson, P.K., Campanella G.: Interpretation of cone penetration tests. Part I: Sand. *Can. Geotech. J.* (1983). <https://doi.org/10.1139/t83-078>
- Durgunoglu, T., Mitchell, K.: Static penetration resistance of soils: I-ANALYSIS. In: Proceedings of ASCE Specialty Conference on in-situ Measurement of Soil Parameters, Raleigh, vol. 1 (1975)
- Fadejev, J., Simson, R., Kurnitski, J., Haghightat, F.: A review on energy piles design, sizing and modelling. *Energy* **122**(2017), 390–407 (2017). <https://doi.org/10.1016/j.energy.2017.01.097>
- Hamada, Y., Saitoh, H., Nakamura, M., Kubota, H., Ochifugi, K.: Field performance of an energy pile system for space heating. *Energy Build.* **39**(2007), 517–524 (2007). <https://doi.org/10.1016/j.enbuild.2006.09.006>
- Kalantidou, A., Tang, A.M., Pereira, J.M., Hassen, G.: Preliminary study on the mechanical behaviour of heat exchanger pile in physical model. *Geotechnique* **62** (2012). <https://doi.org/10.1680/geot.11.t.013>
- Khodaparast, M., Kiani, A.M. Bayesteh, H.: Numerical study of bearing capacity and consolidation settlement of energy piles in fine-grained soils. In: *Energy Geotechnics* (2016). ISBN 978-1-138-03299-6. ISBN: 978-1-138-03299-6
- Laloui, L., Nuth, M., Vulliet, L.: Experimental and numerical investigations of the behaviour of a heat exchanger pile. *Int. J. Numer. Anal. Methods Geomech.* **30**, 763–781 (2006). <https://doi.org/10.1016/B978-0-08-100191-2.00016-2>. ISBN: 9780081002384
- Lancellotta, R.: Analisi di Affidabilità in Ingegneria Geotecnica. Atti dell'Istituto di Scienza delle Costruzioni, Number 625, Politecnico di Torino (1983)
- Luo, J., Zhao, H., Gui, S., Xiang, W., Rohn, J.: Study of thermal migration and induced mechanical effects in double U-tube energy piles. *Comput. Geotech.* **91**(2017), 1–11 (2017). <https://doi.org/10.1016/j.comgeo.2017.06.015>. ISSN: 18737633
- Maiorano, R.M.S., Marone, G., Russo, G., Di Girolamo, L.: Experimental behavior and numerical analysis of energy piles. In: XVII ECSMGE 2019 (2019). In print
- Marone, G., Russo, G., Di Girolamo, L.: Carichi termici e carichi meccanici per un palo cfa attestato a tufo. In: IARG GENOVA 2018 (2018)

- Marone, G., Russo, G., Di Girolamo, L.: Studio parametrico del comportamento di un palo singolo sottoposto a carichi termo-meccanici (2019)
- Morrone, B., Coppola, G., Raucci, V.: Energy and economic savings using geothermal heat pumps in different climates. *Energy Convers. Manag.* **88**(2014), 189–198 (2014). <https://doi.org/10.1016/j.enconman.2014.08.007>. ISSN: 01968904
- Murphy, K.D., McCarterney, J.S., Henry, K.S.: Evaluation of thermo-mechanical and thermal behaviour of fullscale energy foundations. *Acta Geotech.* **10**, 179–195 (2015). <https://doi.org/10.1007/s11440-013-0298-4>
- Murphy, K.D., McCarterney, J.S.: Seasonal response of energy piles foundations during building operation. *Geotech. Geol. Eng.* **33**(2), 343–356 (2015). <https://doi.org/10.1007/s10706-014-9802-3>
- Nguyen, V.T., Tang, A.M., Pereira, J.M.: Long-term thermo-mechanical behavior of energy pile in dry sand. *Acta Geotech.* **2017**(12), 729–737 (2017). <https://doi.org/10.1007/s11440-017-0539-z>
- Pahud, D., Hubbuch, M.: Measured thermal performances of the energy pile system of the dock midfield at Zürich airport. In: Proceedings European Geothermal Congress 2007, Unterhaching, Germany, 30 May–1 June 2007 (2007)
- Park, H., Lee, S., Yoon, S., Choi, J.: Evaluation of thermal response and performance of PHC energy pile: Field experiments and numerical simulation. *Appl. Energy* **103**(2013), 12–24 (2013). <https://doi.org/10.1016/j.apenergy.2012.10.012>. ISSN: 03062619
- Parkin, A.K., Lunne, T.: Boundary effects in the laboratory calibration of a cone penetrometer for sand. In: Proceedings of the 2nd European symposium on penetration testing, vol. 2, pp. 761–768 (1982)
- Rammal, D., Mroueh, H., Burlon, S.: Impact of thermal solicitations on the design of energy piles. *Renew. Sustain. Energy Rev.* **92**, 111–120 (2018). <https://doi.org/10.1016/j.rser.2018.04.049>. ISSN: 18790690
- Raucci, M.P.: Comportamento di platee su pali in terreni sabbiosi. Ph.D. thesis, Università degli studi di Napoli Federico II (2017)
- Rotta Loria, A.F., Di Donna, A., Laloui, L.: numerical study on the suitability of centrifuge testing for capturing the thermal-induced mechanical behavior of energy piles. *J. Geotech. Geoenvir. Eng.* (2015). [https://doi.org/10.1061/\(ASCE\)GT1943-5606.0001318](https://doi.org/10.1061/(ASCE)GT1943-5606.0001318)
- Rui, Y., Yin, M.: Investigations of pile-soil interaction under thermo mechanical loading. *Can. Geotech. J.* (2018). <https://doi.org/10.1139/cgj-2017-009>
- Russo, G., Maiorano, R.M.S., Marone, G.: Analysis of thermo-mechanical behaviour of energy piles. Issue of SEAGS-AGSSEA Journal, June 2019
- Saggù, R., Chakraborty, T.: Cyclic thermo-mechanical analysis of energy piles in sand. *Geotech. Geol. Eng.* (2014). <https://doi.org/10.1007/s10706-014-9798-8>
- Santiago, C., Pardo de Santayana, F., de Groot, M., Urchueguia, J., Badenes, B., Magraner, T., Arcos, J.L., Martin, F.: Thermo mechanical behaviour of a thermo-active precast pile. *Bulg. Chem. Commun.* **48**(Special Issue E), 41–54 (2016)
- Sutman, M., Brettmann, T., Guney, Olgun C.: Full-scale in situ tests on energy piles: Head and base restraining effects on the structural behaviour of three energy piles. *Geomech. Energy Environ.* **18**, 56–68 (2019). <https://doi.org/10.1016/j.gete.2018.08.002>
- UNI/TS 11300-1:2014: Evaluation of energy need for heating and cooling
- Vasilescu, R., Fauchille, A., Dano, C., Kotronis, P., Manirakiza, R., Gotteland, P.: Impact of temperature cycles at soil – concrete interface for energy piles. In: *Energy Geotechnics SEG-2018* (2018)
- Wang, C., Kong, G., Liu, H., Ng, C.W.W.: Different types of energy piles with heating-cooling cycles. *Geotech. Eng.* (2017). <https://doi.org/10.1680/jgeen.16.00061>. ISSN:1353-2618

- Yavari, N., Tang, A.M., Pereira, J.M., Hassen, G.: A simple method for numerical modelling of energy pile's mechanical behaviour. *Geotechnique Lett.* (2013). <https://doi.org/10.1680/geolett.13.00053>
- Yavari, N., Tang, A.M., Pereira, J.-M., Hassen, G.: Experimental study on the mechanical behaviour of a heat exchanger pile using physical modelling. *Acta Geotechnica* **9** (2014). <https://doi.org/10.1007/s11440-014-0310-7>
- You, S., Cheng, X., Guo, H., Yao, Z.: Experimental study on structural response of CFG energy piles. *Appl. Therm. Eng.* **48**(Special Issue E), 41–54 (2016)
- Zarrella, A., De Carli, M., Galgaro, A.: Thermal performance of two types of energy foundation pile: helical pipe and triple U-tube. *Appl. Therm. Eng.* **61**(2013), 301–310 (2013). <https://doi.org/10.1016/j.aplthermaleng.2013.08.011>. ISSN:13594311



The Role of Constitutive Material Laws on the Jacking of Single Pile Into Sandy Soil Using Coupled Eulerian-Lagrangian Method

Mohamed Abdelfattah^{1(✉)}, Khalid Abdel-Rahman², Sayed M. Ahmed³, and Yasser M. El-Mossallamy⁴

¹ Ain Shams University, Cairo, Egypt

Mohamed_abdel_fattah@yahoo.com

² Institute of Geotechnical Engineering, Leibniz University, Hannover, Germany

khalid@igth.uni-hannover.de

³ Geotechnical, Ain Shams University, Cairo, Egypt

sayed.mohamed@dar.com

⁴ Geotechnical Engineering, Ain Shams University, Cairo, Egypt

yasser.elmossallamy@arcadis.com

Abstract. The great challenge to study the application involving large deformations is a choice of suitable constitutive law to simulate the soil response during installation of displacement piles. Considering, the nonlinear response, stress history, stress pass and the hardening/softening behavior for constitutive law assess to achieve the realistic behavior of piles during installation. In this study, the large deformations response associated with pile jacking are considered using a novel numerical approach which it calls coupled Eulerian-Lagrangian method (CEL). The used constitutive laws in study herein are partly based on elastoplastic theory while the other based on hypoplastic theory. Mohr-Coulomb and Cap plasticity constitutive law based on elastoplastic theory are adopted, while the Hypoplastic constitutive law formulated by Von Wolffersdorff was implemented using a material subroutine (VUMAT). The used constitutive laws are firstly calibrated with database of Hostun sand to simulate the jacking pile and investigate the response of pile using the corresponding constitutive law. Secondly, using the results of laboratory-scale at purdue university for jacking of pile into silica sand of #2Q-ROK are compared with numerical results to investigate the more realistic constitutive law with geotechnical applications involving large deformations such as jacking pile into sandy soil.

1 Introduction

Serval constitutive laws could be used to model soil response which would be classified based on elastic theories, elasto-plastic theories and hypoplasticity. The theories based on plasticity could be grouped into elastic-perfect plastic such as Mohr-Coulomb and Drucker-Prager, in addition, cap models such as cap plasticity and Hardening soil model. On the other hand, the hypoplasticity concept which was developed by Kolymbas (1985), it describes soil plasticity using nonlinear tensorial functions of the rate-type and are characterized by simple formulation and few parameters.

Many researches were performed the geotechnical applications with sandy soil involving large deformations techniques based on Elasto-plastic theory using Mohr-Coulomb constitutive model such as Craig and Chua (1990) to simulate numerically deep penetration of spud-can foundations on sand and clay. Susila and Hryciw (2003) used the Drucker- Prager constitutive law to investigate the cone penetration test (CPT) in normally consolidated sand. Dijkstra et al. (2008) used Hardening Soil model (HSM) to model displacement pile installation into Baskarp sand. Qiu et al. (2009) used Drucker-Prager model and Cap Plasticity to simulate anchor plate problem and pile penetration process in cohesionless soil respectively.

Basu (2009) used a constitutive law based on critical-state soil mechanics which proposed by Manzari and Dafalias (1997) and modified by Loukidis and Salgado (2009) in order to perform analysis of shaft resistance of jacked and drilled-displacement piles in sandy soil. Qiu et al. (2011) simulated the pile jacking into Mai-Liao sand and ship grounding into Hochstetten gravel. Based on Hypoplastic theory, Pucker and Grabe (2012) simulated the installation process of full displacement piles into Karlsruher sand. Ko et al. (2016) used Mohr-Coulomb to study steel driven piles with soil plugging.

Zhao et al. (2016) to predict the penetration resistance profile of spudcan foundation on sediments with interbedded medium-loose sand layer. Khoa and Jostad (2016) used modified Mohr-Coulomb, which the failure and post-failure strain softening are defined, in order to conduct analyses of offshore foundations and suction anchors. Galavi et al. (2017) simulated pile installation in saturated Cuxhaven sand by using MPM method. Abdelfattah et al. (2018) used Cap Plasticity to simulate pile jacking into sandy soil considering large deformation during installation. Elkadi et al. (2018) used two constitutive laws to define Baskarp sand by hypoplastic model and the double-hardening soil model (DHS) for simulating pile installation.

In study herein, parameters of Hostun sand are calibrated numerically in explicit scheme based on database of triaxial and oedometer tests with Hypoplastic and elastoplastic constitutive laws. Mohr-Coulomb and Cap plasticity based on elasto-plastic theory are defined in Abaqus's library while, Hypoplastic, which is formulated by Von Wolffersdorff, is implemented using a user subroutine (Vumat) provided by Gudehus et al. (2008). The calibrated Hostun parameters are developed to simulate jacked pile process into calibrated chamber by Purdue university. In the second stage, using the measurements of jacking force during pile installation into calibrated chamber by Purdue university contented of silica sand of #2Q-ROK are compared with numerical results to investigate the more realistic constitutive law with jacking pile into sandy soil.

2 Constitutive Laws

2.1 Mohr Coulomb

Mohr-Coulomb is a classical criterion and widely used for geotechnical applications is which is elastic perfectly plastic to simulate soil stress-strain response. The model is defined as Eq. 1 while considering principal stress ($\sigma_1 - \sigma_2 - \sigma_3$) space; the general

state in terms of three stress invariants is developed as Eq. 2. The flow potential, G , is hyperbolic function in meridional plane and smooth elliptic function in deviatoric plane and is defined by Eq. 3.

$$\tau = c - \sigma \tan \varphi \quad (1)$$

$$F = Rmc q - p \tan \varphi - C = 0 \quad (2)$$

$$G = \sqrt{(\epsilon c_0 \tan \psi)^2 + (R_{mw} q)^2} - P \tan \psi \quad (3)$$

where,

ϕ is friction angle of material and is slope of the Mohr-Coulomb yield surface in the $p - R_{mc}$ stress plane, C is cohesion of material, ψ is the dilation angle measured in the $p - R_{mw}$ plane, c_0 is the initial cohesion yield stress and ϵ refer to the eccentricity which the flow potential tends to a straight line as the eccentricity tends to zero.

2.2 Cap Plasticity

Stress history, nonlinear response, stress pass and control hardening/softening behaviour are considered by Cap plasticity model which consists of Drucker-Prager yield criterion, cap yield surface and transition surface as shown in Fig. 1. Drucker-Prager shear surface is defined by d and β parameters and could be matched with Mohr-Coulomb parameters c and ϕ in meridional plane with three-dimensional space by Eq. 4. Flow stress ratio, K , describes shape of shear surface as Eq. 5, which is within range $0.778 \leq k \leq 1$ to ensure the surface is convex.

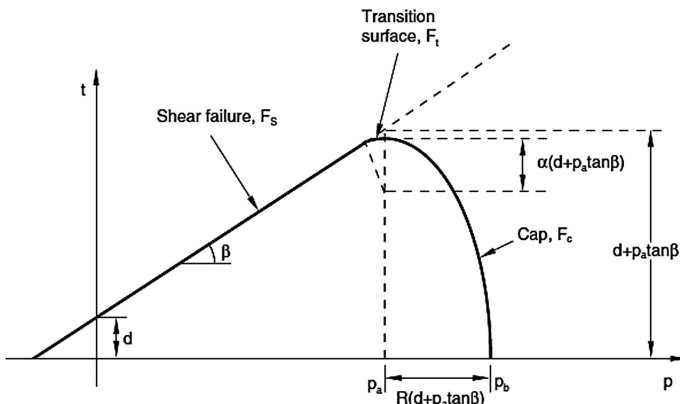


Fig. 1. Cap plasticity surfaces in meridional plane (ABAQUS manual)

$$\tan \beta = \frac{6 \cdot \sin \varphi}{3 - \sin \varphi} \quad (4)$$

$$k = \frac{3 - \sin \varphi}{3 + \sin \varphi} \quad (5)$$

The cap yield surface is described as an ellipse with eccentricity (R) in the $p - t$ plane and controls hardening/softening behaviour by user-defined piecewise linear function relating the hydrostatic compression yield stress (P_b) and the volumetric inelastic strain ($\dot{\epsilon}_v^p$), which can be obtained from the isotropic compression test results. The intersection between cap surface and Drucker-Prager shear surface is smooth transition surface, which is defined by typically value of α between 0.01 and 0.05.

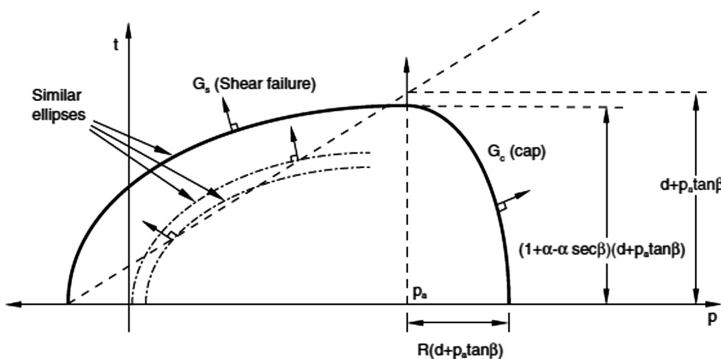


Fig. 2. Flow potential for Cap Plasticity in meridional plane (ABAQUS manual)

The flow potential is defined in meridional plane as associated in the cap surface while non-associated in both shear and transition surface. Elliptical portions in meridional plane is described potential surfaces is as shown in Fig. 2. The surfaces for cap surface G_c and for both shear and transition surface G_s are defined in Eqs. 6 and 7, respectively, where, t is deviatoric stress measure.

$$G_c = \sqrt{(P - p_a)^2 + \left(\frac{Rt}{1 + \alpha - \frac{\alpha}{\cos \beta}} \right)^2} \quad (6)$$

$$G_s = \sqrt{[(P - p_a)\tan \beta]^2 + \left(\frac{t}{1 + \alpha - \frac{\alpha}{\cos \beta}} \right)^2} \quad (7)$$

Where, t is deviatoric stress measure and P_a is an evolution parameter that represents the volumetric plastic strain driven hardening/softening.

$$p_a = \left(\frac{P_b - R.d}{1 + R \cdot \tan \beta} \right)$$

2.3 Hypoplastic Model

Soil response in hypoplastic model is defined by nonlinear tensorial functions of the rate-type. Early, Kolymbas (1985) considered Cauchy stress as the state variable (T_s). Later other states variables of void ratio (e) and critical state concept were formulated for granular materials by Gudehus (1996), Bauer and (1996), Wu (1992) and Wu and Bauer (1994). The general framework for stress rate tensor \dot{T} is determined by stretching tensor of granular skeleton, D and the current void ratio, e as shown in Eq. 8. Wolffersdorff (1996) organized widely used formulation considering Matsuoka/Nakai criterion for yield critical state.

$$\dot{T} = F(T_s, D, e) \quad (8)$$

The tensorial function of hypoplastic model yields to scalar factors f_s (barotropy factor) to allow consistency condition for isotropic compression starting from void ratio at zero pressure and f_d (pyknontropy factor) to consider pressure-dependent relative void ratio. Bauer (1996) organized the limiting void ratios e_i , e_d and e_c with increasing pressure as Eq. 12. Figure 3 shows the relation between void ratios and logarithmic normalized pressure.

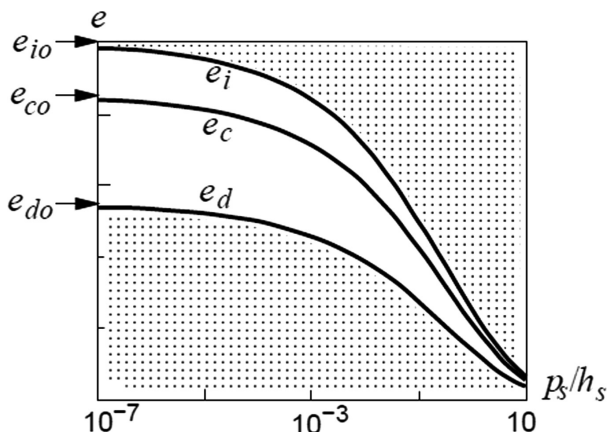


Fig. 3. Limiting pressure-dependent void ratio lines for hypoplastic model (after, Herle and Gudehus)

$$fs = \frac{hs}{n} \left(\frac{ei}{e} \right)^\beta \frac{1+e}{e} \left(\frac{-trT}{hs} \right)^{1-n} \left[3 + a^2 - a\sqrt{3} \left(\frac{eio - edo}{eco - edo} \right)^\alpha \right]^{-1} \quad (9)$$

$$fd = \left(\frac{e - ed}{ec - ed} \right)^\alpha \quad (10)$$

$$a = \frac{\sqrt{3}(3 - \sin \varphi_c)}{2\sqrt{2}\sin \varphi_c} \quad (11)$$

$$\frac{e_i}{e_{i0}} = \frac{e_c}{e_{c0}} = \frac{e_d}{e_{d0}} = \exp \left(- \frac{3PS}{h_s} \right)^n \quad (12)$$

The stiffness parameters are defined by granulate hardness h_s at reference pressure and exponent n to consider the increasing the incremental stiffness with pressure. Both parameters are estimated by compression test either oedometer or isotropic compression test. Peak friction angle is controlled by exponent α which is calibrated using drained triaxial tests on dense soil. Herle and Gudehus (1999) presented a simple framework to estimate void ratios at zero pressure e_{i0} , e_{do} and e_{co} using index tests., approximately, eco equals maximum void ratio while e_{do} equals minimum void ratio as well as e_{i0} is 1.20 times of maximum void. The exponent α could be estimated by the relationship between peak friction angle and critical friction angle as shown in Fig. 4.

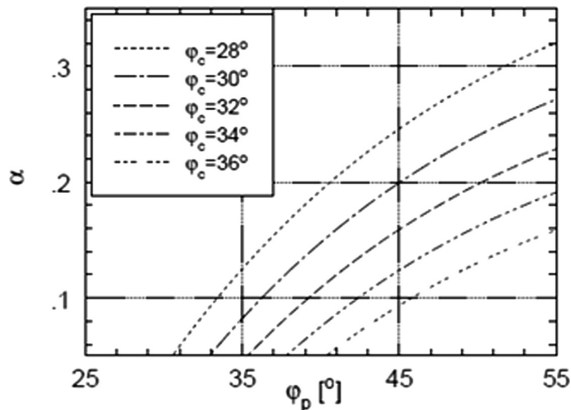


Fig. 4. Relation parameter α with φ_{peak} and $\varphi_{critical}$ for hypoplastic model (after, Herle and Gudehus)

3 Calibration of Used Sand Parameters Numerically

Hypoplasticity model is implemented in Abaqus/Explicit by a user subroutine (Vumat) provided by Gudehus et al. (2008) which was developed by Von Wolffersdorff (1996) with small-strain extension by Niemunis and Herle (1997), while Mohr-Coulomb and Cap plasticity are implemented by Abaqus's library.

3.1 Hostun Loose Sand

A series laboratory tests were conducted on loose sand with initial void ratio 0.82–0.85 at Grenoble and Stuttgrat and the soil behaviour were developed numerically by Marcher et al. (2000) to utilize it for Hypoplastic and elasto-plastic models. Herewith, the calibrated parameters of Hostun sand were developed numerically using one element of CAX4R in Abaqus based on Mohr-Coulomb, Cap plasticity and Hypoplastic model against the laboratory results in terms of triaxial and oedometer, the set parameters of Hypoplastic model as shown in Table 1 were investigated by Marcher et al. (2000), whereas, the parameters of elasto-plastic models shown in Table 2 were determined based on elasto-plastic rules with results of lab-tests, Fig. 5 shows the cap hardening curves used for cap plasticity model (Hostun sand & 2Q-ROK sand).

Table 1. Parameters of Hostun sand for hypoplastic model

φ_c	h_s	n	e_{do}	e_{co}	e_{io}	α
32	1000 MPa	0.29	0.61	0.91	1.09	0.19
β	m_R	m_T	R	β_r	χ	e_0
2	5	2	1e-5	0.5	6	0.85

Table 2. Parameters of Hostun sand for elasto-plastic models

Model	Mohr-Coulomb	Cap plasticity
E_s (kPa)	20000	30000
v	0.20	0.38
φ (Degree)	34	—
ψ (Degree)	0.10	—
β (Degree)	—	54
α	—	0.03
Initial cap position	—	0.003
R	—	1
K	—	0.778

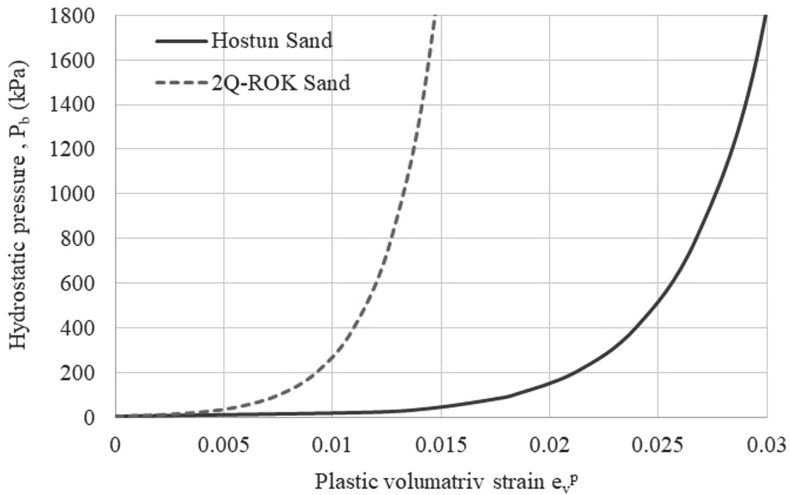


Fig. 5. Cap-hardening curve used in analysis

3.1.1 Triaxial Tests

Triaxial test was simulated with confining stress of 100 kPa and 300 kPa. Displacement control was applied for shearing stage. Figures 6 and 7 show the comparison between response of constitutive laws for isotropic stress 100 kPa and 300 kPa respectively. Cap plasticity model performed a well correlation with triaxial tests for

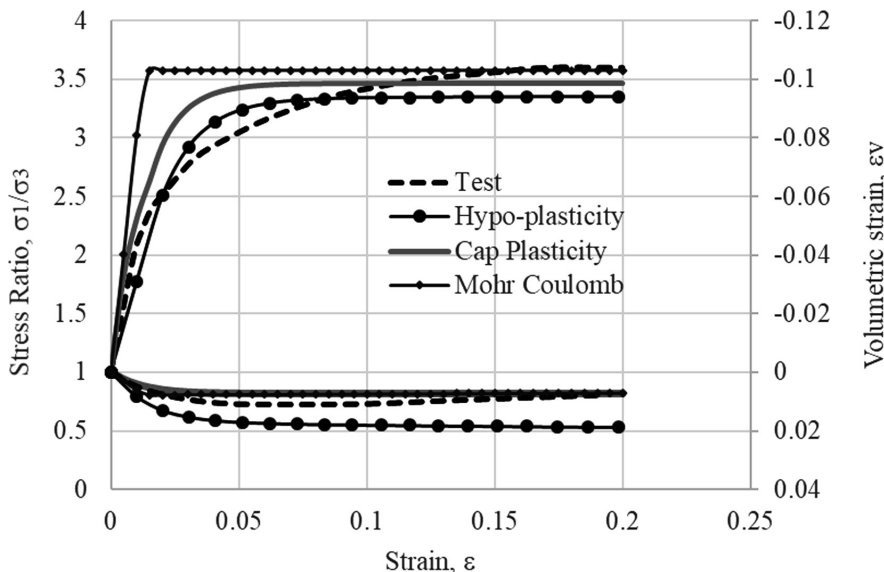


Fig. 6. Comparison between laboratory triaxial test with isotropic pressure of 100 kPa and numerical results for Hostun sand

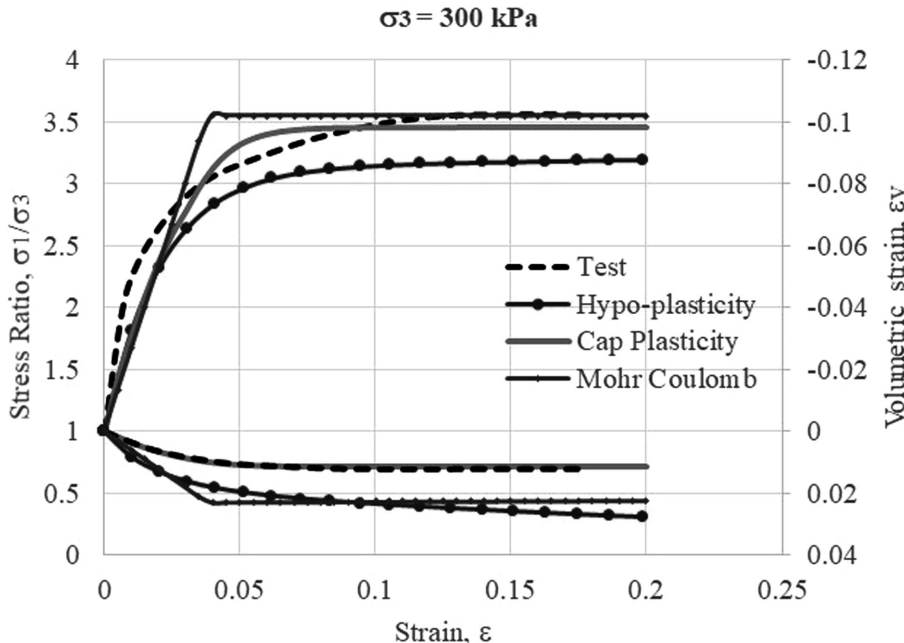


Fig. 7. Comparison between laboratory triaxial test with isotropic pressure of 300 kPa and numerical results for Hostun sand

both confining pressure in terms of contraction and deviatoric stress better than Mohr-Coulomb, while the Hypoplastic model was suffering higher contraction and lower failure stress than lab-test for both isotropic levels.

3.1.2 Oedometer Test

The oedometer test was performed for loading-unloading loops at 50, 100 and 200 kPa. Figure 8 shows the comparison between oedometer test and behavior of used constitutive laws. A well response for Cap plasticity model during loading – unloading loops with oedometer test, in contrast of both Mohr-Coulomb and Hypoplastic model. The Hypoplastic model could capture one loop only but it could not consistently distinguish between loading-unloading loops Marcher et al. (2000), even using intergranular strain.

3.2 #2Q-ROK Dense Sand

2Q-ROK is described as angular particles of silica sand from the Oriskany sandstone deposits at Berkeley Springs in West Virginia. The mean particle size D_{50} is 0.78 mm, the coefficient of uniformity C_u is 1.43 and the specific gravity G_s is 2.65. The maximum and minimum void ratios e_{\max} and e_{\min} are 0.998 and 0.668, respectively. The critical-state friction angle and peak friction angle using direct shear is 32.3° and 40.2° , respectively. The interface friction angle between pile material and 2Q-ROK sand was found to be 21.60° .

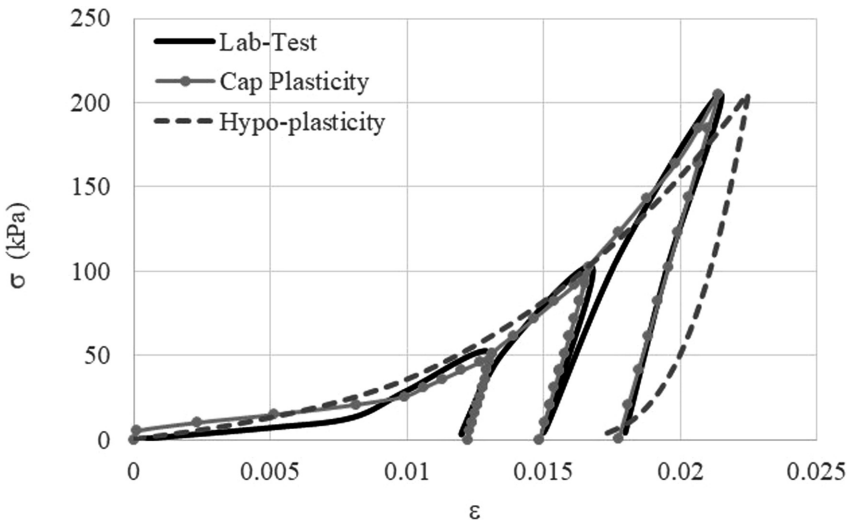


Fig. 8. Comparison between laboratory oedometer and numerical results for Hostun sand

3.2.1 Calibration of 2Q-ROK Sand Parameters

Arshad (2014) performed one loop of loading oedometer test up to 10 MPa on very dense sand with relative density, Dr of 85%. The stiffness parameters were calibrated numerically using one element of CAX4R in Abaqus for Cap plasticity and Hypoplastic model against the laboratory results. the cap hardening used for cap plasticity model was estimated as shown in Fig. 5. The other parameters used for Hypoplastic model were estimated based on Herle and Gudehus (1998), while shearing

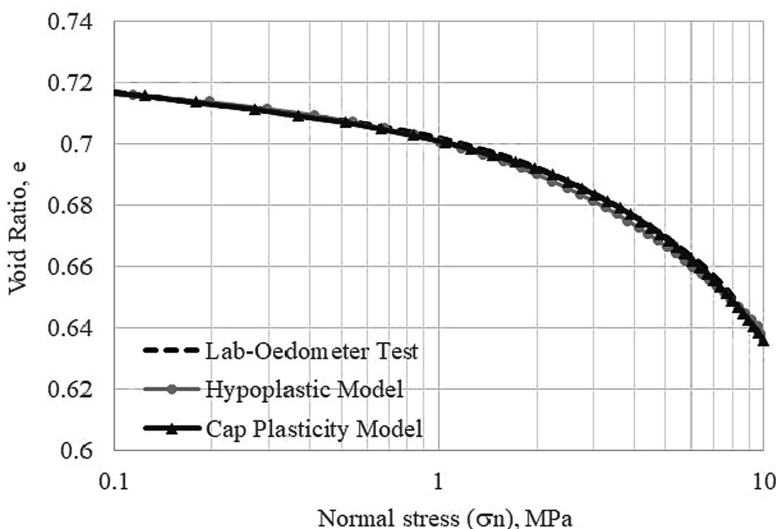


Fig. 9. Comparison between laboratory oedometer and numerical results for 2Q-ROK sand

parameters for Cap plasticity model were estimated using peak friction angle in p-q space. The calibrated parameters are well agreed with oedometer test as shown in Fig. 9. Unfortunately, Mohr Coulomb stiffness could not be calibrated with oedometer test due to its shortcomings for not taking into account the stiffness-stress dependency. Tables 3 and 4 show the calibrated parameters for Hypoplastic and elasto-plastic constitutive laws.

Table 3. Parameters of 2Q-ROK sand for hypoplastic model

ϕ_c	h_s	n	e_{do}	e_{co}	e_{io}	α
32.30	300 MPa	0.6	0.668	0.998	1.19	0.12
β	m_R	m_T	R	β_r	χ	e_o
1	5	2	1e-5	0.5	6	0.72

Table 4. Parameters of 2Q-ROK sand for elasto-plastic models

Model	Mohr-Coulomb	Cap plasticity
E_s (kPa)	12500	45000
v	0.30	0.47
ϕ (Degree)	41	—
ψ (Degree)	0.10	—
β (Degree)	—	59
α	—	0.05
Initial cap position	—	0.0057
R	—	2.5
K	—	0.778

4 Simulation of Jacking Pile into Sandy Soil

4.1 Coupled Eulerian-Lagrangian Approach

A novel numerical approach called Coupled Eulerian-Lagrangian (CEL) which is used in ABAQUS is explicit integration scheme known as the forward Euler or central difference algorithm. The numerical stability is defined by $\Delta t_{min} = L_e/C_d$ where, L_e is characteristic element length and C_d is dilatory wave speed. The equilibrium in ABAQUS/explicit is defined by $M \ddot{U} = P - I$ where, M is lumped mass, \ddot{U} is acceleration, P is the external load vector and I is the internal load vector. The quasi-static analyses are achieved when kinetic energy is within 5.0%–10.0% of internal energy (ABAQUS).

4.2 Eulerian Domain

The Eulerian domain depends on Eulerian volume fraction (EVF), when the EVF is equal to one, the domain is filled with material, whereas, the domain is empty, when

EVF equals zero. The void material has neither mass nor strength. In initial condition, the layer with EVF equal zero (empty layer) in Eulerian domain should be assigned above soil layers in order to allow the material to heave and flow freely at the subsequent stages of the analysis.

4.3 Contact Algorithm

General contact based on penalty contact method was utilized for describing soil-pile interface. The contact algorithm tracks the Lagrangian structure, which occupies void regions inside the Eulerian mesh and computes the interface between the Lagrangian structure and the Eulerian materials. The mechanical contact properties were used to define the relationship of contact between the parts.

Coulomb friction law and Hard contact model were used to describe tangential and normal contact respectively between Lagrangian body (pile) and Eulerian material (soil). Hard contact model was used to define normal contact behaviour when the clearance between two surfaces becomes zero and allows separation after contact, whereas, Coulomb friction was utilized by friction coefficient (μ) to define shear stress (τ_c) based on contact pressure (p) using the function $\tau_c = \mu.P$.

5 Finite Element Model

The calibration chamber prepared by Purdue university used in numerical models consists of 1680 mm in diameter and a height of 1200 mm. The pile diameter of 31.75 mm with conical base of 60° was selected to minimize the effect of chamber boundaries (Salgado 2013). The effect of the chamber boundaries on model piles had been interpreted by Ghionna and Jamiolkowski 1991; Salgado et al. 1998. This equipment was used by many Purdue researchers such as Tehrani (2014), Arshad (2014), Tovar-Valencia et al. (2018a, b). A pressure of 50.0 kPa was applied on top of soil to consider the deep penetration of pile according to Arshad (2014).

In order to consider large deformations induced during pile penetration, the CEL method was applied in three-dimensional domain (3-D) using one-quarter of space due symmetry condition. The soil was modeled by Eulerian element of EC3D8R, i.e. 8-node linear Eulerian brick element, reduced integration, while, the pile was modeled by rigid body of Lagrangian element with 8-node brick element. Figure 10 shows the used geometry and CEL model for analyzing process of jacked pile using different of constitutive laws.

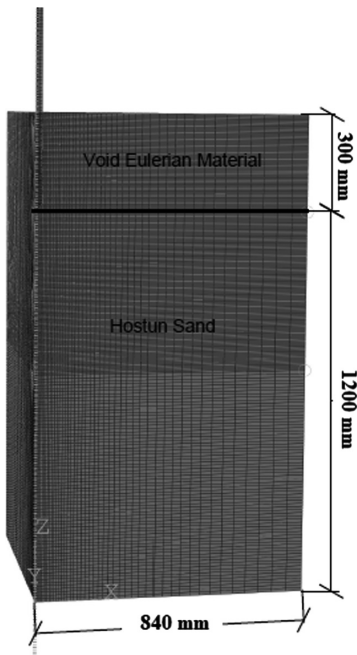


Fig. 10. Geometry and CEL model for analysing jacking pile

6 Response of Pile Jacking Into Dense 2q-Rok Sand

Figure 11 shows the jacking force with penetration depth by the used constitutive laws (Mohr-Coulomb, Cap Plasticity and Hypoplasticity model). It is clear seen that the used constitutive laws are agreed with straight portion up to 3 kN of experimental test. Hypoplastic model is suffering oscillation after yield point and the results is underestimated with experimental test. The back-calculation was performed to estimate the equivalent stiffness parameter for Mohr coulomb, as well as, the dilatancy angle is omitted to prevent very large volumetric strains with large displacements due to MC shortcomings of dilatation cut-off. which was performed by others such as Dijkstra et al. (2009). Cap Plasticity model is well agreed and consistently distinguish with experimental test. Figures 12 and 13 show the soil movement at penetration depth four times of pile radius for Cap Plasticity and Hypoplastic model respectively, Cap model appeared more realistic behaviour of soil movement than hypoplastic model compared with experimental test.

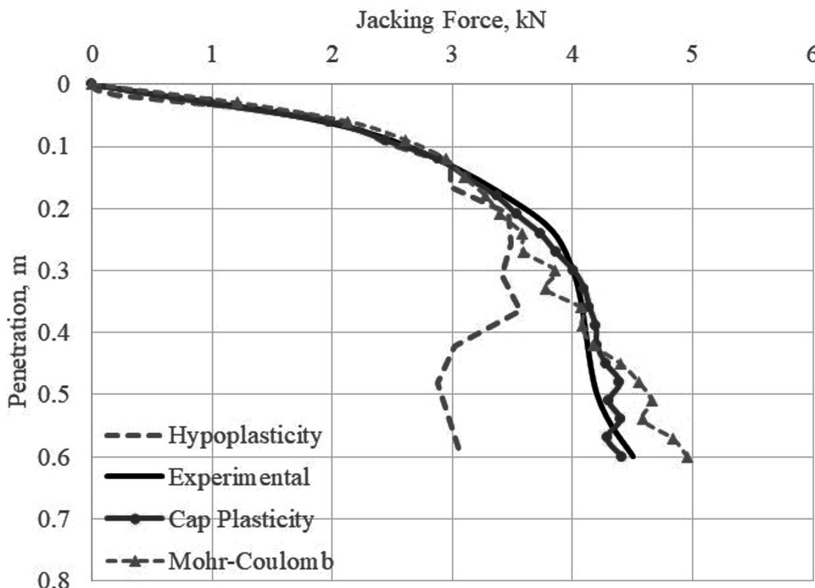


Fig. 11. Response of pile jacking into 2Q-ROK sand

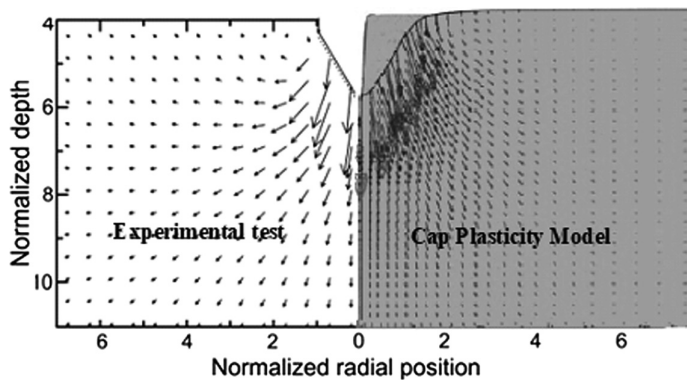


Fig. 12. Soil displacement using Cap plasticity during pile jacking into 2Q-ROK sand compared with experimental test

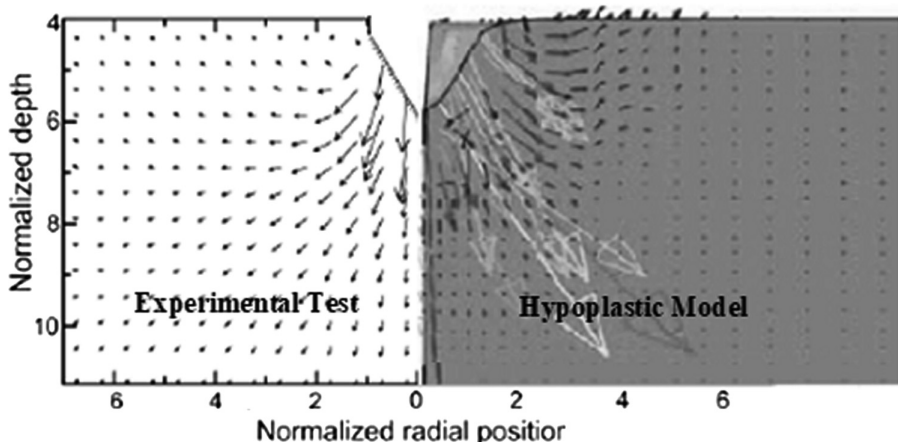


Fig. 13. Soil displacement using Hypoplastic model during pile jacking into 2Q-ROK sand compared with experimental test

7 Conclusions

The elastoplastic models appear capable of capturing the jacking response more than hypoplastic model. Unfortunately, hypoplastic model appeared not capable of capturing the jacking response for all stress levels and was suffering oscillation after yield point. Cap Plasticity model is well agreed consistently with experimental test and it proved capability for simulating sandy soil response yield geotechnics applications involving large deformations such as pile jacking, where, Cap plasticity model took into account stress-dependent stiffness other than Mohr-Coulomb which it is no distinction between primary loading and unloading or reloading. The stiffness plays a significant role for jacking response thus, the used constitutive law has to be considered stiffness depending on the stress level and stress path like Cap plasticity model.

References

- Abdelfattah, M., Abdel-Rahman, K., Ahmed, S.M., EL-Mossallamy, Y.M.: Modelling of pile jacking into sandy soil considering large deformation behavior using coupled Eulerian Lagrangian method (CEL). In: Proceedings of the 15th International Conference on Structural and Geotechnical Engineering, Cairo (2018)
- Arshad, M.I.: Experimental study of the displacements caused by cone penetration in sand. (Doctoral dissertation, Purdue University) (2014)
- Basu, P.: Analysis of shaft resistance of jacked and drilled-displacement piles (Doctoral dissertation, Purdue University) (2009)
- Bauer, E.: Calibration of a comprehensive hypoplastic model for granular materials. *Soils Found.* **36**(1), 13–26 (1996)
- Craig, W.H., Chua, K.: Deep penetration of spud-can foundations on sand and clay. *Géotechnique* **40**(4), 541–556 (1990)

- Dassault Systèmes, ABAQUS User's Manual (2016)
- Dijkstra, J., Broere, W., Van Tol, A.F.: 45 Modelling displacement pile installation in a finite element method. In: Proceedings of the Second BGA International Conference on Foundations (2008)
- Dijkstra, J., Broere, W., van Tol, A.F.: Eulerian simulation of the installation process of a displacement pile. *Geotech. Spec. Publ.* **186**, 135–142 (2009)
- Elkadi, A., Galavi, V., Martinelli, M.: Numerical simulation of pile Installation with the material point method. In: Proceedings of the 15th International Conference on Structural and Geotechnical Engineering, Cairo (2018)
- Galavi, V., Beuth, L., Coelho, B.Z., Tehrani, F.S., Hölscher, P., Van Tol, F.: Numerical simulation of pile installation in saturated sand using material point method. *Procedia Eng.* **175**, 72–79 (2017)
- Herle, I., Gudehus, G.: Determination of parameters of a hypoplastic constitutive model from properties of grain assemblies. *Mech. Cohesive Frict. Mater. Int. J. Exp. Model. Comput. Mater. Struct.* **4**(5), 461–486 (1999)
- Khoa, H.D.V., Jostad, H.P.: Application of coupled Eulerian-Lagrangian method to large deformation analyses of offshore foundations and suction anchors. *Int. J. Offshore Polar Eng.* **26**(03), 304–314 (2016)
- Ko, J., Jeong, S., Lee, J.K.: Large deformation FE analysis of driven steel pipe piles with soil plugging. *Comput. Geotech.* **71**, 82–97 (2016)
- Marcher, T., Vermeer, P.A., Von Wolfersdorff, P.A.: Hypoplastic and elastoplastic modelling—a comparison with test data. In: *Constitutive Modelling of Granular Materials*, pp. 353–374. Springer, Heidelberg (2000)
- Niemunis, A., Herle, I.: Hypoplastic model for cohesionless soils with elastic strain range. *Mech. Cohesive Frict. Mater. Int. J. Exp. Model. Comput. Mater. Struct.* **2**(4), 279–299 (1997)
- Pucker, T., Grabe, J.: Numerical simulation of the installation process of full displacement piles. *Comput. Geotech.* **45**, 93–106 (2012)
- Qiu, G., Henke, S., Grabe, J.: Applications of coupled Eulerian-Lagrangian method to geotechnical problems with large deformations. In: *Proceeding of SIMULIA Customer Conference*, pp. 420–435 (2009)
- Qiu, G., Henke, S., Grabe, J.: Application of a coupled Eulerian-Lagrangian approach on geomechanical problems involving large deformations. *Comput. Geotech.* **38**(1), 30–39 (2011)
- Rowe, P.W.: The stress-dilatancy relation for static equilibrium of an assembly of particles in contact. *Proc. R. Soc. London. Ser. A. Math. Phys. Sci.* **269**(1339), 500–527 (1962)
- Sheng, D., Eigenbrod, K.D., Wriggers, P.: Finite element analysis of pile installation using large-slip frictional contact. *Comput. Geotech.* **32**(1), 17–26 (2005)
- Tho, K.K., Leung, C.F., Chow, Y.K., Swaddiwudhipong, S.: Eulerian finite-element technique for analysis of jack-up spudcan penetration. *Int. J. Geomech.* **12**(1), 64–73 (2012)
- Tovar-Valencia, R.D., Galvis-Castro, A., Salgado, R., Prezzi, M.: Effect of surface roughness on the shaft resistance of displacement model piles in sand. *J. Geotech. Geoenviron. Eng.* **144**(3) (2018a)
- Tovar-Valencia, R.D., Galvis-Castro, A.C., Prezzi, M., Salgado, R.: Short-term setup of jacked piles in a calibration chamber. *J. Geotech. Geoenviron. Eng.* **144**(12) (2018b)
- Von Wolfersdorff, P.A.: A hypoplastic relation for granular materials with a predefined limit state surface. *Mech. Cohesive Frict. Mater. Int. J. Exp. Model. Comput. Mater. Struct.* **1**(3), 251–271 (1996)
- Wu, W., Bauer, E.: A simple hypoplastic constitutive model for sand. *Int. J. Numer. Anal. Methods Geomech.* **18**(12), 833–862 (1994)

Yu, L., Hu, Y., Liu, J., Randolph, M.F., Kong, X.: Numerical study of spudcan penetration in loose sand overlying clay. *Comput. Geotech.* **46**, 1–12 (2012)

Zhao, J., Jang, B.S., Duan, M., Song, L.: Simplified numerical prediction of the penetration resistance profile of spudcan foundation on sediments with interbedded medium-loose sand layer. *Appl. Ocean Res.* **55**, 89–101 (2016)



Numerical Analysis of Instabilities Affecting an Excavation on the High Speed Line in Northern Morocco

Ghizlane Ardouz^(✉) and Khadija Baba

LGCE Laboratory, High School of Technology-Salé,
Mohammed V University in Rabat-Morocco, Rabat, Morocco
ghizlane.ardouz@gmail.com

Abstract. The study presented in this paper deals with the numerical analysis by the finite element method of the behavior of an excavation, of the high speed line in the North of Morocco, which has undergone successive sliding after its excavation. With the Plaxis finite element software, and with the tracking paths stress and deformation of different points in the unstable mass, the development of the failure mechanism can be examined. The analysis of the stability of the massif allowed us to highlight the existence of potentially unstable zones.

1 Introduction

Landslides are the most spectacular and the most common among the mass movements, whose appearance causes deformations of the earth crust. They develop in a range of loose soils or soft rocks and occur under a wide variety of circumstances, affecting man-made structures (cuttings and embankments) or natural slopes.

The danger of the occurrence of a slip can be estimated by analyzing the variation of the safety factor according to the shape and position of a possible sliding surface for which the safety factor has the minimum value represents the critical fracture surface.

In the context of this article, a finite element analysis has been established to better understand the instabilities of the trigger mechanism on a railway excavated north of Morocco in the rural commune of Hjar Nhal.

2 Presentation of the Study Area

2.1 Geographical Context

The excavation object of the present study is located in the high-speed line connecting Kenitra Tangier, specifically on rural commune Hjar Nhal, Tangier-Tétouan-Al Hoceima region (Fig. 1).

It extends over a length of 1170 m, its maximum height is 62 m to the axis.



Fig. 1. Location of the excavation

2.2 Geological Context

The hill of Hjar Nhal where the excavation is made marks the North-West fringe of the tablecloth of Numidian sandstones. It is a formation that was carried during the rifan tectonic movements, and which is based on the clayey pelites of the Lower Tangier Unit. According to the geological map of Tangier (Fig. 2), this layer is formed in the upper part by an alternation of sandstone and G (N) pelites, at the base of this formation more clay or pelitic levels are present A (N).

From a lithological point of view, we therefore distinguish:

- alternating layers of sandstone (G2) and weathered pelites (E5a);
- The pure pelites (E5) in the bottom of excavation;
- The summit is covered with reddish silt clays of surface (E/C).

2.3 Hydrogeological Context

Piezometric measures could not be carried on bunk aquifers (no selective piezometers). However, it appears that the sandstone is relatively porous ($n = 12\%$) and therefore potentially aquifers with alternating more clayey levels of pelites probably constituting the wall of these aquifers (Fig. 3).

This is confirmed by the existence of numerous sources at the base of the excavation, at the interface between the Numidian sandstones and the pelites of the Tangier aquifer.

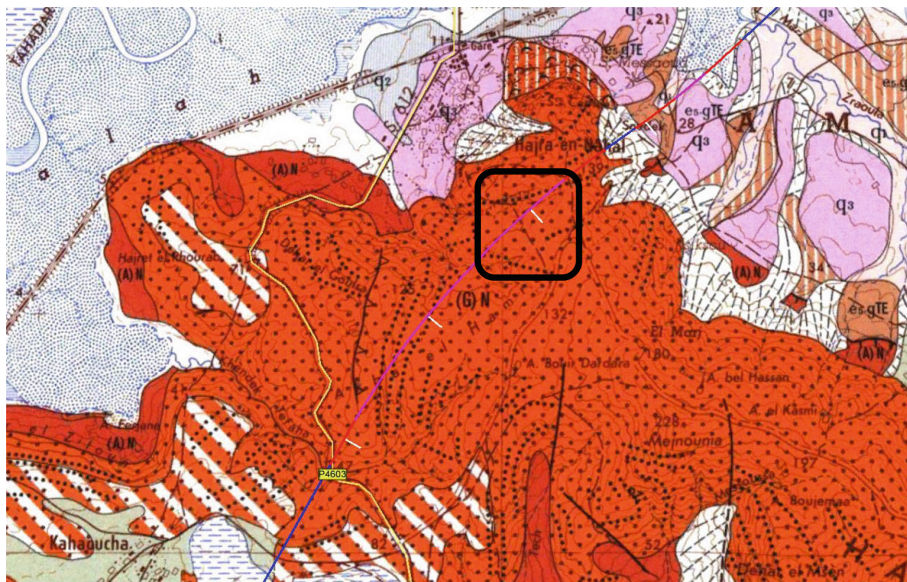


Fig. 2. Geographical location of the excavation - extracted from the 1:50,000 geological map of Tangier

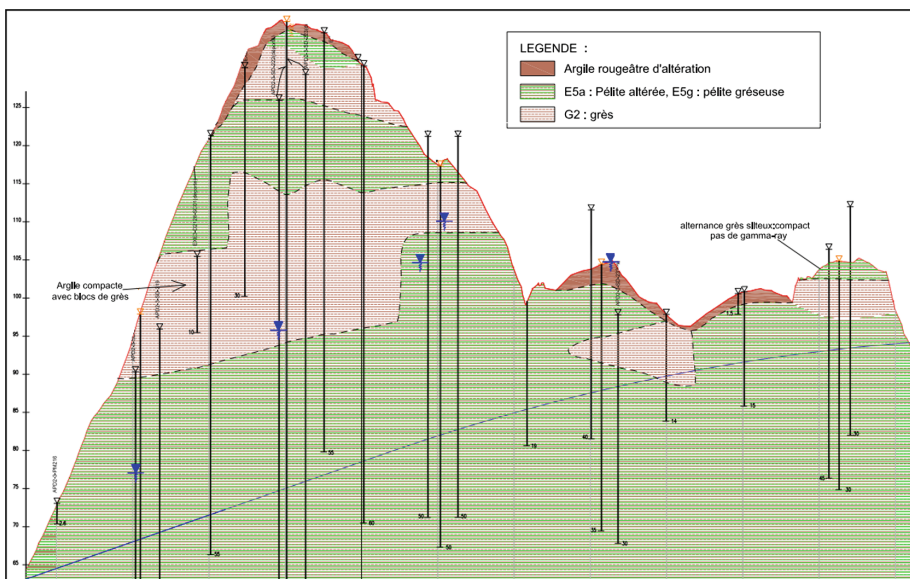


Fig. 3. Geotechnical length profile of the excavation with the implementation of the various surveys

3 Geotechnical Synthesis

The geotechnical reconnaissance of the structure has resulted in many in situ and laboratory tests.

3.1 Classification and Description of the Different Formations

The following categories of materials are defined:

- E/C: soil cover colluviated predominantly clay;
- E5a: alteration products of the pelites, mainly located between 0 and 10 m approximately;
- E5: pure, rocky pelites;
- E5 g: alternation of pelite and sandstone (the sandstone benches represent between 15 and 40%);
- E5 g/G: alternation of pelite and sandstone in approximately equal proportion - G2: sandstone, possibly with pelitic schools of minority (less than 20% pelite);
- Ga: alteration of sandstone.

3.1.1 Formation of Surface E/C: Scree, Colluvions

These materials, described as reddish variegated clays, are the alteration results, sometimes colluviated, of the underlying materials (pelites). They are met on the first 2 meters, and are located on the top of the mounds.

The results of the laboratory tests on the samples assigned to this formation show that they are mainly clay materials mainly classified A2 and A3. The hydric state is mostly wet with water contents of 21% on average.

3.1.2 Pelitic Formations

In terms of identification, it is very difficult to distinguish the different pelitic formations. In particular, the tests carried out in the sandstone bench pelites were carried out either in sandstone banks - in which case the results are then attached to the G2 sandstones - either in the pelite banks, whose characteristics are very similar to the weathered pelites. E5a or healthy E5. All pelitic materials are materials containing a significant proportion of fines, mostly classified A2 in the sense of the GTR (52%), with a minor fraction of A3 (35% of the total). In place, these materials are likely to be classified as R34 (7% of samples) - this is more likely to be E5 healthy pelites or E5 g pelitic beds.

The hydric states are predominantly "m" (36%) and "s" (40%). There does not seem to be any noticeable difference between the hydric states of the E5a and the deeper pelites (E5 and E5 g).

The average of the IPI is 19. Thus, one can differentiate the most altered facies (IPI = 14 on average) of the healthier facies (IPI = 28 to 63).

The swelling values measured on immersion in a CBR mold are between 1.2 and 2%, which is the average of the pelitic samples. However, one sample showed a swelling of 20.7%. If this value does not result from an input error, it tends to show that there is a significant risk of meeting highly inflating levels within the pelites.

3.1.3 Numidian Sandstone G2 and their Alteration Ga

These materials are rated R43 to R41/R42 (50% each) for the most indurated levels

3.2 Triaxial Test

Two triaxial tests were carried out in weathered pelites and surface clays. The characteristics retained for each facies are presented in Table 1.

Table 1. Mechanical soil characteristics applied in the calculations

Facies	Cohesion (kPa)	Internal friction (°)	Density (kN/m3)
Surface clays	5	25°	18.7
Altered pelites	28	17°	19
Sandstone	Substratum		

3.3 In-Situ Tests

Seismic profiles have been made in the right of the core drilling. The results show that the different facies (pelites-sandstone) are not distinguishable in terms of seismic velocity. On the other hand, the depth of alteration, which is relatively homogeneous from the surface, is observed:

- Between 5 and 10 m depth, $V = 300$ to 600 m/s;
- Between 10 and 30 m depth, $V = 1000$ to 1500 m/s;
- Between 30 and 50 m depth, $V = 2000$ to 2500 m/s;
- Above 40 to 50 m depth, $V > 3000$ m/s;

Parameter records also do not distinguish between the two facies, but the altered area is well distinguished about 2 to 5 m from the surface.

4 Verification of the Stability of the Cut by Finite Elements

The geometric site data and soil characteristics were used to create the finite element model shown in Fig. 4.

The behavior of the excavation was modeled with the elasto-plastic law of Mohr-Coulomb. A hydro mechanical transient analysis was done using the Plaxis software and the variations in stresses and deformations were plotted.

In Fig. 5, it is noted that the shear stresses are mainly localized in the clay layer (E/C) and the altered pelite layer (E5 g), which indicates that a rupture mechanism has occurred (Fig. 6).

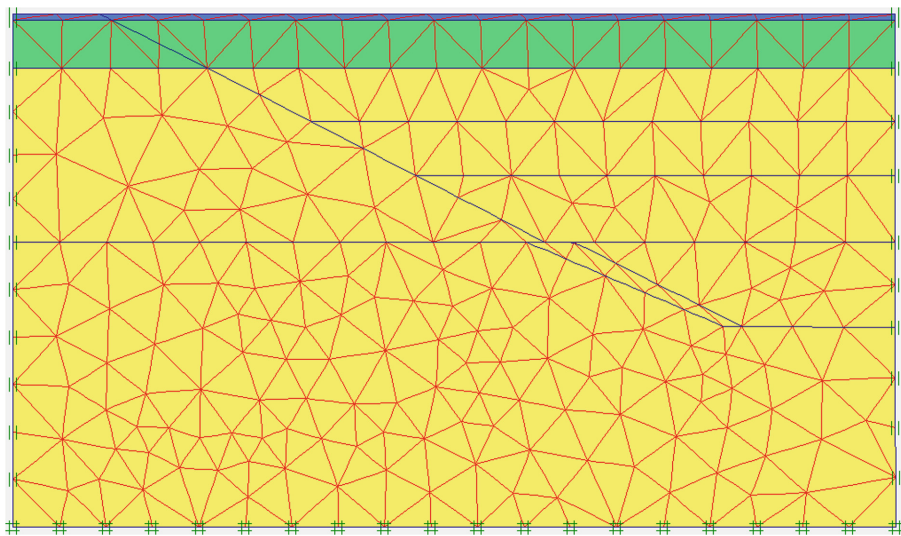


Fig. 4. Finite element model and cutting mesh

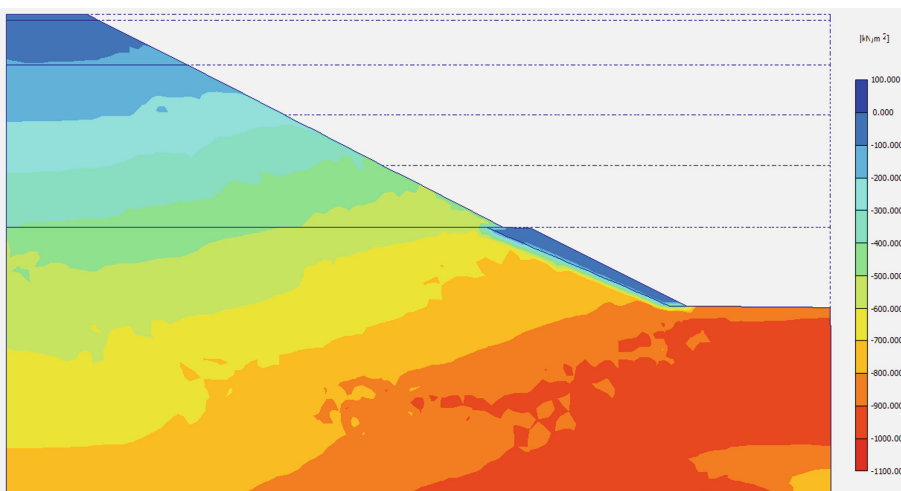


Fig. 5. Shear stresses in the excavation

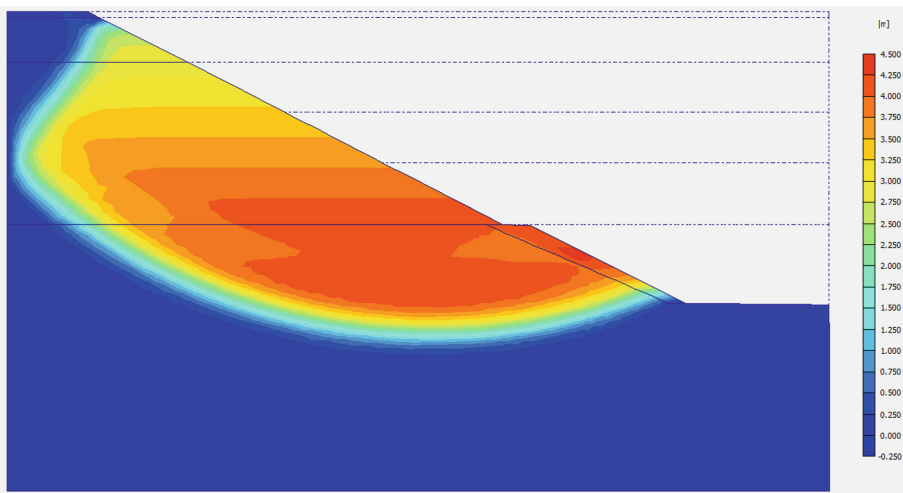


Fig. 6. Horizontal displacements

5 Conclusions

The northern region of Morocco is characterized by various geological formations. The studied slope, characterized by a slope of 28° ; consists of a heterogeneous soil (clay, pelites and sandstone).

The study of this finite element model showed the difficulties and the complexity of the initial conditions in the excavation. The inhomogeneity of the materials constituting the body of the excavation is the main source of diversity of the results found.

The movements of the slope are very important, and shear stresses are very important in the first two layers, which explains why the clay layer and the altered pelites layer is a favorable plan for the sliding process.

References

- Boussaid, K.: Sols intermédiaire pour la modélisation physique: application aux fondations superficielles. In: Intermediate Soils for Physical Modeling: Application to Superficial Foundations: Central School of Nantes and University of Nantes (2005)
- Kouakou, N., Cuisinier, O., Masrouri, F., et al.: Mechanical behavior of heterogeneous granular soils with matrix. Journées Nationales de Géotechnique et de Géologie de l'Ingénieur – Champs-sur-Marne (2018)
- Dine, B.S.E., Dupla, J.C., Frank, R., et al.: Mechanical characterization of matrix coarse-grained soils with a large-sized triaxial device. Canadian Geotechnical Journal. **47**(4), 425–438 (2010)
- Jaboyedoff, M., Oppikofer, T., Derron, M.-H., et al.: Complex landslide behaviour and structural control: A threedimensional conceptual model of Åknes rockslide, Norway. Chapter in Geological Society London Special Publications, London (2011)

- Prime, N., Dufour, F., Darve, F.: Numerical modeling of landslides using a finite element method with lagrangian integration particules. National Days of Geotechnics and Geology of the Engineer JNGG2010 -Grenoble 7–9 juillet 2010 (2010)
- Prunier, F., Darve, F., Laouafa, F.: Modeling of landslides by a material instability criterion. In: 18th French Congress of Mechanics Grenoble, 27–31 août (2007)
- Lyesse, L., John, E., Alessio, F.: Landslide Analysis and Modeling. Technical bulletin of French-speaking Switzerland. August 18, 2010 (2010)
- Droniuc, N.: Finite element analysis of embankments in fine compacted soils. In: Proceedings of the 18th International Conference on Soil Mechanics and Geotechnical Engineering, Paris 2013 (2013)



Effects of Reynolds Number and Aspect Ratio on the Turbulence Characteristics in Developing and Fully Developed Flow Over a Rough Bed

Minakshee Mahananda¹, Prashanth Reddy Hanmaiahgari^{1(✉)},
and Ram Balachandar²

¹ Department of Civil Engineering, Indian Institute of Technology Kharagpur,
Kharagpur 721302, India

minakshee.m@iitkgp.ac.in, hpr@civil.iitkgp.ernet.in

² Department of Civil and Environmental Engineering, University of Windsor,
401 Sunset Ave, Windsor, ON N9B 3P4, Canada

rambala@uwindsor.ca

Abstract. In order to enhance the physical understanding of the turbulent structures, the streamwise evolution of the turbulent flow in narrow open channel over a fixed continuous rough bed has been investigated experimentally. The experiments were conducted to investigate the effects of Reynolds number and aspect ratio on turbulence characteristics in developing and fully developed narrow open channel flows. Instantaneous 3-D velocities were acquired using a Nortek VectrinoPlus down looking acoustic Doppler velocimeter at streamwise intervals of 0.5 m along the centerline of the flume. The time mean velocities with inner scaling for different aspect ratio flows demonstrate the self-similarity of fully developed flow. The effects of Reynolds number and aspect ratio on the normalized turbulence intensities, Reynolds shear stress and turbulent kinetic energy were found significant in the outer region of both the developing and fully developed narrow open channel flow.

Keywords: Developing flow · Fully developed flow · Narrow open channel flow · Turbulence · Dip-phenomenon · Aspect ratio

1 Introduction

Open channel flows are characterised by free surface with a boundary layer type flow near the bed. These flows contain complex three-dimensional turbulent structures that influence the flow behaviour. However, most open channel flows are non-uniform because of ever changing boundary conditions resulting from changes in discharge, cross-section, bed roughness, the presence of hydraulic structures, etc. The flow becomes disturbed whenever there is a change in the boundary condition because of imbalance of viscous, gravitational and inertial forces. Subsequently, the flow tries to attain a fully developed flow condition in the downstream direction. The developing turbulent open channel flow is a complex three-dimensional flow, which is influenced

by aspect ratio (ratio of the width of the channel to the depth of the flow), roughness Reynolds number, and Reynolds number. Therefore, it is essential to understand the flow characteristics in developing and developed open channel flows to assess fluid-sediment interaction and sediment erosion, which are directly linked to the hydrodynamic characteristics such as the vertical distribution of time-averaged velocities, turbulence intensities, Reynolds shear stresses and turbulent kinetic energy.

The spatial evolution of turbulent boundary layer (Marusic et al. 2015; Hanson and Ganapathisubramani 2016, among others) and grid turbulence (Gomes-Fernandes et al. 2014) has been studied extensively. However, the streamwise evolution of flow development in the turbulent open channel flow is limited. To the best of the authors' knowledge, the only study to date of the spatial evolution of turbulent open channel flow is the experimental study of Kirkgoz and Ardiçoglu (1997). They experimentally studied the velocity profiles of developing and fully developed subcritical smooth open channel flow. They found that the boundary layer along the centerline of the channel develops up to the free surface for a flow aspect ratio greater than equal to three and finally it was concluded that the velocity profiles agree well with the logarithmic law in the inner regions of developing and fully developed boundary layer flows. Further, they observed that the wake effect in the developing flow region is weak, which was found to be very important in the velocity profile of the fully developed flow.

The aspect ratio influences the velocity distribution as well as the turbulence characteristics. Wei and Willmarth (1989) stated that the inner-region turbulence structures may be affected by the sidewalls of the channel especially at low Reynolds number. Aspect ratio determines the number of secondary current cells across the channel and the secondary current generates spiral eddies near the free surface which in turn affects the velocities, Reynolds stresses and turbulence intensities (Albayrak and Lemmin 2011). Mahananda et al. (2018) demonstrated that an increase in aspect ratio increases the downward shift in the velocity profile in narrow open channel flows (OCF) for a given Reynolds number. Mahananda et al. (2019) proposed a dip modified wake law for describing the velocity distribution in uniform open channel flow for low aspect ratio flows. Although, the effect of Reynolds number on the turbulence characteristics in turbulent channel flow has been studied by various researchers (Bernardini 2014, Busse et al. 2017), the flow characteristics in developing open channel flow has not been explored fully. Therefore, to fulfil the research gap, the present study aims to investigate the effects of Reynolds number and aspect ratio on the turbulence characteristics in the developing flow and fully developed flow.

2 Experimental Methodology

The experiments were conducted in a rectangular flume of dimensions 7.0 m long × 0.6 m wide × 0.7 m deep in the HWRE Laboratory at Indian Institute of Technology Kharagpur, India. Figure 1 shows the schematic diagram of the experimental flume. To allow visual observations, the side walls are made of glass. A honeycomb was fixed at the inlet to the flume to stabilize the flow and turbulence. Rails were provided on the side walls to hold a carriage which can be moved along the streamwise direction. A track was provided in lateral direction on the carriage to allow the movement of

instruments in the transverse direction. The flume bottom has a cement mortar finished with a roughness of sand diameter $d_{50} = 2.25$ mm. Water is recirculated from the flume to an underground sump and back to the flume by using a vertical centrifugal pump. The flow rate was controlled by a valve located at the upstream of the flume inlet chamber. A tailgate was used to control the required flow depth in the flume. The flow depth in the channel was measured with the help of Vernier point gauge with an accuracy of ± 0.1 mm.

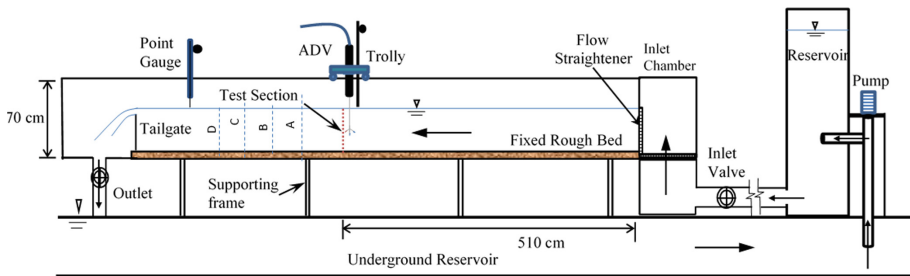


Fig. 1. Schematic of the experimental setup and measurement locations

A three-dimensional coordinate system is used to locate the measurement stations. In the coordinate system, the streamwise direction, vertical direction and lateral direction are represented by x -axis, z -axis and y -axis, respectively. The total length of the working section is 3 m which begins at $x = 2.65$ m and ends at $x = 5.15$ m in the streamwise direction. The velocity measuring stations denoted by A, B, C and D were located at streamwise locations $x = 2.65, 3.65, 4.65$ and 5.15 m, respectively, along the centerline for different vertical levels depending upon the flow depth of the experimental runs. The vertical locations considered were $z = 0.3, 0.5, 0.7, 0.9, 1.5, 2, 2.5, 3, 4, 5, 6, 7, 8, 9, 10, 11, 12, 13, 14$ and 15 cm from the channel bed. Four tests were carried out for two Reynolds numbers $Re = 2.8 \times 10^4$ and 4.5×10^4 and two aspect ratios, $Ar = 3.0$ and 4.1 , where Ar is defined as the aspect ratio of flow. As the aspect ratio is less than five, the flow can be considered to be narrow open channel flows (Nezu and Nakagawa 1993). The detailed experimental conditions were provided in Table 1.

Table 1. Details of hydraulic parameters of the present experimental conditions

Run	h (m)	δ (m)	\bar{u} (m/s)	U_{max} (m/s)	Ar	$Re(\times 10^4)$	F_r
ER1	0.2	0.14	0.37	0.40	3.0	4.5	0.27
ER2	0.2	0.15	0.23	0.23	3.0	2.8	0.15
ER3	0.15	0.13	0.46	0.58	4.1	4.5	0.41
ER4	0.15	0.11	0.27	0.30	4.1	2.8	0.23

The instantaneous flow velocities were measured by a Nortek VectrinoPlus acoustic Doppler Velocimeter (ADV) having four down looking acoustic Doppler probes and an emitter at the center. The Vectrinoplus ADV measures velocities 50 mm below its emitter to avoid the disturbance caused by the probe. The sampling frequency and sampling duration were set to be 100 Hz and 300 s, respectively. Low frequency spikes in the ADV data were removed by using the phase space threshold method developed by Goring and Nikora (2002). Further, the data was filtered for low SNR and correlation values as recommended by Chanson et al. (2008).

In the present study, u , v and w are defined as the streamwise, transverse and vertical instantaneous velocities components respectively. Similarly, u' , v' and w' are defined as the streamwise, transverse and vertical velocity fluctuations respectively. Normalized values of velocities in inner layer scaling were denoted by u/u_* , v/u_* and w/u_* , where u_* is defined as the shear velocity. The normal stresses $\sqrt{u'u'}$, $\sqrt{v'v'}$ and $\sqrt{w'w'}$ are the streamwise turbulence intensity denoted by u_{rms} , turbulence intensity in transverse direction denoted by v_{rms} and vertical turbulence intensity denoted by w_{rms} , respectively. Similarly, normalized Reynolds shear stresses are represented as $-\overline{u'w'}^+ = (-\overline{u'w'})/u_*^2$. The experimental uncertainty errors of time mean velocities (u , v , and w), root mean square velocities (u' , v' and w') and $-\overline{u'w'}$ are found to be less than 2%–5%, 5%–7%, and 10–12.5%, respectively in the inner layer.

3 Results and Discussion

3.1 Streamwise Velocity

Figure 2 illustrates the effects of Reynolds number and aspect ratio on vertical distributions of the normalized time averaged streamwise velocities along the centerline of developing and developed flow. The friction velocity is adopted for scaling the turbulent flow characteristics and the vertical coordinate is scaled with flow depth. For this inner layer scaling, friction velocity in the fully developed flow of that corresponding experiment was chosen. The experiments ER1 to ER4 are hydraulically rough narrow open channel flows, and they are only considered to study aspect ratio effect on turbulence characteristics. Experiments ER1 and ER3 are of the same Reynolds number, but different aspect ratios. Experiments ER3 and ER4 are of the same aspect ratio, but different Reynolds numbers (Table 1). Measurements at $x = 2.65$ m, 3.65 m, 4.65 m, and 5.15 m are considered, in which velocities at $x = 2.65$ m, 3.65 m, 4.65 m are in the developing flow regime whereas the velocity profile at $x = 5.15$ m is in the fully developed region. Plots in the top row of the Fig. 2, are meant for determining the Reynolds number effect, whereas the plots in the bottom row are meant for determining the aspect ratio effect. From the non-overlapping nature of the velocity distribution, the influence of Reynolds number is noticed in the inner layer in the beginning of the developing flow. However, as the flow begins to develop, the Re effect in the inner layer is diminished, but its effect is increased in the outer region. In the fully developed flow region, Re effect is significant in the outer layer based on the roughness geometry (Bhaganagar et al. 2004). Due to increase in Reynolds number, the percentage increase

in shear velocity is less than the percentage increase in time mean velocity in the outer layer; therefore, u/u_* in the outer layer for higher Reynolds number flow is higher than the lower Reynolds number flow. Therefore, it is concluded that the Reynolds number effect is predominant in the outer layer in the narrow open channel flow and a higher Reynolds number flow has higher normalized streamwise velocity in the outer region.

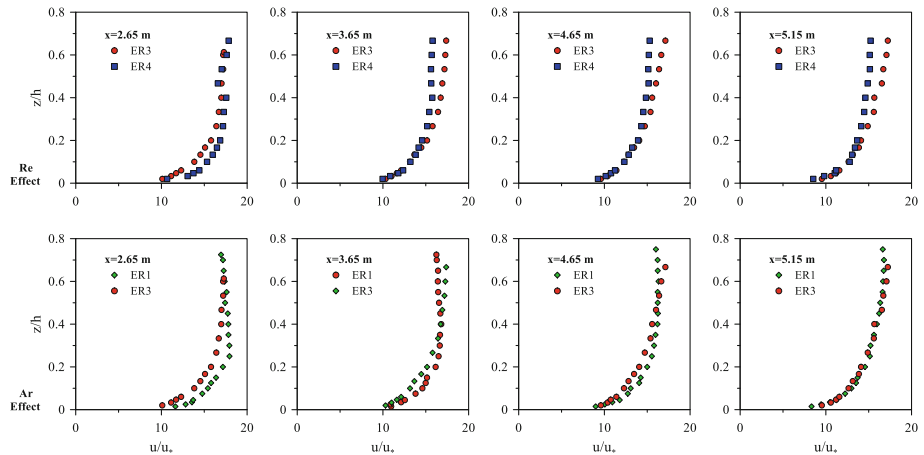


Fig. 2. Effect of R_e and A_r on vertical distribution of normalized streamwise velocity

In the second row of graphs, the aspect ratio effect on time mean streamwise velocity is visible in the developing flow region, but the effect diminishes in the fully developed region (Fig. 2). In the fully developed flow, a collapse of data is found, which demonstrates the effect of secondary currents created by lower aspect ratio on time mean velocities in the wall shear layer and intermediate layer is absorbed due to proper scaling variables. Finally, it is concluded that time mean velocities with inner scaling for different Ar flows demonstrate the self-similarity of fully developed flow.

3.2 Turbulence Intensities

The vertical profiles of streamwise turbulence intensity $u_{rms}^+ = u_{rms}/u_*$, lateral turbulence intensity $v_{rms}^+ = v_{rms}/u_*$ and vertical turbulence intensity $w_{rms}^+ = w_{rms}/u_*$ are presented in Figs. 3, 4 and 5, respectively.

Increase in either Reynolds number or aspect ratio increases the strength of small-scale motions, i.e., turbulence intensities (Bernardini 2014; Busse et al. 2017 and Mahananda et al. 2018). Reynolds number effect on u_{rms}^+ is seen throughout the depth in the entrance region of developing flow, i.e., u_{rms}^+ of flow with low R_e is higher than the high R_e flow in the entrance region (see Fig. 3). The effect of R_e decreases in the inner region as the flow develops. In the fully developed flow, i.e., at $x = 5.15$ m, R_e effect is completely diminished in the inner layer, whereas its effect is still distinctive in the outer layer ($z/h > 0.2$). Streamwise turbulence intensity of lower Reynolds number

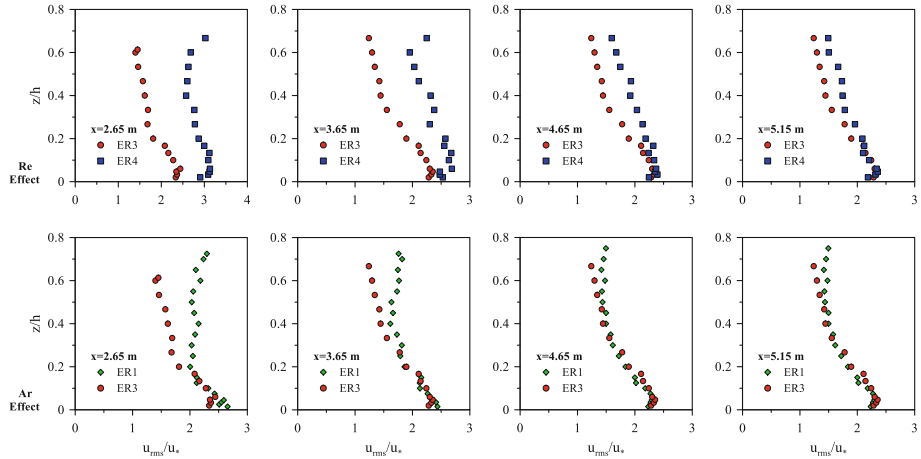


Fig. 3. Effect of R_e and A_r on vertical distribution of normalized streamwise turbulence intensity

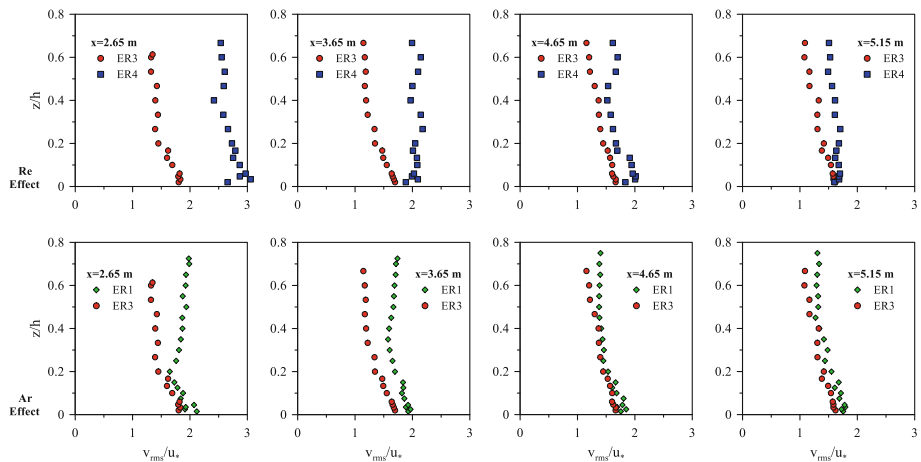


Fig. 4. Effect of R_e and A_r on vertical distribution of normalized lateral turbulence intensity

flow in the outer region is more than that of higher Reynolds number flow, the trend being similar to the experiments over rough surfaces carried by Krogstad et al. (1992).

The bottom row in Fig. 3 shows the effect of aspect ratio on the streamwise turbulence intensity. The effect of aspect ratio on u_{rms}^+ is significant in the outer region in the initial region of flow development length. In fact, the lower aspect ratio flow has higher u_{rms}^+ in the outer region (Vinuesa et al. 2014 and Mahananda et al. 2018). However, the difference in the u_{rms}^+ between the two aspect ratios decreases as the flow development attains a fully developed state. It may be inferred that along the centerline of the developing flow, the effect of Ar on the u_{rms}^+ profiles is dominant after 0.4 h above the bed towards the free surface where the magnitude of turbulence intensity is

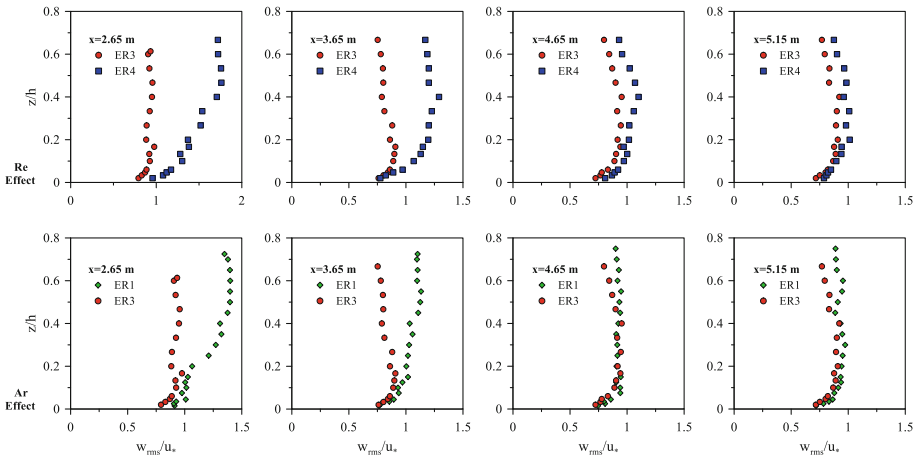


Fig. 5. Effect of Re and Ar on vertical distribution of normalized vertical turbulence intensity

greater for $Ar = 3.0$ as compared to $Ar = 4.1$. That means, the lower aspect ratio flow has higher u_{rms}^+ in the outer region of the fully developed flow, which demonstrates the interaction between secondary currents and turbulence (Nezu et al. 1985, Vinuesa et al. 2015). In the fully developed flow, streamwise turbulence intensity for $z/h > 0.4$ increases towards the free surface due to the dip effect. In addition, Fig. 3 demonstrates that the streamwise turbulence intensity decreases along the flow development length irrespective of either aspect ratio or Reynolds number.

Figures 4 and 5 show the effect of Reynolds number and aspect ratio on vertical profiles of lateral (v_{rms}^+) and vertical (w_{rms}^+) turbulence intensities, respectively. The effect of Reynolds number on v_{rms}^+ and w_{rms}^+ throughout the depth is clearly seen in the developing flow region and the effect diminishes along the flow development length (Figs. 4 and 5). In fully developed flow region, the effect of Re on v_{rms}^+ and w_{rms}^+ is distinct in the outer layer ($z/h > 0.2$). The lower Re flow has higher v_{rms}^+ and w_{rms}^+ than those of higher Re flow. The v_{rms}^+ and w_{rms}^+ range between $v_{rms}^+ = 1.0 - 3.0$ and $w_{rms}^+ = 0.5 - 2.0$, respectively in the narrow open channel flow.

The aspect ratio (Ar) effect on v_{rms}^+ and w_{rms}^+ is found throughout the depth in the developing flow region (refer to Figs. 4 and 5), which is similar to that of Re effect. Figures 4 and 5 illustrate that lower aspect ratio flow has higher v_{rms}^+ and w_{rms}^+ than the higher aspect ratio flow caused by the turbulence driven secondary currents. In the fully developed flow, aspect ratio effect is strong in the outer region i.e., $z/h > 0.4$ because of large scale motion. The w_{rms}^+ attains a constant value of nearly equal to the shear velocity in the outer layer in the case of fully developed flow. The suppression of vertical turbulence intensities in the free surface region explains the characteristic pattern of secondary currents in the open channel flow (Tominaga et al. 1989).

The observed ascending order of turbulence intensities in developing narrow open channel rough flow is $w_{rms} < v_{rms} < u_{rms}$ which indicates that universality and similarity exists in the structure of turbulence regardless of Reynolds number, and aspect ratio (Nezu and Nakagawa 1993). The normalized streamwise, lateral and vertical turbulence

intensities of low Reynolds number flow are found to be more than that of high Reynolds number flow for a given aspect ratio and vice versa lower aspect ratio flow has higher normalized turbulence intensities for a given Reynolds number.

3.3 Reynolds Shear Stresses

The Reynolds shear stresses (RSS) are second order moments, which provide correlations between different fluctuating velocity components. Reynolds shear stresses offer resistance to the flow in the corresponding plane and govern secondary flows as well as flow development. Figure 6 depicts the vertical distribution of normalized Reynolds shear stress $\tau_{uw}^+ = -\overline{u'w'}/u_*^2$ along the developing and fully developed flow at different stations.

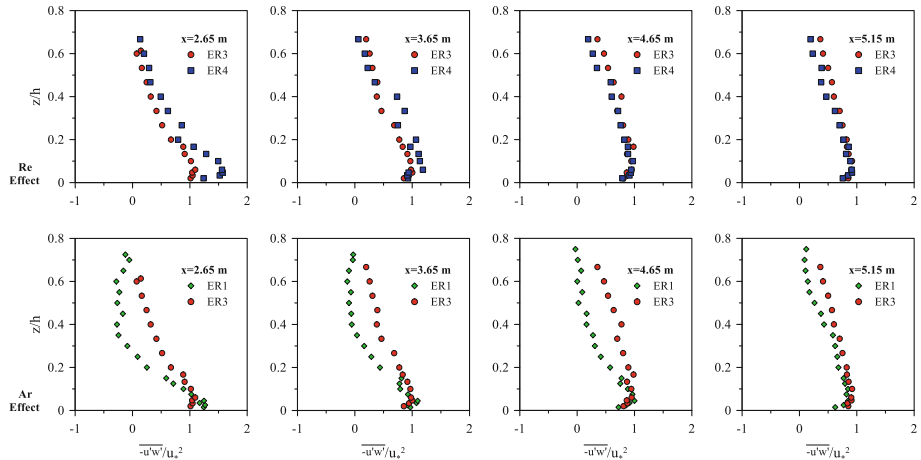


Fig. 6. Effect of Re and Ar on vertical distribution of normalized Reynold shear stress τ_{uw}

Figure 6 demonstrates the diminishing effect of Re on the RSS along the flow development. Reynolds number has no effect on the RSS in the inner region of fully developed flow; while Re has little effect in the outer layer of fully developed flow. Contrary to the turbulence intensities, higher RSS in the outer layer is found in the higher Re flow as compared to the lower Re flow. The aspect ratio effect is seen throughout the depth in the developing flow and its effect seen only in the outer layer of the fully developed flow (Fig. 6). The lower aspect ratio flow has a lower RSS in the outer layer as compared to that of higher aspect ratio flow. For the experimental run ER1, sign change of τ_{uw}^+ from positive to negative occurs at $z/h \geq 0.6$, which signifies the existence of dip phenomena in the fully developed narrow open channel flow (Yang et al. 2004).

3.4 Turbulent Kinetic Energy

Discussion on the distribution of turbulent kinetic energy (TKE) along the depth is important since it is related to presence of turbulence intermittency. In addition, TKE distribution identifies the region where the maximum production occurs and the region contains larger eddies. Hence, the plots of vertical distributions of turbulent kinetic energy k normalized by u_*^2 in developing and fully developed flow are plotted in Fig. 7. The normalized turbulent kinetic energy (k^+) profiles in the developing flow region are different for different Reynolds numbers (Fig. 7). In the developing flow region, the low Re and low Ar flows have higher k^+ and their effects decrease as the flow develops. In the fully developed flow, Re and Ar effects on k^+ are negligible in the inner layer, however, their effect is distinct in the outer layer.

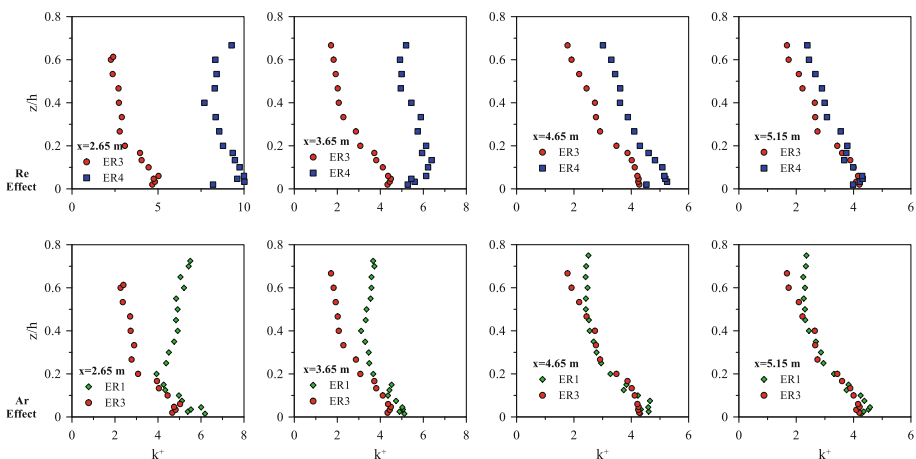


Fig. 7. Effect of R_e and A_r on vertical distribution of normalized turbulent kinetic energy

4 Conclusions

The present study investigated the effects of Reynolds number and aspect ratio on turbulence characteristics in developing and fully developed narrow open channel flow over a fixed continuous rough bed. The time mean velocities with inner scaling for different aspect ratio flows demonstrate the self-similarity of fully developed flow. The effects of Reynolds number and aspect ratio on the normalized three-dimensional turbulence intensities, Reynolds shear stress and turbulent kinetic energy were found significant in the outer region of both the developing and fully developed narrow open channel flow. Suppression of vertical turbulence intensity was observed in the outer region in the fully developed flow, which explains the characteristic pattern of secondary currents in the narrow open channel flow. In the developing flow, normalized turbulence intensities and TKE in the outer region of low Reynolds number flows are more than those of high Reynolds number for a given aspect ratio. Vice-versa, normalized turbulence intensities and TKE in the outer region of low aspect ratio flows are

higher than those of high aspect ratio flows for a given Reynolds number. Contrarily, normalized Reynolds shear stress in the outer region of high Reynolds number and high aspect ratio flows are higher than those of either low Reynolds number or lower aspect ratio flows.

References

- Albayrak, I., Lemmin, U.: Secondary currents and corresponding surface velocity patterns in a turbulent open-channel flow over a rough bed. *J. Hydraul. Eng.* **137**(11), 1318–1334 (2011)
- Bakken, O.M., Krogstad, P.A., Ashrafiyan, A., Andersson, H.: Reynolds number effects in the outer layer of the turbulent flow in a channel with rough walls. *Phys. Fluids* **17**, 065101 (2005)
- Bernardini, M.: Reynolds number scaling of inertial particle statistics in turbulent channel flows. *J. Fluid Mech.* **758**, R1 (1–14) (2014)
- Bhaganagar, K., Kim, J., Coleman, G.: Effect of roughness on wall-bounded turbulence. *Flow Turbul. Combust.* **72**, 463–492 (2004)
- Busse, A., Thakkar, M., Sandham, N.D.: Reynolds number dependence of the near wall flow over irregular rough surfaces. *J. Fluid Mech.* **810**, 196–224 (2017)
- Chanson, H., Trevethan, M., Aoki, S.I.: Acoustic Doppler velocimetry (ADV) in small estuary: field experience and signal post-processing. *Flow Meas. Instrum.* **19**(5), 307–313 (2008)
- Gomes-Fernandes, R., Ganapathisubramani, B., Vassilicos, J.C.: Evolution of the velocity-gradient tensor in a spatially developing turbulent flow. *J. Fluid Mech.* **756**, 252–292 (2014)
- Goring, D.G., Nikora, V.I.: Despiking Acoustic Doppler velocimeter data. *J. Hydraul. Eng.* **128**(1), 117–126 (2002)
- Hanson, R.E., Ganapathisubramani, B.: Development of turbulent boundary layers past a step change in wall roughness. *J. Fluid Mech.* **795**, 494–523 (2016)
- Kirkgoz, M.S., Ardiçoglu, M.: Velocity profiles of developing and developed open channel flow. *J. Hydraul. Eng.* **123**(12), 1099–1105 (1997)
- Krogstad, P.A., Antonia, R.A., Browne, L.W.B.: Comparison between rough- and smooth-wall turbulent boundary layers. *J. Fluid Mech.* **245**, 599–617 (1992)
- Mahananda, M., Hanmaiahgari, P.R., Balachandar, R.: Effect of aspect ratio on developing and developed narrow open channel flow with rough bed. *Can. J. Civ. Eng.* **45**(9), 780–794 (2018)
- Mahananda, M., Hanmaiahgari, P.R., Ojha, C.S.P., Balachandar, R.: A new analytical model for velocity distribution in fully developed turbulent OCF. *Can. J. Civ. Eng.* (2019). <https://doi.org/10.1139/cjce-2018-0615>
- Marusic, I., Chauhan, K.A., Kulandaivelu, V., Hutchins, N.: Evolution of zero pressure gradient boundary layers from different tripping conditions. *J. Fluid Mech.* **783**, 379–411 (2015)
- Nezu, I., Nakagawa, H., Tominaga, A.: Secondary currents in a straight channel flow and the relation to its aspect ratio. In: *Turbulent Shear Flows 4*, pp. 246–260. Springer (1985)
- Nezu, I., Nakagawa, H.: *Turbulence in Open-Channel Flows*. IAHR/AIRH Monograph Series. Balkema, Rotterdam (1993)
- Tominaga, A., Nezu, I., Ezaki, K., Nakagawa, H.: Three-dimensional turbulent structure in straight open channel flows. *J. Hydraul. Res.* **27**(1), 149–173 (1989)
- Vinuesa, R., Noorani, A., Lozano-Durán, A., El Khoury, G.K., Schlatter, P., Fisher, P.F., Nagib, H.M.: Aspect ratio effects in turbulent duct flows studied through direct numerical simulation. *J. Turbulence* **15**(10), 677–706 (2014)

- Vinuesa, R., Schlatter, P., Nagib, H.M.: On minimum aspect ratio for the duct flow facilities and the role of side walls in generating secondary flows. *J. Turbulence* **16**(6), 588–606 (2015)
- Wei, T., Willmarth, W.W.: Reynolds number effects on the structure of a turbulent channel flow. *J. Fluid Mech.* **204**, 57–95 (1989)
- Yang, S.Q., Tan, S.K., Lim, S.Y.: Velocity distribution and dip-phenomenon in smooth uniform open channel flows. *J. Hydraul. Eng.* **130**(12), 1179–1186 (2004)

Author Index

A

- Abdelfattah, Mohamed, 108
Abdel-Rahman, Khalid, 108
Abdulla, Fayed, 1
Abouzied, Mohamed, 63
Abu-Zreig, Majed, 1
Ahmed, Sayed M., 108
Al-Omari, Abbas, 1
Ardouz, Ghizlane, 125

B

- Baba, Khadija, 125
Balachandar, Ram, 133

D

- Dawleh, Bashar Abu, 1
Dey, Arindam, 34
Di Girolamo, Luca, 89

E

- El-Mossallamy, Yasser M., 108

H

- Haider, Abbas, 19
Hanmaiahgari, Prashanth Reddy, 133

K

- Khater, Khaled R., 63

M

- Mahananda, Minakshee, 133
Marone, Gabriella, 89
Mizanur Rahman, Md., 56
Mukherjee, Mousumi, 34

N

- Nguyen, Hoang Bao Khoi, 48, 56

P

- Pirone, Marianna, 89

R

- Rahman, Mizanur, 48
Russo, Gianpiero, 89

S

- Song, Erxiang, 19
Sun, Yujin, 19

W

- Wang, Hung-Chun, 48, 56

Z

- Zhang, Ruiyu, 19